ENZYME-CATALYZED DEGRADATION OF CARBON NANOMATERIALS

by

Gregg P. Kotchey

B.S. Chemistry, University of Pittsburgh, 2004

Submitted to the Graduate Faculty of

The Dietrich School of Arts and Sciences in partial fulfillment

of the requirements for the degree of

Doctor of Philosophy

University of Pittsburgh

2013

UNIVERSITY OF PITTSBURGH

THE DIETRICH SCHOOL OF ARTS AND SCIENCES

This dissertation was presented

by

Gregg P. Kotchey

It was defended on

August 20, 2013

and approved by

Dr. Adrian C. Michael, Professor, Department of Chemistry

Dr. Renã A. S. Robinson, Assistant Professor, Department of Chemistry

Dr. Valerian E. Kagan, Professor, Department of Environmental and Occupational Health

Dissertation Advisor: Dr. Alexander Star, Associate Professor, Department of Chemistry

ENZYME-CATALYZED DEGRADATION OF CARBON NANOMATERIALS

Gregg P. Kotchey, PhD

University of Pittsburgh, 2013

Carbon nanotubes and graphene, the nanoscale sp^2 allotropes of carbon, have garnered widespread attention as a result of their remarkable electrical, mechanical, and optical properties and the promise of new technologies that harness these properties. Consequently, these carbon nanomaterials (CNMs) have been employed for diverse applications such as electronics, sensors, composite materials, energy conversion devices, and nanomedicine. The manufacture and eventual disposal of these products may result in the release of CNMs into the environment and subsequent exposure to humans, animals, and vegetation. Given the possible pro-inflammatory and toxic effects of CNMs, much attention has been focused on the distribution, toxicity, and persistence of CNMs both in living systems and the environment.

This dissertation will guide the reader though recent studies aimed at elucidating fundamental insight into the persistence of CNMs such as carbon nanotubes (CNTs) and graphene derivatives (*i.e.*, graphene oxide and reduced graphene oxide). In particular, in-test-tube oxidation/degradation of CNMs catalyzed by peroxidase enzymes will be examined, and the current understanding of the mechanisms underlying these processes will be discussed. Finally, an outlook of the current field including *in vitro* and *in vivo* biodegradation experiments, which have benefits in terms of human health and environmental safety, and future directions that could have implications for nanomedical applications such as imaging and drug delivery will be presented.

Armed with an understanding of how and why CNMs undergo enzyme-catalyzed oxidation/biodegradation, researchers can tailor the structure of CNMs to either promote or inhibit these processes. For example, in nanomedical applications such as drug delivery, the incorporation of carboxylate functional groups could facilitate biodegradation of the nanomaterial after delivery of the cargo. Also, the incorporation of CNMs with defect sites in consumer goods could provide a mechanism that promotes the degradation of these materials once these products reach landfills.

TABLE OF CONTENTS

LIST OF TABLES

LIST OF FIGURES

LIST OF EQUATIONS

PREFACE

I would first like to express my sincerest gratitude to my research advisor, Professor Alexander Star, without whom I would not be defending a Ph.D. Not only have I developed as a scientist and writer under his guidance, but also I have learned other important qualities through his example over these years that have made me a better person. It has been a true honor to work and learn from him.

I also would like to express my appreciation to the members of my committee, Professor Valerian Kagan, Professor Adrian Michael, and Professor Renã Robinson. These individuals are respected members of the scientific community, and I greatly appreciate both their patience and valuable advice throughout the years.

Furthermore, I wanted to extend a special thanks to all of my collaborators. Not only have they contributed to making my graduate career productive, but also I have learned a great deal of science through our efforts. To this end, I am especially grateful to past and present Star group members, Dr. Brett Allen, Dr. Yanan Chen, Dr. Mengning Ding, Dr. Yifan Tang, Dr. Harindra Vedala, Gordon Chiu, and Yong Zhao, for our fruitful collaborative efforts. I also extend my appreciation to Dr. Andon, Dr. Sorescu, Dr. Tkach, Dr. Yanamala, Professor Fadeel, Professor Kagan, Professor Kapralov, Professor Klein-Seetharaman, Professor Shvedova, and Professor Tyurina with whom I have collaborated outside of the chemistry department. In

particular, I would like to thank Professor Kagan for his feedback over the years during our collaborations; I feel that I have matured as a scientist as a result of this relationship.

Moreover, I am very grateful to past and present members of the Star Group with whom I have had the pleasure to interact with and befriend during my graduate career. I enjoyed countless lunches with Dr. Yanan Chen, Dr. Mengning Ding, Dr. Yifan Tang, and Yong Zhao. To James A. Gaugler for your reliable assistance during both your undergraduate and the beginning of your graduate career, I wish you continued success. To all other past members of the group, Dr. Brett Allen, Hao Bai, Brian Barth, Sruti Bhaumik, Ian Feigel, Dr. Pingping Gou, Dr. Douglas Kauffman, Dr. Nadine Kraut, and Dr. Harindra Vedala, and current members, Seth Burkert, Gordon Chiu, Dr. Haifeng Dong, James Ellis, Dr. Uri Green, Zachary Michael, Gregory Morgan, Wanji Seo, and Yong Zhao, it has been a pleasure working together and I wish you the best of luck with your future endeavors.

Next, I would like to extend my gratitude to the faculty and staff of the Department of Chemistry for the knowledge, friendship, and assistance that you have provided thought the years. In particular, I would like to thank Professor Weber for his understanding and guidance. Also, I appreciate all of the work that Darlene Lanz, Evon Nigro, Mary Schwarman, and the chemistry stockroom have done on my behalf. Much appreciation is owed to Tom Harper from the Department of Biological Science for his assistance with electron microscopy, Michael L. McDonald and Dr. Susheng Tan from the NFCF, and Dr. Joel Gillespie, head of the Department of Chemistry's Materials Characterization Lab.

I would not be where I am today without the constant love and support of my family and friends. To my parents, David and Michelle, thank you for you unconditional love, support, and encouragement. To my best friend and sister, Nicole, thank-you for always being there for me to

lean on and being my role model as a scientist. To my dogs, Wellington and Harry, thank you for your constant loyalty and companionship during my graduate studies. To George and Regina ("Flo"), thank you for providing the much needed comic relief and friendship during both my undergraduate and graduate careers. To my dear friends from graduate school and college such as, Professor Justin Chalker, Dr. Erin Skoda, Dr. Carol Fortney, Dr. Ericka Huston, Joshua Jones, Professor Joshua Pierce, Dr. Christopher Rosenker, Kara Rosenker, thank you for your help, support, and our valued friendship. To my good friend Mary, I could not have made it through this process without your continual guidance.

Finally, I would like to extend my gratitude to University of Pittsburgh, National Institute of Environmental Health and Safety (NIEHS), and the United States Environmental Protection Agency (EPA) for their financial support.

1.0 INTRODUCTION

1.1 CHAPTER PREFACE

The goal of this dissertation is to guide the readers through recent efforts to degrade carbon nanomaterials *via* enzymatically driven reactions. To this end, this first chapter will provide an introduction to carbon nanotubes (CNTs) and graphene, the nanoscale, sp^2 allotropes of carbon employed in the degradation studies. Moreover, background regarding the three peroxidase enzymes (*i.e.*, horseradish peroxidase (HRP), myeloperoxidase (MPO), and eosinophil peroxidase (EPO)) that were utilized for the degradation of carbon nanomaterials is discussed. The material contained within Section 1.2 and Sections 1.4.1 to 1.4.3 was primarily reproduced from original works with permission from [1] and [2]. Copyright 2010 Momentum Press, LLC. and Copyright 2012 John Wiley and Sons, Ltd., respectively. The content of Section 1.6 was primarily reproduced from original works with permission from [3] and [4]. Copyright 2012 American Chemical Society and Copyright 2013 Elsevier B.V., respectively.

1.2 CARBON NANOTUBES

In the 1970s and 1980s, carbon filaments with diameters that measured less than 10 nm were formed through the decomposition of hydrocarbons at high temperatures in the presence of transition-metal nanoparticles of the same diameter.[5] Due to limitations in imaging technology, no methodical studies were conducted on these filaments. The real excitement over nanotubes began in 1991 with the discovery and characterization of multiwall carbon nanotubes (MWCNTs) by Iijima of the NEC Laboratories in Tsukuba, Japan.[6] Around the same time of Iijima's discovery (1992), a group working independently in Russia also discovered multiwall carbon nanotubes and nanotube bundles.[7, 8] Less than two years later, Iijima and his group at NEC[9] and Bethune at the IBM Almaden laboratory[10] discovered single-walled carbon nanotubes (SWCNTs). In 1992, it was theoretically predicted[11-13] that nanotubes could be either semiconducting or metallic, depending on their geometry; it required an additional six years to confirm this hypothesis experimentally.

1.2.1 Structure of Carbon Nanotubes

A single-walled carbon nanotube is an elongated fullerene, which also consists of 12 pentagons and thousands of hexagons making a tubular structure. SWCNTs can be visualized as an individual graphene sheet rolled into a cylinder along a lattice vector (m, n) (refer to Figure 1b). Similarly, as depicted in Figure 1a, a multiwalled carbon nanotube is composed of multiple concentric SWCNTs. The diameter of the nanotube is typically based on the size of the metal nanoparticles from which the nanotube is grown; generally speaking, the diameters of SWCNTs

and MWCNTs range from 0.4 to 3 nm and from 2 to 100 nm, respectively.[14] Moreover, the lengths of nanotubes range from tens of nanometers to several micrometers.

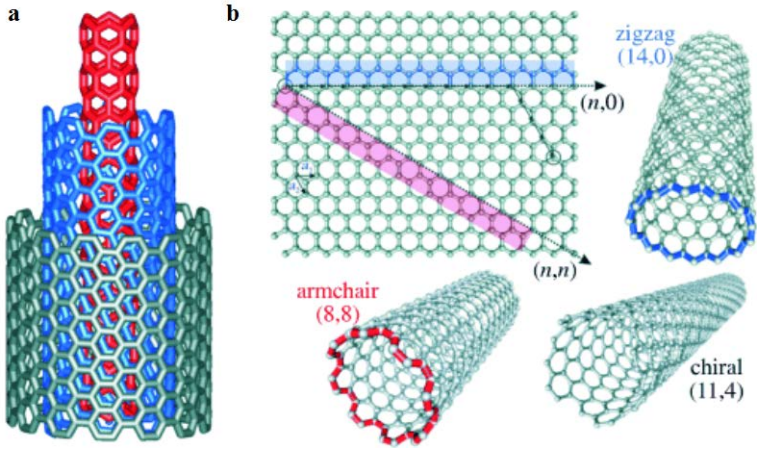

Figure 1. (a) Conceptualized depiction of a multiwalled carbon nanotube (MWCNT) with concentrically nestled walls. A single-walled carbon nanotube (SWCNT) consists of one wall, or the innermost carbon nanotube (CNT). (b) Schematic depiction of the roll-up vectors (*n*, *m*) of a CNT, showing armchair (*n* = *m*), chiral (*n* ≠ *m*), and zigzag (*n*, 0) SWCNTs. (Reprinted with permission from [15]. Copyright 2008 WILEY-VCH Verlag GmbH & Co. KGaA, Weinheim).

The carbon atoms in a nanotube are sp^2-hybridized, and three out of four of the outer-shell electrons are involved in bonding with neighboring carbons. The fourth electron is located in a *p* orbital that runs perpendicular to the graphene lattice. For an infinitely flat graphene sheet, the arrangement of *p* orbitals would provide a semimetallic structure, with the *p*-orbital electrons organized in broad valence (π) and conductance (π*) bands, and the semimetallic structure would have a zero band gap. When the graphene sheet is rolled to form a nanotube, however, partial σ–π hybridization occurs due to the π and π* electron orbitals experiencing significant curvature. This property leads to 1-D quantum confinement, in which the density of states depends on the diameter, chirality, and type of nanotube.[14]

The circumference of a nanotube is expressed by the Hamada vector, $\mathbf{C_h}$, such that

Equation 1: $\mathbf{C_h} = n\mathbf{a_1} + m\mathbf{a_2}$.

The values for *n* and *m* are integers that are characteristic of each nanotube, and $\mathbf{a_1}$ and $\mathbf{a_2}$ represent two lattice unit vectors. Due to the degree of orbital overlap, the (*n*, *m*) values predict whether a nanotube will be metallic (*i.e.*, zero band gap, when $n = m$), semimetallic (*i.e.*,, a small band gap, ca. 10 meV, when $n - m = 3k$ with *k* being an integer), or semiconducting (*i.e.*,, a large band gap, ca. $\geq$0.6 eV, when $n - m \neq 3k$) (refer to Figure 1b). Generally, a semimetallic nanotube is classified as metallic due to its small band gap. Moreover, the (*n*, *m*) values determine the shape of the nanotube. For the case ($n = m$), the nanotube is referred to as an armchair structure. When (*n*, 0) occurs, the nanotube will have a zigzag appearance. Finally, when ($n \neq m$), the structure of the nanotube is characterized as being chiral.

1.2.2 Synthesis of Carbon Nanotubes

1.2.2.1 Synthesis of Multiwalled Carbon Nanotubes

One method of producing MWCNTs employs electric arc discharge; the major breakthrough for this method occurred in 1992, when Ebbesen and Ajayan produced MWCNTs on the gram scale.[5] In this technique, a high current is passed through a carbon anode and cathode; this current ignites He gas, causing plasma to form. Carbon atoms vaporize in the plasma, which permits the formation of nanotubes. MWCNTs are obtained by controlling the current and the pressure of the inert gas. The MWCNTs usually have diameters that range from 5 to 30 nm, and the length of the nanotubes is tens of micrometers. Moreover, the nanotubes produced by this method are extremely straight due to their high crystallinity, and the sidewalls usually contain

few defects. The MWCNTs are purified through heating in an oxygen environment, where other carbaceous material produced during the synthesis would be oxidized.

A second method to produce MWCNTs involves chemical vapor deposition (CVD), which is depicted in Figure 2.[5] This method entails flowing a hydrocarbon gas over a substrate that contains metal catalysts; the entire system is heated in a tube oven. The nanotubes are grown over the catalysts and collected once the system is cooled down to room temperature. The hydrocarbon precursor, the transition-metal catalyst, and temperature are the controllable parameters for the CVD process. During the CVD process, the hydrocarbon is dissociated by means of the metal catalyst. The carbon atoms subsequently dissolve and saturate in the melted metal nanoparticles, and as the saturated carbon precipitates out, it forms tubular sp^2 structures. The tubular form is favored because it lowers the surface energy by eliminating dangling bonds. To grow MWCNTs, ethylene or acetylene is employed as the precursor, and the oven temperature is usually between 550 and 750°C. The metal catalyst for MWCNT production is usually iron, cobalt, or nickel because of carbon's finite solubility in these metals at high temperatures. MWCNTs grown by CVD contain a high number of defects, which are likely due to the low growth temperature not providing sufficient thermal energy to anneal the nanotubes into perfect crystalline structures.

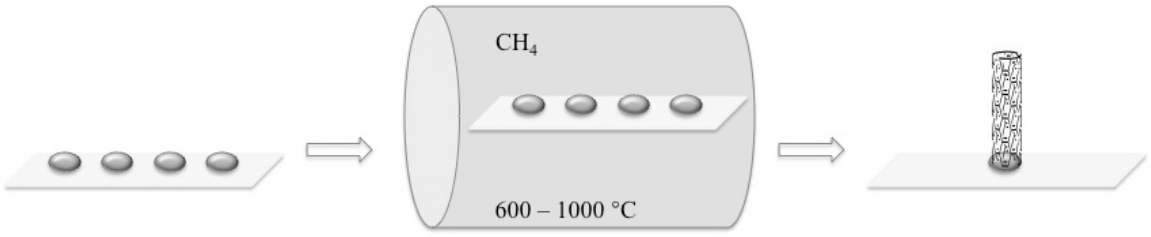

Figure 2. Synthesis of individual CNTs by CVD using clusters of catalyst particles deposited on a substrate. (Reprinted with permission from [1]. Copyright 2010 Momentum Press, LLC).

1.2.2.2 Synthesis of Single-walled Carbon Nanotubes

SWCNTs are also produced by the electric arc discharge method; for SWCNTs, however, a metal catalyst is required [5]. In 1993, Bethune *et al.* were the first to demonstrate that SWCNTs could be produced via arc discharge;[16] by using a carbon anode that contained a small percentage of Co catalyst—they discovered that SWCNTs were produced in the soot.

High-quality SWCNTs were fabricated by Smalley and co-workers, who employed laser ablation to generate nanotubes on a scale of 1–10 g.[17] In this method, a laser is employed to ablate a carbon target, which contains 0.5 at% Ni and Co and is in a tube-furnace. The furnace is heated to 1200°C, and during the laser ablation process, an inert gas carries the nanotubes down the tube, where they are collected on a cold finger. The nanotubes produced by this method consist of hexagonal-shaped ropes composed of tens of nanotubes, which are held together by van der Waals interactions.

A third method of SWCNT production involves CVD.[5] Unlike MWCNTs, high-quality SWCNTs are produced by CVD. As with MWCNTs, temperature, the choice of precursor, the flow conditions, and the metal catalyst play a key role in SWCNT synthesis. To create nanotubes that have both small diameters and no defects, the temperature for SWCNT production is higher than for MWCNT fabrication; the temperature usually ranges between 850 and 1000°C. Moreover, the carbon precursor of choice is methane, because this molecule undergoes the least amount of self-decomposition at high temperatures—therefore, the majority of the methane undergoes catalytic decomposition at the transition-metal nanoparticles.

Today, high-purity SWCNTs are produced commercially by a gas-phase chemical-vapor-deposition process referred to as the HiPco (high-pressure carbon monoxide) method.[18] In this process, SWCNTs are grown under both high pressure (~30–50 atm) and temperature (~900–

1100°C) in the presence of an iron catalyst. As carbon monoxide flows through the reactor, it undergoes a disproportionation reaction during which carbon dioxide and the atomic carbon for the SWCNT are formed. Moreover, the catalytic iron clusters are formed *in situ*. To achieve this result, iron pentacarbonyl, $Fe(CO)_5$, is added to the gas flow; upon heating, this iron species decomposes to form condensed clusters. Employing the HiPco technique, SWCNTs with a purity up to 97 mol% were produced at a top rate of 450 mg/h.

All existing synthetic methods yield SWCNTs as mixtures of different helicities, with only limited control of their diameters. There are ongoing active efforts to develop better synthetic procedures for controlled synthesis of SWCNTs. For example, using mesoporous materials as templates for SWCNT growth, nanotubes with tight diameter distributions have been produced. In one approach, SWCNTs were synthesized using Co, Fe/Co, and Rh/Pd alloy nanoparticles, which were positioned in the one-dimensional channels of a mesoporous material (folded sheets mesoporous material, FSM-16), by catalyst-supported chemical vapor deposition (CCVD).[19] In a second example, mesoporous Mo MCM-41 and Nb MCM-41 molecular sieves were synthesized in various ratios, and the calcined samples were used as catalysts for the growth of carbon nanotubes using CVD.[20] The single-walled carbon nanotubes had diameters ranging from 1.06 to 2.9 nm and from 1.08 to 2.3 nm when formed over Mo MCM-41 and Nb MCM-41, respectively. Additionally, uniform-diameter SWCNTs were grown in Co-substituted MCM-41 molecular sieves templated with C_{12} and C_{16} alkyl chains to result in pore diameters of 2.6 and 3.3 nm, respectively. Alternatively, Bertozzi and co-workers recently synthesized and characterized aromatic molecules called cycloparaphenylenanes, which are hoop-shaped chains of 9, 12, or 18 benzene molecules.[21] They hypothesized that this organic synthetic approach

could be developed into an efficient way of producing armchair carbon nanotubes of predetermined diameters.

While selective synthetic methods still remain an elusive target, recent years have witnessed significant progress in separation of as-produced SWCNTs. Duesberg *et al.* (1998) demonstrated that size-exclusion chromatography (SEC) could be employed to separate SWCNTs from metal nanoparticles and amorphous carbon, and this technique permitted SWCNTs to be divided by length.[22] Moreover, Zheng and Semke (2007) combined SEC with ion-exchange chromatography (IEC) to successfully isolate semiconducting SWCNTs of a defined length and chirality.[23] Bauer *et al.* (2007) not only separated dispersions of nanotubes based on length using SEC, they also employed an online viscosity detector to ascertain the intrinsic viscosity of the dispersion, which varies as a function of hydrodynamic size.[24] This permits one to differentiate SWCNTs by shape and has profound applications for differentiating functionalized SWCNTs. Density-gradient ultracentrifugation (DGU), on the other hand, represents an alternative method for separating as-produced SWCNTs. Green and Hersam (2007) employed an amphiphilic surfactant such as sodium cholate to disperse the SWCNTs in solution, and a linear density gradient was formed from varying concentrations of water and iodixanol ($C_{35}H_{44}I_6N_6O_5$).[25] After 12 hour of ultracentrifugation at 288,000 *g*, the SWCNTs formed distinctive colored bands, which could be isolated. The observed differences in color represent SWCNTs sorted by physical and electronic structure. Additionally, Yanagi *et al.* (2008) utilized sucrose as a gradient medium to separate metallic and semiconducting SWCNTs by DGU (sucrose-DGU).[26] Employing a low temperature and carefully controlling the concentration of surfactant, metallic and semiconducting SWCNTs were isolated with purities of 69% and 95%, respectively (as determined by optical absorption spectra).

1.2.3 Properties of Carbon Nanotubes

1.2.3.1 Physical and Mechanical Properties of Carbon Nanotubes

The structure of carbon nanotubes (CNTs), which are composed completely of sp^2-hybridized carbon atoms, endows these materials with unique properties. For example, CNTs have a tensile strength that is 100 times stronger than steel and 10 times stronger than Kevlar; at the same time, the elastic Young's modulus is 7 times that of steel.[27] Moreover, CNTs are lighter than aluminum while having a surface area up to 1500 $m^2\ g^{-1}$. Finally, CNTs remain thermally stable even at temperatures above 1000°C, and with a value of 6000 $W\ m^{-1}\ K^{-1}$, the thermal conductivity of a CNT is double that of diamonds.[27]

1.2.3.2 Electronic Properties

Metallic Versus Semiconducting Carbon Nanotubes

As discussed in Section 1.2.1, carbon nanotubes are characterized as being metallic (including semimetallic) or semiconducting, depending on the integers (*n, m*). As evidenced by Figure 3a and b, a significant amount of information can be ascertained from a plot of density of states (DOS) *versus* energy for both semiconducting SWCNTs (sem-SWCNTs) (Figure 3a) and metallic SWCNTs (met-SWCNTs) (Figure 3b). First, sharp spikes referred to as van Hove singularities characterize these plots.[14] Beginning at the Fermi level, the van Hove singularities are numbered as i = 1, 2, 3,…, and permissible optical/electronic transitions involve singularities across the Fermi level. By analyzing Figure 3a and b, one can ascertain that the two semiconducting transitions, S_{11} and S_{22}, lie between the first metallic transition, M_{11}. A major

difference between met-SWCNTs and sem-SWCNTs involves the conduction and valence bands of the material. For met-SWCNTs, the valence and conduction bands are continuous. On the other hand, there exists a band gap between the valence and conduction bands for sem-SWCNTs.

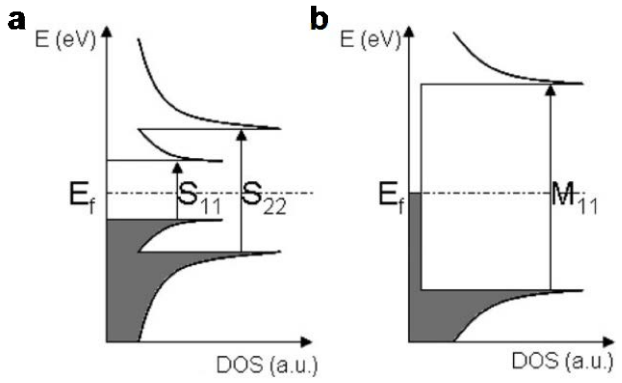

Figure 3. Energy diagram showing the density of states in (a) semiconducting SWCNT and (b) metallic SWCNT. Valence bands are gray, while conduction bands are white. (Reprinted with permission from [1]. Copyright 2010 Momentum Press, LLC).

Depending on the type of carriers, all semiconductors can be divided into two subcategories: *p* type and *n* type. Generally, under ambient conditions, a SWCNT will exhibit *p*-type characteristics, which permits the conduction of holes instead of electrons. It is believed that *p*-type behavior originates from oxygen absorbing to either the surface of the nanotube[28] or the electrode surface of the device.[29] On the other hand, SWCNTs can form an *n*-type semiconducting device, in which electrons are main carriers, when treated in vacuum or by doping a *p*-type nanotube with an electron-donating species or a species with small ionization energy.

Field-Effect Transistors (FETs)

In 1998, the Dekker[30] and Avouris[31] groups were the first to report the fabrication of nanotube field-effect transistor (NTFET) devices. NTFET devices consist of either a single semiconducting nanotube or a network[32] of nanotubes positioned between two conducting metal electrodes, the source (S) and the drain (D). A Si substrate forms the back gate of the device, which is insulated from the electrodes by a layer of SiO_2. Figure 4a and b depict a schematic and an atomic force microscope (AFM) image of a single semiconducting nanotube FET device.

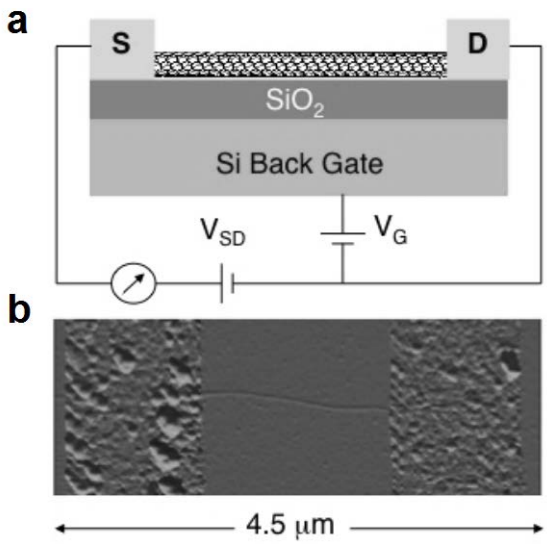

Figure 4. (a) Schematic diagram of a nanotube field-effect transistor device with a semiconducting SWCNT (black) contacted by two Ti/Au electrodes representing the source (*S*) and the drain (*D*) with a Si back gate separated by a SiO_2 insulating layer in a transistor-configured circuit. (b) AFM image of a typical NTFET device with individual SWCNTs connecting *S* and *D* electrodes. (Reprinted with permission from [15]. Copyright 2008 WILEY-VCH Verlag GmbH & Co. KGaA, Weinheim).

1.2.4 Chemical Modification and Functionalization of Carbon Nanotubes

In general, the doping of SWCNTs, like that of other graphene-based species, is amphoteric.[27] Therefore, based on the chemical nature of the dopant or the electrochemical potential applied, both electron and hole doping (*n* or *p* doping) are accessible. By doping a SWCNT, it is possible to raise the hole or electron and phonon thermal conductivity of the species by numerous orders of magnitude. Doping a CNT shifts the Fermi level, E_F; the density of states of the band structure, however, remains unchanged. Consequently, the population of the electronic states near the Fermi level changes as a result of the doping-induced shift, ΔE_F.

There are two major mechanisms of doping for CNTs. The first entails noncovalent methods, which involve endohedral doping and the adsorption of polymers and biological molecules to the sidewalls of the CNT. The second involves direct covalent bonding to the CNT through substitutional doping, numerous synthetic reactions, and the attachment of biomolecules to carboxylic defect sites on the SWCNT.

1.2.4.1 Noncovalent Functionalization

Endohedral Doping

Endohedral doping is the process whereby atoms, molecules, or clusters are encapsulated by CNTs.[27] Examples of the enclosed objects include empty fullerenes, endo-, and exohedral metallofullerenes, alkali metals, metal halides, hydroxides, and transition-metal oxides and complexes. The endohedral species functions as a dopant that confers new properties to the nanotube. For example, a new hybrid electronic band is generated by periodic arrays of C_{60} in

SWCNT. Additionally, a hybrid system with modified electronic and optical properties was generated from encapsulated metallocenes such as bis(cyclopentdienyl)cobalt.

Exohedral Functionalization

Exohedral noncovalent functionalization of CNTs involves wrapping with polymers and attaching molecules through π–π stacking (sticky labels).

Biological Molecules

CNTs are capable of forming noncovalent interactions with biological molecules, thereby producing a system with new electronic properties.[33] Proteins represent a class of molecules that have high affinity for the external sides of the nanotube walls. For example, it is believed that the hydrophobic domains of the protein streptavidin form strong interactions with the surface of the nanotube[34] or that this protein binds to the nanotube through charge-transfer interactions.[35] Because of the ability of its aromatic nucleotide bases to form π-stacking interactions with the sidewalls of carbon nanotubes, single-stranded DNA (ssDNA) also has a high affinity for CNTs.[36] This aspect has been exploited to disperse CNTs in aqueous solutions. Likewise, it has been demonstrated that starch can be employed to disperse SWCNTs in aqueous solutions.[37] Amylose, the linear component of starch, consists of α-1,4 linkages between D-glucopyranose residues; in aqueous solutions, this biological polymer forms left-handed helices. The diameter of the helices is variable, which permits a variety of guest molecules to form complexes with amylose. Iodine molecules initiate the formation of the cavity; SWCNTs subsequently dislodge the iodine molecules in a "pea-shooting" mechanism. The SWCNT interacts with the hydrophobic faces of the D-glucopyranose residues, and the hydroxy groups are positioned outward so that they may form hydrogen bonds with water molecules in the surrounding aqueous

solution and thereby promote dispersity. The driving forces for this process are a gain in enthalpy due to favorable van der Waals interactions between the CNT and amylose and an increase in entropy.

Wrapping CNTs with Synthetic Polymers

The three primary means by which CNT and polymers interact are π–π stacking, hydrophobic interactions, and charge transfer. Moreover, the physisorption of polymer molecules can alter the electronic state of a CNT. For example, poly(ethyleneimine) (PEI) causes *n*-type behavior when adsorbed to SWCNTs because of the electron-donating ability of the amine group; the electron transfer from the polymer to the CNT is confirmed by a 10 cm^{-1} downshift in the *G* band of the Raman spectrum.[27] Nafion, on the other hand, imparts on SWCNTs a *p*-type behavior when in a solvent consisting of deionized water and 1-propanol. It has been demonstrated that poly(metaphenylenevinylene) (PmPV), a conjugated luminescent polymer, exhibits enhanced properties when bound to CNTs by π–π stacking.[38] For example, CNT/PmPV composites demonstrated nearly an eightfold increase in electrical conductivity relative to PmPV alone, and the photo- and/or electroluminescence properties of PmPV were not affected by the CNT/polymer conjugation. O'Connell *et al.* (2001) employed poly(vinyl pyrrolidone) (PVP) and poly(styrene sulfonate) (PSS) to solubilize pristine SWCNTs in aqueous systems.[39] This process is favored thermodynamically, since the polymer minimizes the hydrophobic interactions between the SWCNTs and the aqueous solution. The polymer could be subsequently unwrapped from the nanotube by changing the solvent. Star *et al.* (2003) synthesized poly{(5-alkoxy-*m*-phenylenevinylene)-*co*-[(2,5-dioctyloxy-*p*-phenylene)-vinylene]} (PA*m*PV) tethers or rings that

represent pseudorotaxanes with matching rings or threads.[40] When SWCNT bundles were wrapped with PA*m*PV polymers, the nanotube bundles became soluble in organic solvents.

Imparting a florescent label on carbon nanotubes can be challenging. Covalently bonded fluorophores interrupt the π system of the sp^2 sidewall, and the noncovalent attachment of fluorescent molecules often requires the creation of bulky structures.[41] Moreover, both covalently and noncovalently bonded fluorophores have been quenched due to energy transfer to the surface of the nanotube. To overcome this problem, Didenko *et al.* created fluorescent CNTs by employing poly(vinylpyrrolidone)-1300 (PVP-1300) that had been labeled with various Alexa fluorescent dyes.[41] In the presence of 1% SDS, the fluorescently labeled PVP-1300 polymer wraps around the CNT, forming an ~2.5-nm-thick monomolecular layer that maintains its ability to fluoresce.

1.2.4.2 Covalent Functionalization

Substitutional Doping

The process of substitutional doping involves replacing some carbon atoms of a CNT with boron, nitrogen, silicon, or phosphorous.[27] Since boron has one less electron than carbon, its incorporation into a SWCNT generates localized states in the valence band that are below the Fermi level. These states are caused by the presence of structural holes, and as a result, boron-doped SWCNTs (B-SWCNTs) are *p*-type semiconductors. One type of nitrogen doping, on the other hand, can form three-coordinate bonds within the sp^2 network. The localized states are above the Fermi level due to the presence of excess electrons, so nitrogen-doped SWCNTs (N-

SWCNTs) exhibit *n*-type conduction. Through substitutional doping, one can create *n*- or *p*-type nanotubes that can subsequently be exploited for sensing applications.

Approaches to Synthesis

Various organic reactions have been employed to functionalize CNTs. Some examples include halogenation reactions, hydrogenation reactions, cycloadditions, radical additions, electrophilic additions, ozonolysis, and the addition of inorganic compounds.[33] Zhang *et al.* (2009) developed a series of modular zwitterion-mediated transformations that enable the functionalization of both nanotubes (SWCNTs and MWCNTs) and fullerenes.[42] CNT dispersions prepared by this method were stable for months. Additionally, the zwitterion reaction was employed to functionalize MWCNTs on a large scale (10 g) and was conducted under mild conditions (60°C, no strong acids or bases, and low pressure). There are several excellent review articles detailing covalent functionalization of CNTs[43-45] and fullerenes.[46-49]

Biological Molecules

Biological molecules are able to form covalent bonds with carboxylic acid defect sites on CNTs, and the bonding of these materials can create new bioelectric systems.[33] For example, biotin was covalently attached to a CNT. Alternatively, proteins have been covalently bonded to N-doped MWCNTs.[33] Finally, DNA strands were covalently linked to the carboxylic groups on the CNT by diimide activation.[33] In addition, nitrene cycloaddition, arylation employing diazonium salts, or 1,3-dipolar cycloadditions reactions have been employed to functionalize the sidewalls of CNTs and represent possible routes for biomolecule attachment.[50] Carboxylated CNTs can be coupled directly with amines in biomolecules employing N-hydroxy succimide (NHS) activation

followed by standard carbodiimide (EDC) peptide coupling chemistry.[50] For example, Yu *et al.* employed this methodology to link secondary antibodies to carboxylic acid functionalized CNTs.[51]

Solubility under physiological conditions is the first step in producing a biocompatible CNT.[52] To render a CNT soluble in aqueous solutions, substitution reactions can be employed to functionalize the walls of CNTs. Peptides, proteins, nucleic acids, and other therapeutic drugs subsequently can be linked to functionalized CNTs. For example, Bianco *et al.* (2005) covalently attached a B-cell epitope of the foot-and-mouth disease virus (FMDV) to a CNT functionalized with amine groups, and an *in vivo* assessment of the immunogenic properties of this peptide–CNT conjugate was performed.[52] It was determined that the FMDV peptide–nanotube conjugate induced an immune response; the concentration of peptide-specific antibodies was high for the peptide–CNT complex relative to the response to the control (the free peptide). In a second example, CNTs were employed for drug delivery. When selecting a drug delivery system, generally the design should augment the pharmacological and therapeutic profile of a drug.[53] To achieve this end, Bianco *et al.* first functionalized MWCNTs with a fluorescent probe, fluorescein, for cellular imaging, followed by an antibiotic, amphotericin B.[52, 54] Both molecules were attached to the MWCNTs by covalent bonds. The antibiotic-linked nanotubes entered mammalian cells with ease, did not exhibit toxicity, and the conjugated amphotericin B maintained its antifungal properties.

1.3 GRAPHENE

Graphene consists of a two-dimensional sheet composed of sp^2-hybridized carbon. Moreover, graphene represents the basic building block for three other important carbon allotropes; it is stacked to form three-dimensional graphite, rolled to form one-dimensional nanotubes, and wrapped to form zero-dimensional fullerenes.[55] Until 2004, when Geim and co-workers successfully isolated a single sheet of graphene from graphite by mechanical exfoliation, scientists believed that two-dimensional crystals were thermodynamically unstable at finite temperatures.[56] This discovery created a new material with unique thermal, electrical, and mechanical properties due to the long-range π-conjugated system.[55]

1.3.1 Synthesis of Graphene

Mechanical exfoliation, which employs cellophane tape to isolate a single sheet of graphene from graphite, represents a low-throughput method for producing high quality graphene flakes. The primary problem with mechanical exfoliation is scalability. Consequently, other methods have been developed with the objective of creating large quantities of high quality graphene for device fabrication (Figure 5). One technique involves the bottom up approaches of chemical vapor deposition (CVD) and epitaxial growth, where a carbon feedstock such as ethylene decomposes on a metal (*i.e.*, Ni or Cu) substrate. Although large areas (~ 1 cm^2) of graphene films have been grown on the metal substrates employing CVD,[57-59] it remains difficult to consistently produce a uniform, single layer of graphene employing this technique. Graphene can also be produced by reducing silicon carbide (SiC) at high temperatures (> 1100 °C);[60, 61] the

primary problem with this method is that only small flakes are produced. The final approach involves the creation of a colloidal suspension of graphite oxide, which is exfoliated to form graphene oxide (GO). GO is subsequently reduced either chemically[62-64] or by thermal annealing.[65, 66]

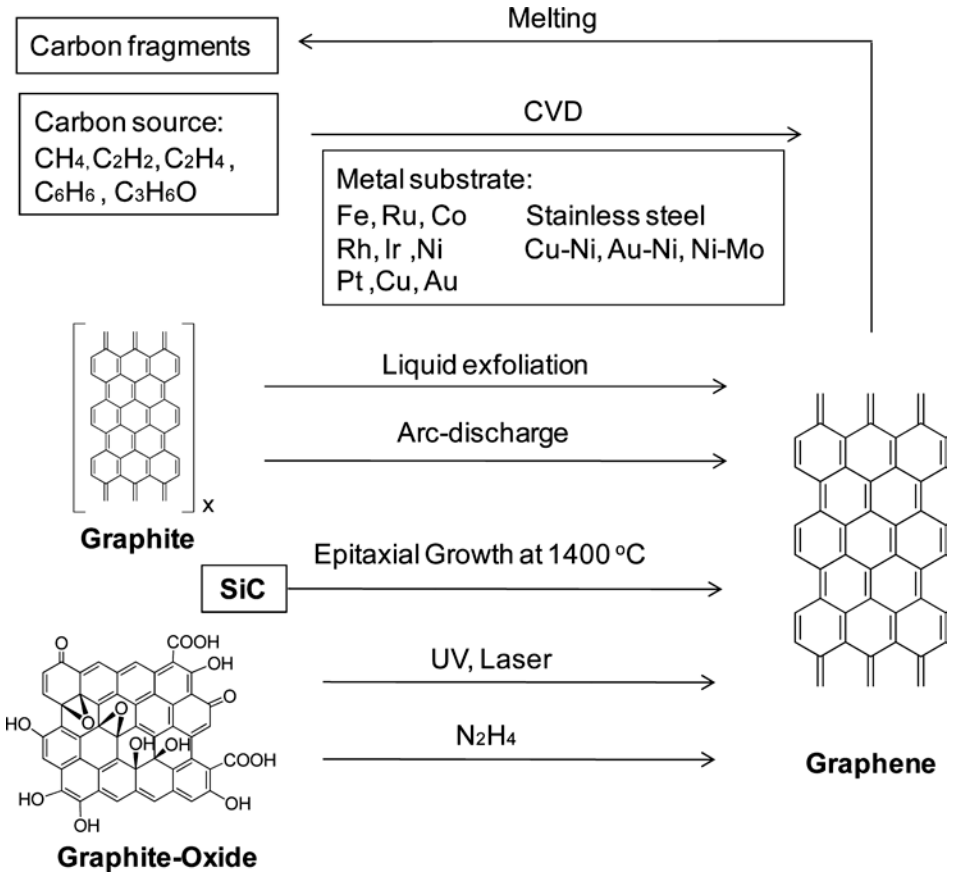

Figure 5. Synthesis of graphene. (Reproduced with permission from [67]. Copyright 2013 American Chemical Society).

1.3.2 Properties of Graphene

Based on experiments conducted on mechanically exfoliated graphene, it was discovered that graphene has unusual physical properties. First, graphene demonstrated the quantum Hall effect

at room temperature.[68-72] Moreover, graphene has ambipolar field-effect properties and high carrier mobility. These electronic properties originate from the high quality (*i.e.*, low number of defects) of graphene's two-dimensional crystal. Therefore, the former property implies that graphene can be used in field-effect transistors that are continuously tuned between electrons and holes based on the applied gate voltage. For a single layer of mechanically exfoliated graphene, the latter property has been measured to exceed 200,000 $cm^2/(V\ s)$.[73] Due to this high carrier mobility, the charge transport is essentially ballistic on the micrometer scale at room temperature. This has profound implication on the semiconducting industry, where the charge mobility of graphene would permit the fabrication of an all-ballistic device even at today's integrated circuit (IC) channel lengths (currently down to 45 nm).[55] Moreover, graphene was employed in a chemical sensor for the detection of a single molecule of analyte. This was possible due to graphene's two-dimensional structure, which represents the absolute maximum surface area to volume ratio for layered material and is essential for high sensitivity.[55] Also, due to graphene's ambipolar nature, the adsorption of either electron withdrawing or donating groups results in "chemical gating" of the material, which can be measured using resistive-based sensors.[55] The lack of selectivity remains the major obstacle to employing graphene in chemical sensors; functionalizing graphene's basal plane and edge with analyte-specific molecules may remedy this shortcoming. Finally, graphene has been employed for other applications, including: fuel cells, supercapacitors batteries, and solar cells.[67]

1.3.3 Functionalization of Graphene

To produce graphite oxide, strong mineral acids and oxidants oxidize graphite. Graphite oxide consists of stacked layers of graphene oxide; due to the hydrophilic nature of graphite oxide (*i.e.*, hydroxyl and epoxy functional groups) water becomes intercalated between the graphene oxide sheets (Figure 6a).[74] This enables graphene oxide to be exfoliated from graphite oxide *via* ultrasonication. While the structure of GO has been debated in the literature, the model recently ascertained by solid state ^{13}C nuclear magnetic resonance (NMR) holds that the sp^2 carbon network of graphene on the basal plane is converted to carbons with sp^3 hybridization to which epoxy and hydroxyl functional groups are bound.[75-78] In addition, carbonyl and carboxyl groups decorate the edge of the GO sheet.[75-78] The disruption of the sp^2 conjugation with surface defects (*i.e.*, phenolic and epoxy groups) renders GO electrically insulating.[79] The surface charge of GO is negative when dispersed in water as a result of the ionization of carboxylic acids and phenolic groups; consequently, the electrostatic repulsion between GO sheets prevents graphite oxide from reforming and permits a stable aqueous suspension to form.[80]

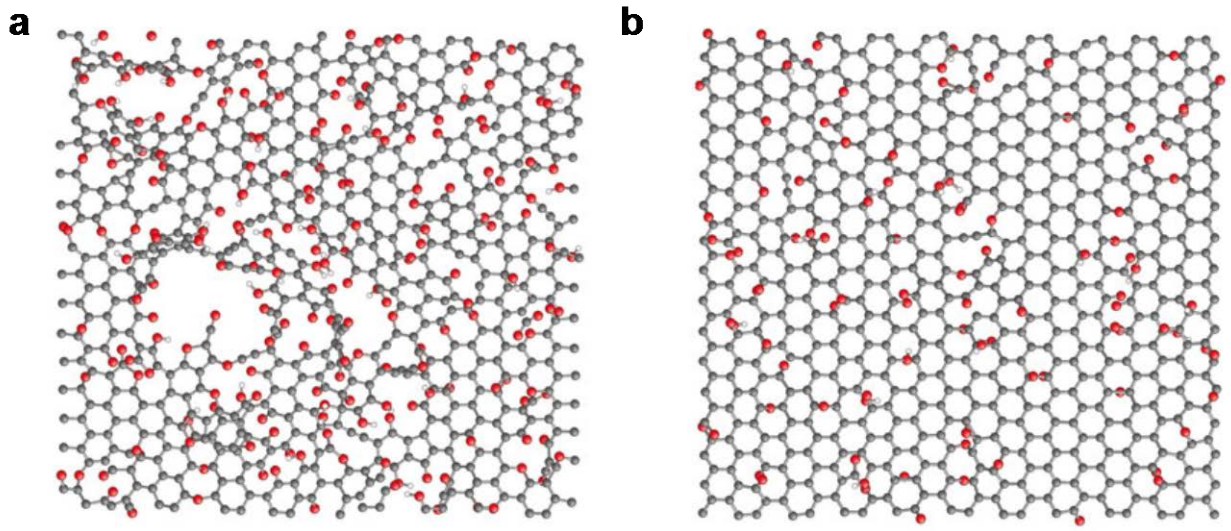

Figure 6. Morphology of (a) graphene oxide (GO) and (b) reduced graphene oxide (rGO). (Reproduced with permission from [81]. Copyright 2010 Macmillan Publishers Ltd.).

To restore electrical conductivity, the oxygen containing functional groups of GO must be reduced, which is typically accomplished by chemical (*i.e.*, chemically converted graphene (CCG)) and thermal means. During this process, most oxygen containing functional groups are reduced, and sp^2 hybridization is restored (Figure 6b).[62] When employing chemical means, hydrazine has become the reductant of choice;[62-64] other reducing agents such as dimethylhydrazine,[82] hydroquinone,[83] sodium borohydride[84] have also been utilized. To produce reduced GO by thermal annealing, graphite oxide is rapidly heated to 550°C.[66] Interlayer CO_2 pressure, which results from the decomposition of the epoxy and phenolic sites of graphite oxide, begins to build when the decomposition rate exceeds the diffusion rate of the evolved gases. Consequently, when the interlayer pressure exceeds the van der Waals forces holding the graphene oxide sheets together, exfoliation occurs. During the process, oxygen-containing moieties were reduced, and a sp^2 conjugated structure was restored.

1.4 CHARACTERIZATION OF CARBON NANOMATERIALS

1.4.1 Absorption Spectroscopy

In the ultraviolet (UV), visible (vis) and near infrared (NIR) wavelength, SWCNTs demonstrate well-defined electronic transitions; these permissible energy states are best represented by a density of states (DOS) diagram (refer to insets of Figure 7).[85] Employing a one-electron model, these transitions are most intense when the energy of the photon is in resonance with the energy difference between a given van Hove singularity.[85] As a consequence, the absorption spectra of an individual SWCNT will be composed of sharp features at energies E_{ii}, where i has the values 1, 2, 3,… (*i.e.*, for a given sub-band).[85] Absorption spectroscopy can be employed to gain insight into the electronic states of bulk SWCNT suspensions.[27] Since CNTs often form bundles while they are being synthesized, it is first important that they be exfoliated into individual structures. This is often accomplished by either encasing the SWCNTs in micelles using sodium dodecyl sulfate (SDS) or by wrapping them with polymers, either synthetic or natural, such as polycarbohydrides, peptides, or DNA. After a stable suspension of dispersed SWCNTs is obtained, a visible–near infrared (vis-near IR) absorbance spectrum affords three sets of peaks resulting from the van Hove singularities (refer to insets of Figure 7). For HiPCO SWCNTs, the bands are centered at 950–2000 nm, 700-950 nm, and 400-700 nm, which correspond to transitions arising from S_{11}, S_{22}, and M_{11} singularities, respectively (refer to Figure 7).

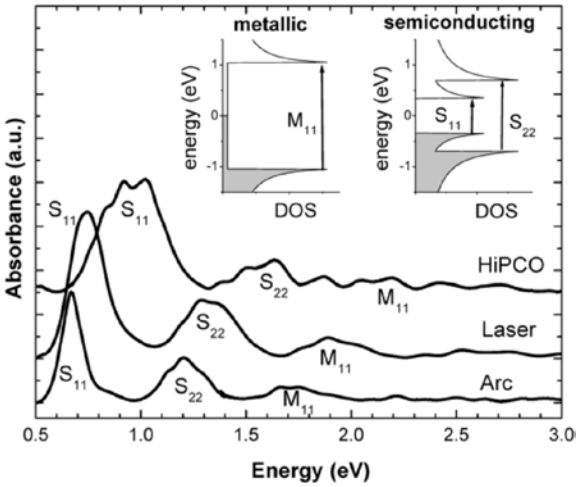

Figure 7. Electronic transitions between the energy bands of SWCNTs, observed by transmission spectroscopy of films. Inset depicts energy density of states (DOS) diagrams for metallic and semiconducting SWCNTs. (Reprinted with permission from [86]. Copyright 2002 American Chemical Society).

In contrast to SWCNTs, the absorption spectrum of graphene demonstrates only a single peak in the UV region (*i.e.*, ~230 nm) characteristic of the π-π* transition.

1.4.2 Fluorescence Spectroscopy

Individual semiconducting SWCNTs have the ability to fluoresce;[87] this is in contrast to bundles of SWCNTs that contain both metallic and semiconducting SWCNTs. The fluorescence for bundles of CNTs is quenched because the metallic SWCNTs provide an efficient nonradiative pathway for the photoexcited carriers produced by semiconducting nanotubes to relax.[27] For a suspension of nanotubes dispersed by SDS, the absorption and emission spectra for more than 30 different species have been recorded (Figure 8). Additionally, SWCNT fluorescence measurements are characterized by both Stokes shifts of <64.5 cm^{-1} and a fluorescence quantum yield of the magnitude of 10^{-4}.

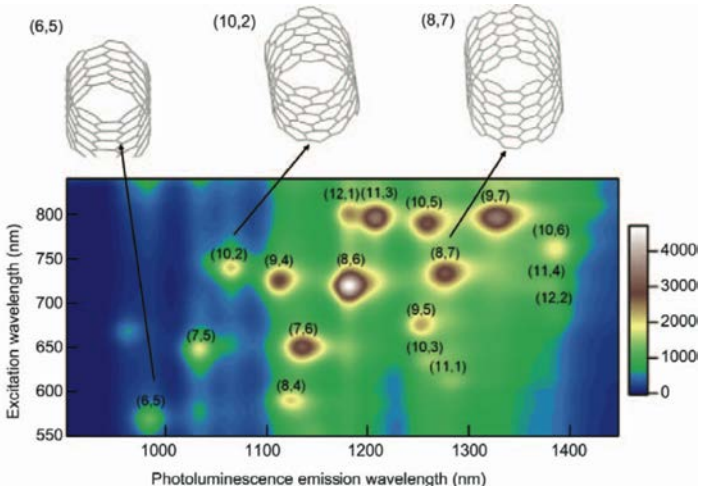

Figure 8. Photoluminescence excitation (S_{22}) and emission (S_{11}) spectrum of semiconducting HiPco SWCNTs. SWCNTs with different chiralities emit at various wavelengths under different excitations. The top panel illustrates the structures of three SWCNT chiralities. (Reprinted with permission from [88]. Copyright 2009 Springer).

1.4.3 Raman Spectroscopy

Historically speaking, Raman spectroscopy has played a vital role in the characterization of graphitic materials. Raman spectroscopy provides information regarding the nanotube diameter, chirality, curvature, and metallic *vs.* semiconducting behavior.[89] For CNTs, the G-band, D-band, the radial breathing mode (RBM), and G'-band (*i.e.*, the 2D) are the primary areas of interest (Figure 9). The G-band, which appears around 1582 cm^{-1}, arises from the stretching of C–C bonds in sp^2 hybridized carbon systems.[89] Due to curvature effects, multiple peaks appear in the G-band spectrum for SWCNTs, and this curvature dependence generates a diameter dependence that makes the G-band a probe for tube diameter.[89] Next, the D-band, which appears around 1300 cm-^{1}, results from the existence of disorder or defect sites in the sp^2 hybridized carbon network.[89] The RBM (100 to 450 cm^{-1}) is important for both the determination of the nanotube diameter and

relating the ω_{RBM} to the resonant optical transition energies E_{ii} for a given CNT.[89] Finally, the dispersive G'-band (also known as the 2D band) appears in the range of 2500-2800 cm^{-1}, and represents a second-order two-phonon process. Due to curvature-induced strain and quantum confinement, CNTs demonstrate special G'-band features, where the number of peaks depend on (*n*,*m*).[89] The G'-band can also be used to assign p-type or n-type doping for SWCNT.[89] Consequently, a rich treasure-trove of information can be gathered about CNTs by implementing Raman spectroscopy.

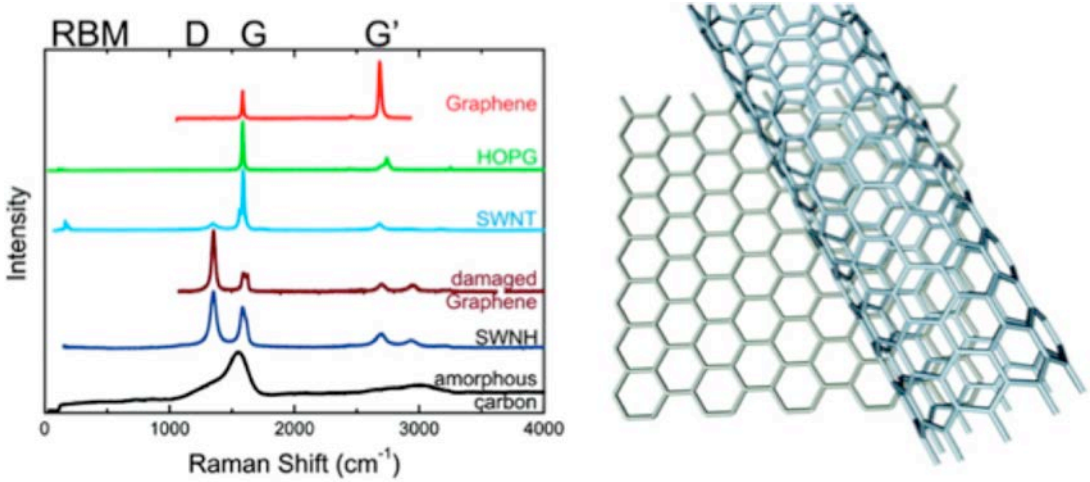

Figure 9. Raman spectra from different types of sp^2 hybridized nanocarbons, which are labeled. The main features (radial breathing mode (RBM), disorder-induced D band, the first-order Raman-allowed G band, and the second-order Raman overtones, G′) are identified. (Reproduced with permission from [89]. Copyright 2010 American Chemical Society).

The Raman spectra of graphene contain peaks at 1350 cm^{-1} (*i.e.*, the D band), 1580 cm^{-1} (*i.e.*, the G-band), and 2700 cm^{-1} (*i.e.*, the G'-band or 2D-band).[90] Moreover, the $I_{G'}/I_G$ provides insight into and represents a high-throughput methodology for elucidating the number of layers

contained within a graphene sample, where $I_{G'}/I_G \sim 2$ is indicative of a monolayer, $2 > I_{G'}/I_G > 1$ signifies a bilayer, and $I_{G'}/I_G < 1$ represents multilayers.[90]

1.4.4 Atomic Force Microscopy (AFM)

AFM was developed to overcome the inherent limitation of scanning tunneling microscopy (STM), namely STM is dependent on tunneling currents between a sample's surface and the tip.[91] As a result, STM must be implemented on electrically conductive surfaces. In contrast, AFM, which was developed for dielectric materials, measures a variety of tip/sample interactions.[91] For example, van der Waals interactions, which consist of permanent dipoles, induced dipoles, and electronic polarization, dominate at short distances; while long-range forces (*i.e.* electrostatic attraction or repulsion, current induced or static-magnetic interactions, and capillary forces due to the condensation of water between the sample and tip) become more significant when the tip/sample distance increases.[91]

The primary components of an atomic force microscope consist of a cantilever with a tip of nanometer dimensions, a laser aimed at the end of a cantilever, a mirror and a photodiode, which collects the reflection of the laser beam, and a 3D positioning sample stage consisting of an array of piezoelectrics.[91] For AFM imaging, the tip is scanned across the surface of a sample during which its topography is yielded through minute upward and downward deflections of the cantilever in order to maintain a constant force.[91]

Because AFM renders both the three-dimensional nanotopography and morphology of a sample with resolution that approaches a fraction of a nanometer and there exists no restrictions on what type of sample materials that can be analyzed, this characterization technique has been

widely employed for imaging nanomaterial.[92] In addition, AFM can be employed to ascertain mechanical (*i.e.*, the Young's modulus) and electrical (*i.e.*, I-V characteristic) properties of the nanomaterial.[92] AFM represents a powerful tool for studying the morphology (*i.e.*, the nanometric geometry), homogeneity, dispersibility, and purity of CNTs and the graphene family (*i.e.*, graphene, graphene oxide (GO), and few-layer graphene). For example, AFM has been employed to ascertain both the lengths and diameters distributions of CNT bundles (or individualized CNTs),[93] and this characterization technique has been employed to image functionalized CNTs (*e.g.*, polymer wrapped[38] and those functionalized by biomolecules such as proteins[94] and lipids,[95] refer to Figure 10a). Likewise, even with a theoretical thickness of 0.34 nm, AFM provides insight into the morphological feature of graphene, and the number of layers that are present in a sample can be elucidated by performing AFM imaging on an edge.[90] Under ambient conditions, however, a thin layer of water is present on the surface of graphene, which artificially inflates the thickness of the sample thereby resulting in measurements that range from 0.35 nm to 1 nm.[96] Finally, as a result of oxygen moieties, GO in water demonstrates a thickness between 1 to 1.2 nm (refer to Figure 10b), and the thickness of reduced graphene oxide in water has been given as approximately 1 nm. For both CNTs and graphene, AFM measurements represent a low throughput characterization technique.[97]

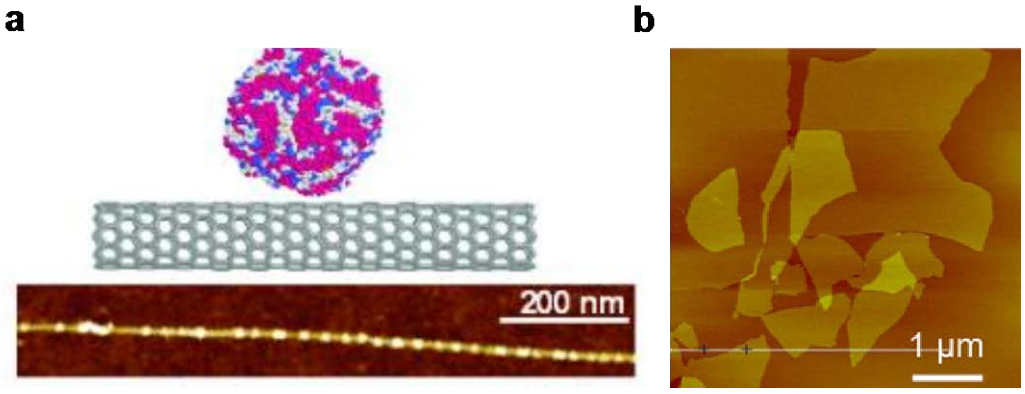

Figure 10. (a) Schematic illustration depicting a globular protein adsorbed to a SWCNT, and an AFM image showing a protein (*i.e.*, the bright dot-like structures) nonspecifically adsorbed to a nanotube. (b) AFM image of GO. (a reprinted with permission from [94]. Copyright 2003 The National Academy of Sciences. b reprinted with permission from [98]. Copyright 2010, Springer Science Business Media, LLC.).

1.4.5 Scanning Electron Microscopy (SEM)

To obtain an image by SEM, an electron beam that has a size of ~5 nm and an energy ranging from a few hundred eV to 50 keV is rastered over the surface of the specimen *via* deflection coils.[91] When the primary electrons strike the surface, electrons and photons are emitted from the sample; the emitted electrons are subsequently collected by a cathode ray tube (CRT) to yield an image.[91] Three types of SEM images are produced, including: secondary electron images, backscattered electron images, and elemental X-ray maps.[91] First, secondary electron images are generated from either inelastic scattering of high-energy primary electrons with atomic electrons or elastic scattering of high-energy primary electrons with the atomic nucleus.[91] To this end, during an inelastic collision between electrons, the primary electron transfers a portion of its energy to an electron comprising the sample; given sufficient energy transfer, the sample electron will be emitted.[91] Sample electrons that are emitted with energies less than 50 eV are

referred to as a secondary electron. The second image produced from SEM is comprised of backscattered electrons, which represent the high-energy electrons that are elastically scattered with essentially the same energy as the primary electrons.[91] Backscattering imaging is utilized to enhance contrast between regions of the specimen that differ widely in atomic number.[91] Finally, elemental X-ray maps result when primary electrons collide with and eject a core electron from an atom belonging to the sample, and the excited atom will decay to its ground state by emitting a characteristic X-ray photon, which can be employed for elemental identification (*i.e.*, *via* energy-dispersive X-ray spectroscopy, EDX).[91]

With magnifications ranging from 10 to 300,000 and a resolution of a few nanometers, SEM provides not only images of the morphology of nanostructured materials, but also detailed information regarding the chemical composition and distribution of the sample. Therefore, SEM represents an attractive technique for characterizing carbon nanomaterials (*i.e.*, CNTs and the graphene family, refer to Figure 11a and b) by providing insight into both morphology and purity.

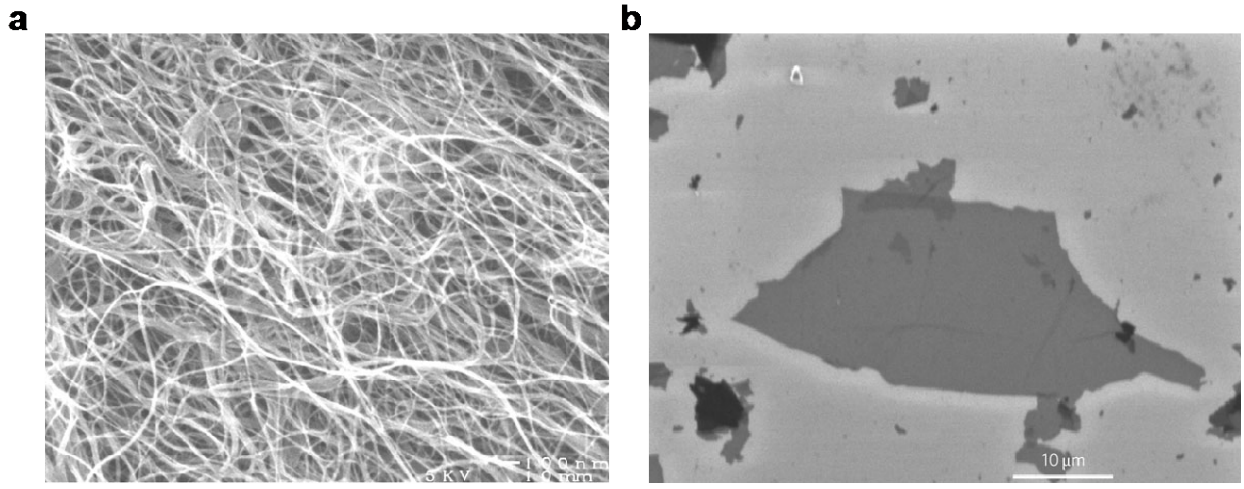

Figure 11. SEM image of (a) purified SWCNTs and (b) reduced graphene oxide (RGO). (a reprinted with permission from [93]. Copyright 1998, American Association for the Advancement of Science. b reprinted with permission from [63]. Copyright 2009, Nature Publishing Group.).

1.4.6 Transmission Electron Microscopy (TEM)

From a single sample, TEM affords imaging at high magnification (*i.e.*, in the range of 50 to 10^6) and provides diffraction information.[91] To this end, primary electrons are accelerated (*i.e.*, from 100 keV up to 1 MeV) and penetrate through a thin sample that is less than 200 nm thereby resulting in scattering of the sample electrons.[91] Elastic scattering, which involves no energy loss, gives rise to diffraction patterns.[91] On the other hand, "inelastic interactions between primary electrons and sample electrons at heterogeneities such as grain boundaries, dislocations, second-phase particles, defects, density variations, *etc*., cause complex absorption and scattering effects, leading to a spatial variation in the intensity of the transmitted electrons.[91]" High-voltage TEM instruments (*e.g.* 400 kV) not only afford a point-to-point resolution better than 0.2 nm, but also benefit from greater electron penetration through the sample. Because electron scattering

information originates from a three-dimensional sample that is projected onto a two-dimensional detector, the limited depth resolution is the primary shortcoming of TEM imaging.[91]

The crystal structure of either homogenous nanomaterials or different sections of inhomogeneous samples can be ascertained *via* selected-area diffraction (SAD), and employing a procedure similar to XRD, both Bravais lattices and other lattice parameters of crystalline materials are determined by the SAD patterns.[91] Finally, various spectroscopies have been developed in conjunction with TEM for the chemical composition analysis (*e.g.*, EDX and electron energy loss spectroscopy, EELS).[91]

When characterizing CNTs, high resolution TEM (HRTEM) represents a powerful microscopy technique, which facilitates the identification of diameter, number of walls, and inter-wall distances (Figure 12a). Also, the purity of the CNT sample can be ascertained *via* chemical composition analysis. With respect to graphene, TEM provides morphological information, and by imaging the edge of the graphene sample, this imaging technique assists in the counting of layers present in a sample (Figure 12b).[90] Finally, TEM can be utilized to obtain the selected-area diffraction pattern of graphene, which demonstrates a hexagonal arrangement that represents the crystal structure of graphene (Figure 12b).[90]

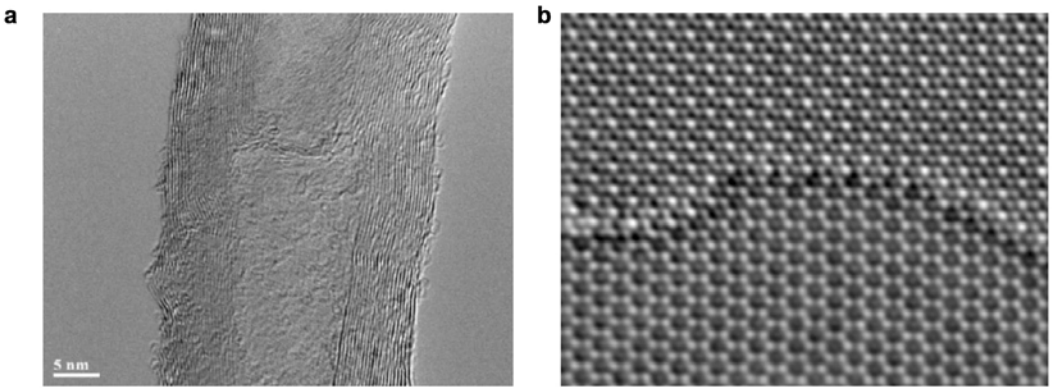

Figure 12. HRTEM micrograph of (a) a MWCNT and (b) edge of bilayer graphene. (a reprinted with permission from[99]. Copyright 2008, Elsevier B.V. b reprinted with permission from [100]. Copyright 2011, Nature Publishing Group.).

1.5 TOXICITY OF CARBON NANOMATERIALS

1.5.1 Toxicity of Carbon Nanotube

Initial reports on the effects of CNTs in relations to human health were incomplete and in some aspects confusing. *In vivo* studies revealed that CNTs that reached the lungs (in animal models) elicited a strong inflammatory and fibrotic reaction.[101-104] Moreover, it was observed that the introduction of MWCNTs into lung epithelial cells stimulated a genotoxic event.[105] Additionally, it has been reported that both SWCNTs and MWCNTs were responsible for causing cytotoxic responses and apoptosis during *in vitro* cellular studies.[106-109] At the same time, however, both *in vivo*[110-112] and *in vitro*[113-115] studies claimed that CNTs had low or no toxicity. A potential reason for the contradictory outcomes of these preliminary studies rests with the inhomogeneous nature of the CNT samples used during each experiment. Researchers

began to systematically examine certain aspects of CNTs to elucidate if CNTs are toxic and the source of this toxicity. These characteristics include: (i) the role of catalyst metals, (ii) length of CNTs, (iii) degree of oxidation/hydrophilic properties, and (iv) surface defects.

1.5.1.1 The Role of Catalyst Metals

Metal catalysts (usually Fe, Co, Ni, Al, or Mo) are employed during the synthesis of CNTs; this material can either be located on the surface of the CNT or encapsulated within the graphitic lattice.[116] It is possible to remove the metal catalyst from CNT by acid treatment[117] or heating at high temperatures.[118] In one study, the presence of the metal catalyst in commercially available CNTs resulted in an increase in the intercellular concentration of reactive oxygen species (ROS) and a reduction in the membrane potential of the mitochondria in rat NR8383 macrophages and human A549 lung cells.[114] This behavior disappeared when acid treated CNTs, which contained a low metal content, were introduced into the cells.[114] Likewise, there was greater oxidative stress and a reduction in antioxidant concentrations for Raw 264.7 macrophages after Fe containing CNTs (30% of total CNT mass) were introduced into the system relative to the response elicited by the iron-stripped CNTs.[119] Finally, a lower toxicity was reported when non-treated CNTs were incubated with keratinocytes, cells that compose 95% of the epidermis, and an iron chelator than when incubated without the chelator.[109] From these examples, it was demonstrated that the presence of transition metal catalysts facilitates the production of ROS, which can cause cellular oxidative stress. The mechanism for ROS production is likely similar to the Fenton reaction.

1.5.1.2 Length of CNTs

Experimental evidence indicates that the length of CNTs determines the level of toxicity. In one study, where chemically "cut" MWCNTs of two mean lengths (220 nm and 825 nm) were injected into the subcutaneous tissue of rats, an inflammatory response was observed.[120] The degree of inflammation, however, was lower for the 220 nm size MWCNTs due to the ability of macrophages to more readily engulf MWCNTs of smaller lengths. In another report, the mesothelial lining of the body cavity of mice was exposed to MWCNTs. The introduction of MWCNTs with lengths longer than 20 μm were characterized by inflammation, the formation of granulomas lesions, and asbestos-like pathogenic behavior.[121] In contrast, mice treated with short, tangled samples of MWCNTs elicited only a minimal inflammatory response. Again, this outcome was attributable to the ability of macrophages to envelope smaller MWCNTs. Therefore, there exists a length-dependent toxicity induced by CNTs that result from the ability of macrophages to perform phagocytosis.

1.5.1.3 Degree of Oxidation/Hydrophilic Properties

When compared to hydrophobic, pristine CNTs, increasing hydrophilic functionalities augments cytotoxicity. In one study, the presence of oxidized CNTs in a dose of 400 μg/mL (approximately 10 million CNTs per cell) induced apoptosis in T cells.[106] On the other hand, pristine (hydrophobic) CNTs were not nearly as toxic as the oxidized species. The reason for this behavior may stem from the fact that oxidized CNTs are water-soluble and therefore are better dispersed throughout the cell. Meanwhile, in an aqueous environment, pristine CNTs tend to aggregate. Under these conditions, one could foresee macrophages having greater ease isolating aggregated samples than one that is well dispersed. In a second experiment, CNTs,

carbon black, and carbon nanofibers were introduced into human lung-tumor cell lines. All of these materials were able to stimulate apoptosis and prevent proliferation; the effects were more pronounced as the aspect ratio decreased and the degree of functionality (oxygen containing functional groups) increased.[122] Therefore, as CNTs become more dispersible in aqueous environments through functionalization with hydrophilic groups such as hydroxyl, carboxyl, and carbonyl moieties, they become well dispersed in the cell. It thus became more difficult for the cell's defenses to eliminate this nanomaterial, and as a result, programmed cell death was induced.

1.5.1.4 Surface Defects

Surface defects on CNTs have been found to be the source of acute inflammation and genotoxicity. Experimentally, MWCNTs were heated to remove residual catalyst metals and subsequently placed in a ball mill to establish surface defects, which created dangling bonds.[123] These CNTs were subsequently injected into the lungs of female rats through intratracheal instillation for *in vivo* studies and introduced to immortalized rat lung epithelial cells for *in vitro* genotoxicity studies *via* cell media.[116] Due to the highly reactive nature of dangling bonds, two effects were observed. First, CNTs with surface defects were scavengers for ROS. Second, *in vivo* acute toxicity and *in vitro* genotoxicity appears directly related to surface defects. Interestingly, granulomas formed two months after exposure to both the ground and pristine (heated) MWCNTs, which indicate that long-term toxicological responses to CNT may develop independently of acute responses.[116] Consequently, it was determined that CNTs with surface defects induce acute inflammation *in vivo* and genotoxicity due to their ability to scavenge for ROS.

1.5.2 Toxicity of the Graphene Family

Despite the recent explosion in research relating to the graphene family (*i.e.* graphene, graphene oxide (GO), and few-layer graphene), there exists very little insight into the potential toxicity of this carbon nanomaterial, and Kostarelos and coworkers provide an excellent *Account* describing the current understanding of graphene toxicity, which is summarized herein.[124] Studies have demonstrated that small sheets of GO resulted in hemolytic activity; the addition of chitosan, which improved dispersity, largely eliminated this problem.[125] The amidation of GO, on the other hand, demonstrated hemocompatible even at high doses (*i.e.*, 50 μg/mL), and in contrast to GO, no pulmonary thrombosis was observed when amidated GO was injected into mice.[126] Furthermore, platelet aggregation resulted in the presence of GO but was not identified for amidated GO.[126] Taken together, these data provide empirical evidence that amidation of GO renders the nanomaterial more hemocompatible. Employing unmodified, multilayer graphene with large diameters (*i.e.*, 25 μm), Schinwald *et al*. reported respirable graphene particles were inflammogenic to the lungs and the pleural space.[127] Interestingly, Kostarelos and coworkers recently demonstrated there exists no evidence of *in vitro* cytotoxicity and *in vivo* pathogenicity for well dispersed, purified GO sheets.[128]

1.6 PEROXIDASES AND CARBON NANOMATERIALS

Recent reports have demonstrated that the plant peroxidase, horseradish peroxidase (HRP),[3, 129-133] and the animal peroxidases, myeloperoxidase (MPO)[3, 134-136] and eosinophil peroxidase

(EPO),[137] catalyze the degradation/biodegradation of carbon nanomaterials. The following sections will serve as an introduction to the peroxidases that drive the degradation of CNTs and graphene derivatives.

1.6.1 Introduction to the Peroxidases

Peroxidases, a class of enzymes, contain a heme active center that facilitates the oxidation of numerous xenobiotics as hydrogen peroxide (H_2O_2) is consumed.[138] The heme, which is usually comprised of a feriprotoporphyrin IX (Figure 13), contains four pyrrole nitrogens bound to the Fe(III) center.[138] Moreover, an imidazole side chain belonging to a histidine residue occupies the fifth coordination position on the proximal side of the heme, and on the distal side of the heme, the sixth coordination position is vacant.[138] Characterized by a smaller size (~300 amino acid residues), both plant peroxidases (*e.g.* horseradish peroxidase) and fungal peroxidases (*e.g.* yeast cytochrome *c* peroxidase) contain non-covalently bound heme groups; this contrasts the covalently bound heme groups encompassed within larger mammalian peroxidases (*e.g.* 576–738 amino acid residues).[138] Because genes that encode for five helices, a His heme ligand, an Asp or Asn ligand hydrogen-bonded to His, and a Ca^{2+} binding site are homologous in both plant and fungal peroxidases, there exists a strong likelihood that these species arose from a common ancestor.[138] On the other hand, mammalian peroxidases (*e.g.* myeloperoxidase and eosinophil peroxidase) were likely derived from different ancestral genes *versus* plant/fungal peroxidases.[138]

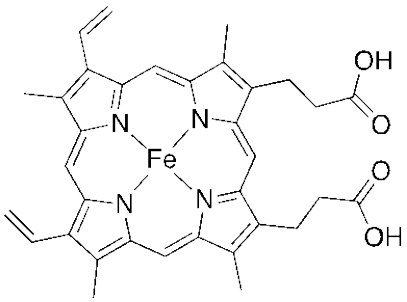

Figure 13. Schematic of the heme (feriprotoporphyrin IX) active site.

1.6.2 Horseradish Peroxidase (HRP)

1.6.2.1 An Introduction to the Enzyme

HRP (Figure 14b), which has been employed in applications ranging from biotechnology to bioremediation,[139] represents a monomeric enzyme that is secreted by the root hairs of the horseradish plant (*Armoracia rusticana*), where it is employed to synthesize cell wall components and metabolize hormones.[140] This enzyme contains a noncovalently bound ferriprotoporphyrin IX prosthetic heme group (Figure 13) as its active site.[140] When HRP is in its native resting state (*i.e.*, inactive form), the iron ion center of the heme group remains in the ferric, Fe(III), oxidation state. The heme (Figure 13) contains four pyrrole nitrogens bound to the Fe(III) center[138] and attaches to the enzyme *via* a coordination bond between the His170 residue (*i.e.*, the imidazole side chain) and the iron center on the proximal side of the heme group. The sixth coordination position is vacant during the resting state of the enzyme[138] and therefore represents the available binding site for hydrogen peroxide during enzymatic turnover.[139]

The heme group endows HRP with the ability to catalyze the oxidation of compounds such as phenols, biphenols, anilines, and benzidines over a wide range of pHs and temperatures.[141] Under neutral or basic conditions, the interaction of hydrogen peroxide (H_2O_2)

with the ferric species results in the formation of a transient intermediate that consists of a peroxide molecule bound to the heme iron. Two protein residues, His42 and Arg38, are responsible for the conversion of this ligand into Compound I, where His42 functions as an acid-base catalysis and Arg38 serves as a charge stabilizer. More specifically, His42, functioning as a Brønsted–Lowry base, abstracts a proton from O_α yielding Compound 0, which consists of an anionic Fe(III)-hydroperoxy complex.[142] This proton abstraction promotes the requisite charge separation to achieve a heterolytic cleavage of the O_α-O_β bond post nucleophilic attack at the heme, and coupled with a proton transfer from His42 to O_β, H_2O is released as Compound I, which is comprised of a ferryl oxo iron (Fe^{4+}=O) and a porphyrin π cation radical (Figure 14a, black pathway).[143] During this process, Arg38 (1) modulates the ionization state of His42 by decreasing the pK_a of the imidazole Nδ2 from around 6 to approximately 4 and (2) through electrostatic and hydrogen-bonding interactions involving His42 and the bound H_2O_2 (*i.e.*, the positively charged guanidinium side chain of Arg38 induces polarization of the O_α-O_β bond thereby facilitating its cleavage).[142] Compound I is reduced back to the ferric state in two sequential, one-electron steps during which the transient intermediate Compound II is produced (Figure 14a, black pathway). During this process, the porphyrin π cation radical is reduced resulting in the oxidation of the enzymatic substrate (AH_2) (Figure 14a, black pathway). A second enzymatic substrate undergoes oxidation when the ferryl oxo iron (Fe^{4+}=O) is reduced to the ferric state (Figure 14a, black pathway). The aforementioned process whereby enzymes that contain ferriprotoporphyrin IX prosthetic heme groups undergo oxidation from and subsequent reduction to the ferric state is referred to as the peroxidase cycle (Figure 14a, black pathway).[139]

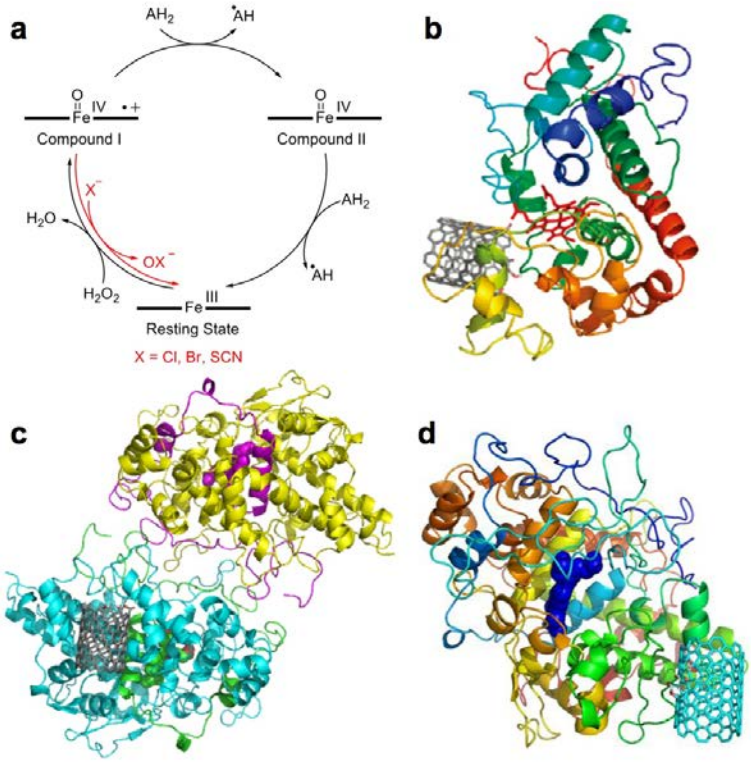

Figure 14. (a) The catalytic peroxidase cycle for HRP, MPO, and EPO. For MPO and EPO, compound I is reduced directly to the resting state *via* conversion of a halide to a hypohalite (red pathway). Molecular modeling of carboxylated SWCNTs binding to the active sites of (b) HRP, (c) MPO, and (d) EPO. (Reprinted with permission from [4]. Copyright 2013 Elsevier B.V.).

1.6.3 Horseradish Peroxidase (HRP) and Carbon Nanotubes

In an initial study, Star, coworkers, and collaborators demonstrated that HRP (Section 1.6.2) in the presence of H_2O_2 catalyzed the degradation of oxidized SWCNTs.[129] Specifically, oxidized SWCNTs, which were synthesized *via* the arc discharge method (Section 1.2.2.2), underwent morphological changes (shortening and deformation) when statically incubated at 4ºC in the presence of HRP and H_2O_2 (~40 μM).[129] In a following up mechanistic investigations, we

demonstrated that only SWCNTs that contained oxygen moieties/defect sites underwent enzyme-catalyzed degradation; pristine SWCNTs were not observed to degrade over the same time period.[130] Later, we extend our study of enzymatic oxidation employing HRP to SWCNTs synthesized by the high-pressure carbon monoxide (HiPco) method (Section 1.2.2.2).[144] HiPco SWCNTs enabled us to probe the material's electronic properties and chirality distribution employing photoluminescence (PL) mapping[145] for semiconducting SWCNTs and analyzing the radial breathing mode (RBM) section of the Raman spectrum for both semiconducting and metallic SWCNTs (Section 1.4.3). In contrast to earlier studies, our results demonstrated that incubation of highly defective, acid oxidized HiPco SWCNTs with HRP/H_2O_2 restored the optical properties of this nanomaterial. To this end, SWCNTs that were oxidized by a strong acid mixture and demonstrated weak absorption bands with no luminescence were further oxidized using HRP/H_2O_2 to yield shorter, less defective CNTs with well-defined absorption bands and strong luminescent signal. These shortened, fluorescent SWCNTs produced through incubating acid oxidized SWCNTs with HRP/H_2O_2 may find applications as NIR imaging agents/nanocarriers for use in theranostic applications.

1.6.4 Myeloperoxidase (MPO)

1.6.4.1 An Introduction to the Enzyme

Mature MPO (Figure 14c) exists as a cationic, homodimeric protein that is predominately expressed in granules of neutrophils (*i.e.*, a type of leukocytes).[146] With a mass of 146 kDa, MPO consists of two, 73 kDa monomers linked *via* a cysteine bridge at Cys153, and the identical dimers function independently.[146] Each monomer unit consists of a heavy chain, which has a

mass of 58.5 kDa, composed of 467 amino acid residues, underwent glycosylation, and contains a modified ferriprotoporphyrin IX active site. Also, the 14.5 kDa, 106 amino acid light chain is present.[146] Because the heavy chain is positioned at the bottom of a deep crevice, most materials except H_2O_2 and small anions cannot access the heme group; endogenous species (*e.g.* the amino acids tyrosine and tryptophan, thiols, ascorbate, steroid hormones, and urate), xenobiotics, and drugs are oxidized by MPO through binding in the hydrophobic pocket, which is located at the entrance of the distal heme cavity.[146]

In response to the phagocytosis of bacterium, MPO is released from the granules into primarily phagolysosomal compartment during which this peroxidase enzyme functions as a bactericide through the generation of both reactive radical intermediates (*i.e.,* formed *via* the peroxidase cycle, Figure 14a, black pathway) and oxidants that are formed during the halogenation cycle (Figure 14a, red pathway).[140, 147-149] EPR studies have demonstrated that Compound I, which contains a porphyrin π cation radical, decays into a protein radical with tyrosine (residues 7, 293, 309, 313, 316 and 557) and tryptophan (residues 47, 271, 513 and 514) functioning as the most probable residues responsible for the formation of the radical adduct.[150] These protein radicals fail to oxidize chloride ions into hypochlorous acid but retain the ability to oxidize classical peroxidase substrates.[150] During the halogenation cycle, Cl^-, Br^-, or the pseudohalide, SCN^-, donate two electrons to Compound I thus generating the ferric form of the enzyme, and, in turn, these substrates are converted into the corresponding (pseudo)hypohalous acids (HOX, such that X = Cl, Br, SCN).[151] Table 1 documents the physiological plasma concentrations of (pseudo)halides and the second-order rate constants for the formation of the (pseudo)hypohalous acids from Compound I and the (pseudo)halide substrate.

Table 1. Physiological Plasma Concentrations and Rate Constants of (Pseudo)Halides

(Pseudo)halide	**Plasma Concentration**[138]	**Rate Constant – MPO**[151,†] **(M^{-1} S^{-1})**	**Rate Constant – EPO**[151,†] **(M^{-1} S^{-1})**
Cl^-	140 mM	2.5×10^4	3.1×10^3
Br^-	20-100 µM	1.1×10^6	1.9×10^7
I^-	100-500 nM	--	--
SCN^-	20-120 µM	9.6×10^6	1.0×10^8
†**Measured at pH 7.0 and 15°C**			

1.6.4.2 Myeloperoxidase (MPO) Catalyzed Biodegradation of Carbon Nanotubes

In 2010, Kagan, coworkers, and collaborators demonstrated that human myeloperoxidase (hMPO, Section 1.6.4), which is expressed in granules of neutrophils (*i.e.*, a type of leukocytes), degraded oxidized SWCNTs.[134] After incubating carboxylated SWCNTs with hMPO in the presence of both H_2O_2 and Cl^- for 24 h, the dispersion appeared almost clear in color (Figure 15a). Moreover, the SWCNTs underwent structural deformation including both a decrease in size as revealed by dynamic light scattering (DLS) (Figure 15b) and an increase in defects as evidenced by the increase in the D/G band ratio, which was determined by Raman spectroscopy (Figure 15c). Degradation of the SWCNTs was also confirmed by the suppression of the metallic (M_1) and semiconducting (S_2) transition bands that characterize the vis-NIR absorption spectra for SWCNTs (Figure 15d). The control experiment, which excluded Cl^- and therefore relied only on the reactive intermediates that formed during the peroxidase cycle, demonstrated markedly less SWCNT degradation thereby suggesting the important role of the strong oxidant, hypochlorous acid (HOCl), in the degradation process. This finding was confirmed by the *in vitro* study by Vlasova *et al.*[135] Presumably, the synergetic effects of hypochlorite and the

reactive intermediates of MPO facilitated a much higher efficiency of CNT degradation for the MPO/H_2O_2/Cl^- system *versus* the HRP/H_2O_2 system. Of importance, small oxidants like HOCl have the ability to diffuse from active site and oxidize CNTs; the more bulky reactive intermediates, on the other hand, must be in close enough proximity of the CNT to promote degradation. Moreover, the enzyme-catalyzed oxidation of CNTs may be in competition with other substances that have lower redox potential (*i.e.*, more reductive), as shown in our recent study, where the enzymatic degradation of SWCNTs was mitigated by antioxidants added to the system.[152]

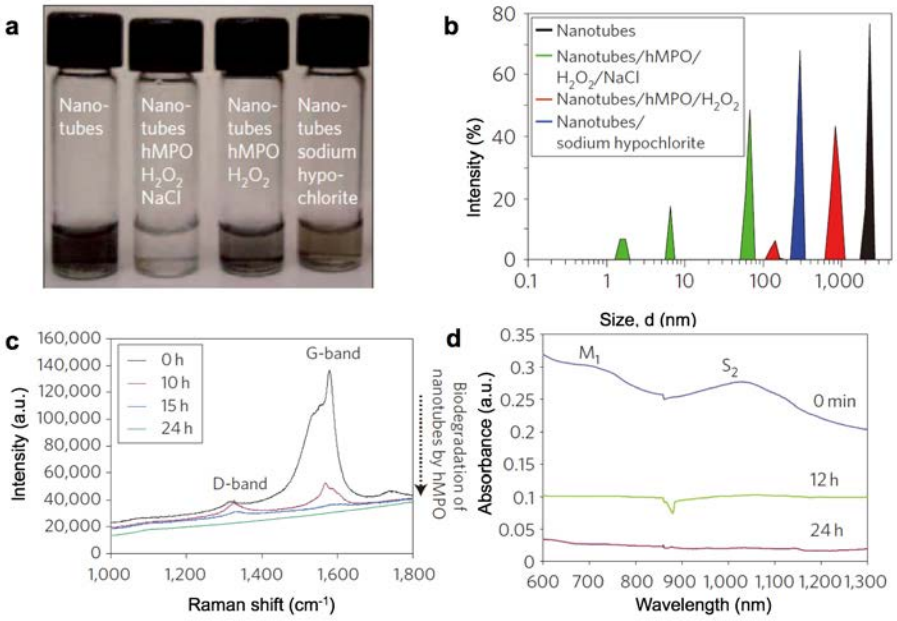

Figure 15. (a) Photographs of carboxylated single-walled carbon nanotubes (SWCNTs) incubated with or without degradative reagents after 24 h. (b) Dynamic light scattering data of different samples showing decreasing sizes of degraded nanotubes. (c) Raman spectra of SWCNTs before and after 24 h of degradation by MPO/H_2O_2/Cl^-. (d) Visible-near infrared (vis-NIR) absorption spectra of SWCNTs being degraded during 24 h. (Reprinted with permission from [4]. Copyright 2013 Elsevier B.V.).

1.6.5 Eosinophil Peroxidase (EPO)

1.6.5.1 An Introduction to the Enzyme

EPO (Figure 14d), which is expressed by eosinophils (*i.e.,* a type of leukocytes), assists in the destruction of invading parasites. Because, in general, parasites are larger than bacteria, eosinophils attach to these species and exocytose their granule contents, which is composed of EPO at 40% by mass. Interestingly, EPO possesses a 70% amino acid homology with MPO but weighs roughly half of the latter enzyme (*i.e.,* 69.8 kDa *versus* 146 kDa, respectively) and consists of both a 57.9 kDa heavy chain and a 11.9 kDa light chain.[151] Like MPO, EPO contains a ferriprotoporphyrin IX active site that can generate reactive radical intermediates by the peroxidase cycle (Figure 14a, black pathway) and (pseudo)hypohalous acids by the halogenation cycle (Figure 14a, red pathway).[151] For EPO, the second-order rate constants for the conversion of Br^- and SCN^- to the respective (pseudo)hypohalous acids (Table 1) are more than 32,000 and 6,000 times faster than the rate constant for the hypochlorous acid formation. Therefore, at neutral pH and physiological concentrations of Cl^-, Br^-, and SCN^-, MPO primarily generates HOCl and HOSCN while EPO chiefly generates HOBr and HOSCN.

1.6.5.2 Eosinophil Peroxidase (EPO) Catalyzed Biodegradation of Carbon Nanotubes

In a recent study, Fadeel, Kagan, and collaborators demonstrated that EPO (Section 1.6.4.2) also facilitated the degradation of oxidized CNTs.[137] Over 96 hours, in-test-tube experiments established that upon incubating human EPO (hEPO, added every 12 hours) with 100 μM H_2O_2 and 100 μM NaBr, which were added every 1 hour, degradation of the oxidized SWCNTs was visually observed as evidenced by the gradual fading of color that is characteristic of a SWCNT

dispersion (Figure 16a). This observation was substantiated by a decrease in the S_{22} characteristic band for SWCNTs in the NIR spectra (Figure 16b) and by transmission electron microscopy (TEM, Figure 16c). Therefore, the reactive intermediates and hypobromous acid generated by EPO through the peroxidase and halogenation cycles, respectively, successfully resulted in the degradation of oxidized nanotubes. Significantly, when lactoperoxidase (LPO) was incubated with H_2O_2 and Br^-, CNT degradation was observed confirming the strong oxidizing role of HOBr.[135]

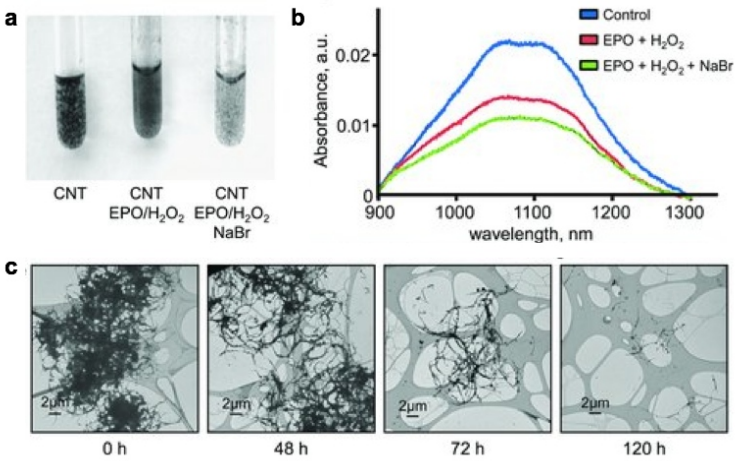

Figure 16. EPO-mediated degradation of carbon nanotubes. (a) CNT suspensions incubated as indicated are photographed after 96 h. (b) Absorbance in the S_{22} region normalized by subtraction of scattering after 96 hours for indicated conditions. (c) TEM analysis tracking the biodegradation of SWCNTs over time. Adapted with permission from [137]. Copyright 2013 WILEY-VCH Verlag GmbH & Co. KGaA, Weinheim).

1.6.6 Standard Reduction Potential of Reactive Intermediates of Peroxidase and Hypohalous Acids

Table 2 lists the standard reduction potentials for HRP, MPO, and EPO, and Table 3 details the two-electron standard reduction potentials of (pseudo)hypohalous acids.

Table 2. Standard Reduction Potentials Along the Peroxidase Cycle for Peroxidase Involved in CNT/Graphene Degradation/Biodegradation

Pathway	**Standard Reduction Potentials (*V*)**		
	HRP[150,†]	MPO[148,†]	EPO[148,†]
Compound I/ Resting State	--	1.16	1.10
Compound I/Compound II	0.898	1.35	--
Compound II/ Resting State	0.869	0.970	--
[†]Measured at pH 7.0 and 25°C			

Table 3. Two-electron Standard Reduction Potentials of (Pseudo)hypohalous Acids

Standard Reduction Potentials of Hypohalous Acids Produced by Peroxidases (*V*)[151,†]		
$HOCl/Cl^-$	$HOBr/Br^-$	$HOSCN/SCN^-$
1.28	1.13	0.56
[†]Measured at pH 7.0 and 25°C		

2.0 PEROXIDASE CATALYZED DEGRADATION OF CARBON NANOTUBES

2.1 CHAPTER PREFACE

Over the past 20 years, the unique electronic,[153] optical,[154] and mechanical[155] properties of carbon nanotubes (CNTs) have fuelled extensive, ground breaking research in areas such as electronics,[156] sensors,[15, 157] composite materials,[158] and energy conversion devices.[159] The full commercial potential of CNTs may not be realized, however, as a consequence of the possible pro-inflammatory and toxic effects of these carbon nanomaterials.[104, 119, 160-162] There exists a risk of human exposure as a result of either occupational or environmental exposure (*i.e.*, as products fabricated from CNTs degrade from wear over time). Since CNT contamination may induce a robust inflammatory response and severe oxidative stress that results in tissue damage,[163] it is necessary to address issues relating to CNT distribution/transformation, toxicity, and persistence.[164-168] To answer some of these questions, fundamental studies demonstrated that horseradish peroxidase (HRP),[3, 129-133] myeloperoxidase (MPO),[3, 134-136] and eosinophil peroxidase (EPO)[137] catalyze the degradation/biodegradation of carbon nanomaterials catalyzed the degradation of oxidized carbon nanomaterials. In this chapter, we detail our current understanding of the underlying mechanism of degradation. The material contained within this chapter was primarily reproduced from original works with permission from [3], [4], and [152].

2.2 EFFECT OF ANTIOXIDANTS ON ENZYME-CATALYZED BIODEGRADATION OF CARBON NANOTUBES

2.2.1 Preface

In this section, antioxidants were employed to elucidate further insight into the mechanism of peroxidase-catalyzed degradation of oxidized SWCNTs (o-SWCNTs). The material contained within Section 2.2 was published as an original research paper in the journal, *J. Mater. Chem. B*, and the figures have been reproduced with permission from [152].

List of Authors: G. P. Kotchey, J. A. Gaugler, A. A. Kapralov, V. E. Kagan, and A. Star.

Author Contributions: GPK, VEK, and AS conceived and designed the experiments, analyzed the data, and wrote the manuscript. GPK performed absorption, Raman, and fluorescence spectroscopies, transmission electron microscopy, and mass spectrometry. AAK performed florescence spectroscopy and electron paramagnetic resonance spectroscopy (EPR). JAG fabricated antioxidant-treated SWCNTs.

2.2.2 Introduction

The exact mechanism of enzyme-catalyzed biodegradation remains ambiguous; it has been hypothesized that the type of defects (*i.e.*, types of functional groups), enzyme-CNT interactions, and relative oxidative strength of the enzymatic system/generated oxidant *versus* the CNT contribute to the degradation process.[2] In this work, we studied the effect of two water-soluble antioxidants, L-ascorbic acid (AA) and L-glutathione (GSH), on MPO-catalyzed biodegradation of o-SWCNTs with and without Cl^- (Figure 17). The antioxidants were selected because they possess a lower redox potential than o-SWCNTs and therefore are more favorably oxidized by the enzymatic system.

Antioxidants serve as a natural defense system whereby cells are protected from reactive intermediates and oxidants (*i.e.*, "oxidative stress").[169] L-Ascorbic acid (vitamin C, AA), which is a six-carbon lactone derived from glucose by plants and most animals, functions as a scavenging water-soluble antioxidant that donates electrons sequentially resulting in the formation of the ascorbate radical and dehydroascorbic acid (DHA), respectively.[170] AA mitigates lipid peroxidation by both scavenging reactive oxygen species (ROS) and *via* the vitamin E redox cycle.[171] A second important endogenous water-soluble tripeptide antioxidant, L-glutathione (L-γ-glutamyl-L-cisteinylglycine, GSH), derives its antioxidant function from the thiol functional group (–SH) belonging to its cysteine residue.[172] While the oxidized dimer of GSH, glutathione disulfide (GSSG), represents the hallmark of oxidative stress, the enzyme, glutathione reductase, maintains glutathione primarily in its reduced active form (*i.e.*, GSH).[172]

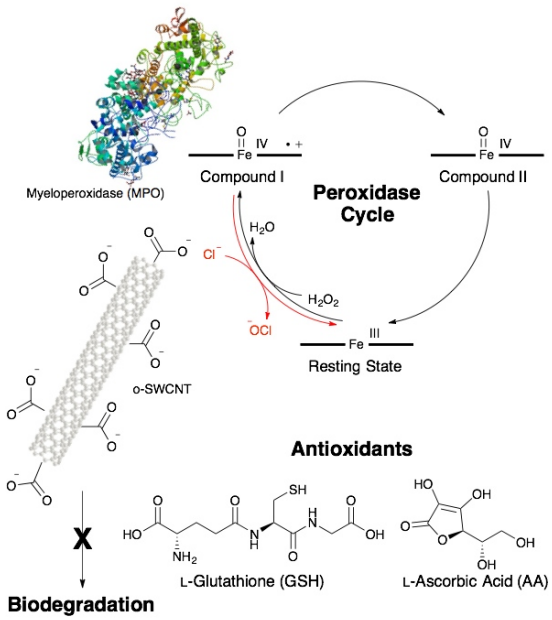

Figure 17. In the presence of hydrogen peroxide (H_2O_2), myeloperoxidase (MPO) biodegrades oxidized single-walled carbon nanotubes (o-SWCNTs) by two mechanisms: (1) reactive intermediates generated *via* the peroxidase cycle and (2) hypochlorite produced in the presence of chloride (Cl^-). When antioxidants such as L-ascorbic acid (AA) and L-glutathione (GSH) are added to the system, the biodegradation of o-SWCNTs is mitigated. (Reprinted with permission from [152]. Copyright 2013 Royal Society of Chemistry).

Myeloperoxidase (MPO), a heme-containing enzyme, is primarily expressed in polymorphonuclear cells (PMNs) of animals including humans.[147, 149, 173] Upon activation, these inflammatory cells release MPO from intracellular granules,[173] where this enzyme exists in millimolar (mM) concentrations,[174] to either intraphagosomal or extracellular spaces. MPO is subsequently oxidized by H_2O_2 from its Fe(III) resting state to MPO-Compound I, and in the presence of chloride (Cl^-, 80 mM for PMNs and 140 mM in plasma),[174] which represents a competitive substrate for the enzyme, MPO-Compound I is reduced back to the ferric resting

state during which Cl^- undergoes a two-electron oxidation to form hypochlorous acid (HOCl, Figure 17). This oxidant, which has a pK_a of 7.6,[173] exists as both HOCl and the hypochlorite ion (^-OCl) at physiological pH (*i.e.*, 7.4). Moreover, with a high redox potential of 1.28 V,[175] HOCl indiscriminately oxidizes invading bacteria and biologically significant macromolecules; therefore, HOCl is integral to the innate immunity[173] in the former case and contributes to oxidative stress in the latter scenario. Because hypochlorite has the ability to introduce acid "defects" onto the surface of CNTs[176] and MPO catalyzes the biodegradation of these carbon nanomaterials,[26, 27] acquiring further insight into the mechanism of biodegradation will potentially provide new understanding of the distribution/transformation, toxicity, and persistence of CNTs.

2.2.3 Results and Discussion

2.2.3.1 Transmission electron microscopy (TEM)

o-SWCNTs that contained carboxylic acids between 1.0 and 3.0 atomic%[177] and were initially around 1 μm in length (Figure 18a) were incubated at 37 °C with MPO and H_2O_2 for four days in the presence and absence of Cl^-, and the samples were inspected by transmission electron microscopy (TEM). In the presence of Cl^-, the micrographs display only residual carbonaceous material thereby marking the absence of tubular structures and indicating biodegradation (Figure 18b). In the absence of Cl^-, TEM micrographs denote the presence of shortened nanotubes and carbonaceous material (not shown). Next, the initial system was supplemented with either AA or GSH (1 mM/addition) during a four day time course at 37 °C. Significantly, in the presence of Cl^-, the TEM micrographs indicate that both antioxidants preserve the nanotubes' cylindrical

structures, and most of the nanotubes exist on the grid as large aggregates Figure 18c and d). This observation is likewise noted for the system without Cl^- and with antioxidants (not shown).

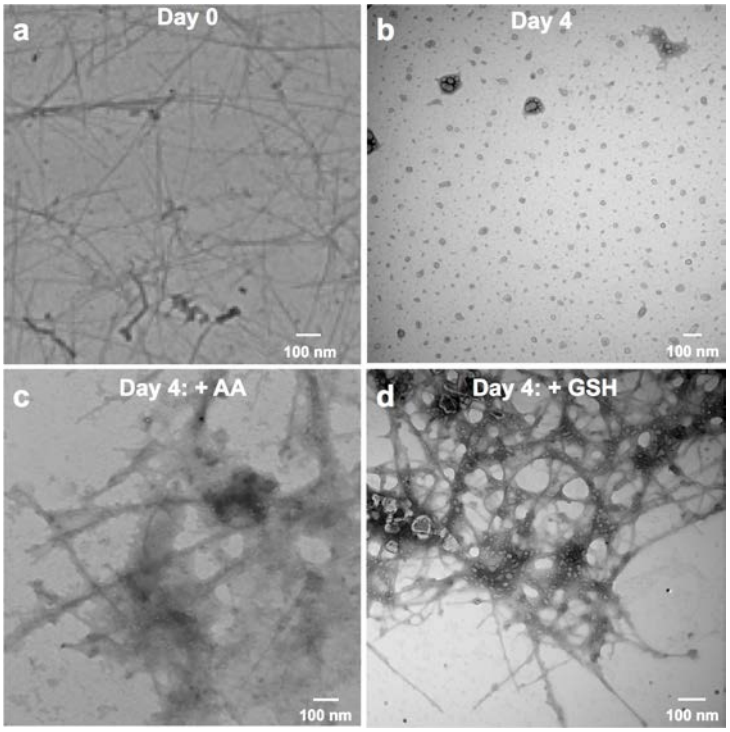

Figure 18. Micrographs obtained by transmission electron microscopy (TEM) of o-SWCNTs dispersed in a 0.1 M phosphate buffer (pH 7.4) with 125 nM myeloperoxidase (MPO) and 140 mM NaCl at (a) day 0 and (b) day 4; 8 additions of H_2O_2 (75 µM, final) were added daily. Micrographs of o-SWCNTs under identical conditions as (b) plus either (c) L-ascorbic acid (AA, 1 mM/addition) or (d) L-glutathione (GSH, 1 mM/addition). Reprinted with permission from [152]. Copyright 2013 Royal Society of Chemistry).

2.2.3.2 Raman spectroscopy

The data obtained from Raman spectroscopy reinforces the TEM observations. For o-SWCNTs, distinct peaks are noted for the radial breathing mode (RBM, 147 cm^{-1} and 159 cm^{-1}), D (1348 cm^{-1}), G (1592 cm^{-1}) and 2D (2643 cm^{-1}) bands (Figure 19A, blue curve),[89] and o-SWCNTs possess a D/G ratio of 0.53. For the MPO/H_2O_2 system with Cl^-, there is an absence of the characteristic Raman signature that is indicative of SWCNTs, however, thereby signifying that

the o-SWCNTs are completely biodegraded (Figure 19a, green curve). For enzymatic conditions without Cl^-, the RBM and D, G, and 2D bands are observed demonstrating the presence of o-SWCNTs (Figure 19a – red curve, and Figure 32); the RBM and 2D bands, however, are stifled relative to the spectrum for o-SWCNTs. Moreover, the D/G ratio increased from 0.53 to 0.65 as a result of o-SWCNT biodegradation by reactive intermediates. This increase in the D band is indicative of increased disorder in the sp^2-hybridized carbon system.[89] Finally, with the retention of the RBM and D, G, and 2D bands, the Raman signatures for o-SWCNTs treated with either antioxidant and with or without Cl^- mirror that of o-SWCNTs (Figure 19a and Figure 32) and provide further indication that the nanotube structure is conserved in the presence of antioxidants.

Examining the RBM provided additional insight into the mechanism of o-SWCNT biodegradation. Given that a laser with a 633 nm wavelength was employed, the resonant Raman scattering signals was primarily obtained from metallic nanotubes because the energy of the M_{11} optical transition is close to the energy of the photon generated by the laser.[178] Initially at day 0, two main peaks at 159 cm^{-1} and 147 cm^{-1} were observed (Figure 19b, blue curve). These peaks can be assigned to metallic o-SWCNTs with calculated diameters around 1.41 and 1.52 nm, respectively, when using the equation:

Equation 2: ω_r (cm^{-1}) = 223.75 (cm^{-1} nm)/*d* (nm).

Under Cl^- conditions, all of the nanotubes, regardless of chirality, appeared to degrade, and no RBM features remained after one day (Figure 19b, green curve). In the absence of Cl^-, the biodegradation resulting from reactive intermediates proceeded at a slower rate as evidenced by examination of the RBM (Figure 19b, red curve). The remaining peak was centered at 170 cm^{-1}, which may be attributed to an upshift in the RBM for the 1.41 nm diameter o-SWCNTs by

~11 cm^{-1}. This upshift, which results from a decrease in the energy spacing between van Hove singularities,[178] could be explained by either enzymatic selectivity for larger diameter nanotubes or further oxidation of the o-SWCNTs by the reactive intermediates of MPO. Such an upshift has been documented in the literature for the RBM of o-SWCNTs *versus* as prepared SWCNTs;[178-181] however, there exist conflicting explanations regarding the cause of this observation.

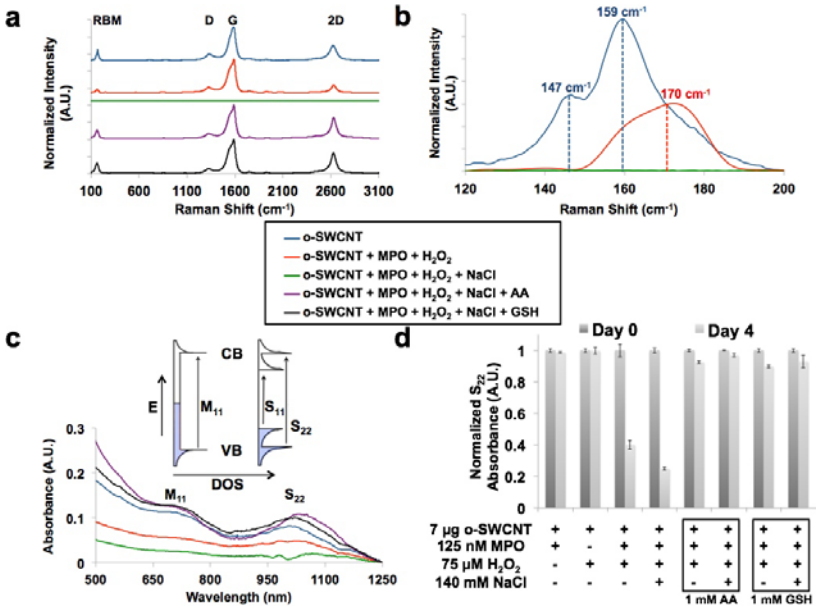

Figure 19. (a) Raman spectroscopy performed on key o-SWCNTs samples (o-SWCNT: blue, o-SWCNT + MPO + H_2O_2: red, o-SWCNT + MPO + H_2O_2 + NaCl: green, o-SWCNT + MPO + H_2O_2 + NaCl + AA: violet, and o-SWCNT + MPO + H_2O_2 + NaCl + GSH: black) for 4 days under experimental conditions. The radial breathing mode (RBM), D, G, and 2D bands are identified. (b) The radial breathing mode (RBM) region of the Raman spectra. (c) vis−NIR absorption spectra for o-SWCNTs samples identified in (A). The inset depicts the density of states (DOS) diagrams for metallic (left) and semiconducting (right) SWCNTs in which the optical transitions arising from van Hove singularities. The S_{22} and M_{11} transitions are identified on the spectra. (d) The S_{22} absorption intensity of o-SWCNTs at day 0 and day 4 for the given experimental conditions. This data was obtained from a microplate reader, and the error bar represents standard error of the mean with a sample size of three. Reprinted with permission from [152]. Copyright 2013 Royal Society of Chemistry).

2.2.3.3 vis-NIR absorption spectroscopy

The vis-NIR absorption spectrum of o-SWCNTs demonstrates distinct characteristic S_{22} and M_{11} transitions (Figure 19c – blue curve, and inset); after four days under enzymatic/peroxide conditions and in the presence of Cl^-, however, the S_{22} and M_{11} transitions are severely subdued (Figure 19c, green curve), which is indicative of biodegradation. Given the equal concentrations of o-SWCNTs, degradation was quantified by integrating the S_{22} peak relative to the baseline (Figure 33 and Table 5). The S_{22} peak area for o-SWCNTs in the presence of Cl^- was reduced 4.1 times compared to o-SWCNTs. In the absence of Cl^-, retention of the S_{22} and M_{11} transitions is apparent albeit subdued (Figure 33 and Table 5), which is demonstrated by the reduction of S_{22} peak area of only 2.7 times. This result is consistent with the TEM and Raman data, which indicate that the o-SWCNTs are degrading at a slower rate *via* reactive intermediates. The absorption spectra for o-SWCNTs incubated with MPO/H_2O_2, either antioxidant, and in the presence and absence of Cl^- demonstrate the retention of the S_{22} and M_{11} bands thereby signifying the presence of o-SWCNTs (Figure 19c, Figure 33, and Table 5). In the presence of Cl^-, the ratios of the S_{22} peak areas are 0.77 and 1.0 for o-SWCNTs relative to AA and GSH treated o-SWCNTs, respectively, and 0.84 and 1.1, respectively, in the absence of Cl^-.

Finally, a microplate reader was employed to obtain high throughput absorption readings at/near the S_{22} absorption transition for multiple samples and controls, and the resulting data further corroborated the results obtained by TEM and both Raman and vis-NIR spectroscopies. It is worth noting that in the range of 800 nm and 1300 nm, the scattering effect of CNTs is minimal (*i.e.*, <8%);[182] therefore, >92% of the signal obtained for the S_{22} band is derived from CNT absorption. Figure 19d portrays a 75% and 60% decrease in the S_{22} absorption intensity at day 4 relative to day 0 in the presence and absence of Cl^-, respectively. On the other hand, the

controls for o-SWCNTs declined by an insignificant amount over the same time period (Figure 19d and Figure 34). Figure 19d also demonstrated a minimal decline in S_{22} absorption intensity at day 4 relative to day 0 for AA or GSH with and without chloride. Therefore, both antioxidants significantly suppressed both hypochlorite-induced biodegradation and degradation resulting from reactive intermediates generated by the peroxidase cycle (Figure 17). We also compared the effects of changing antioxidant concentrations on o-SWCNT degradation as measured by the relative change in S_{22} absorption in both the presence and absence of Cl^- (Figure 38). Lower concentrations of antioxidants (~200 µM for AA and ~50 µM for GSH) per additions demonstrated the same level of protection against HOCl afforded by 1 mM additions of either AA or GSH.

2.2.3.4 Additional characterization techniques

Electron paramagnetic resonance (EPR) spectroscopy and positive mode electrospray ionization – mass spectrometry (ESI-MS) were employed to qualitatively confirm the oxidation of AA and GSH, respectively, under chloride conditions. EPR spectroscopy confirmed the formation of the ascorbate radical after 1h incubation under experimental conditions (Figure 35). Moreover, in the presence of Cl^-, glutathione sulphonic acid (GSO_2OH) and glutathione disulfide (GSSG) were observed at a m/z of 356 and 613, respectively, utilizing ESI-MS (Figure 36).

2.2.3.5 Potential mechanism – why is HOCl more efficient at biodegradation than reactive intermediates?

As previously demonstrated, both samples, which consisted of o-SWCNTs that were incubated at 37 °C with MPO and H_2O_2 for four days in the presence and absence of Cl^-, degraded;[7] the

degree of degradation, however, was dependent on the strength of the oxidant. HOCl is produced in the presence of chloride (Figure 17) and possesses a redox potential of 1.28 V, which is greater than the mean redox potential for the reactive intermediates of MPO (E^0 = 1.16 V) that form during the peroxidase cycle (*i.e.*, in the absence of chloride, Figure 17).[3] Consequently, as demonstrated in Figure 20a, both species are able to oxidize SWCNTs (E^0 = 0.5 V).[3] Compared to HOCl induced degradation, however, o-SWCNTs biodegradation catalyzed *via* reactive intermediates was less efficient as demonstrated by the TEM, Raman spectroscopic, and vis-NIR spectroscopic data. Molecular simulations studies provide a second possible justification for the lower biodegradation efficacy of reactive intermediates.[134] When dispersed in an aqueous media at physiological/experimental pH (*i.e.*, pH = 7.4), the carboxyl groups of the o-SWCNTs, which have a pK_a of approximately 5.5,[183] will be deprotonated as demonstrated by a zeta potential of approximately −50 mV.[184] Additionally, with an isoelectric point greater than 10,[185] MPO will be protonated and highly cationic at pH 7.4. Therefore, to degrade o-SWCNTs employing reactive intermediates, the negatively charged carboxyl groups of o-SWCNTs must interact with the positively charged arginine residues of MPO *via* electrostatic interactions in such a fashion that the nanotube is properly oriented towards and in close enough proximity to the proximal end of the heme group, which involves the catalytically active tyrosine residues, Tyr 293 and 313.[134] It is hypothesized that these radical supporting aromatic residues catalyzed the cleavage of o-SWCNTs.[134] On the other hand, in the presence of Cl^-, HOCl will diffuse through the solution and oxidize species of lower redox potential such as SWCNTs (Figure 20a).

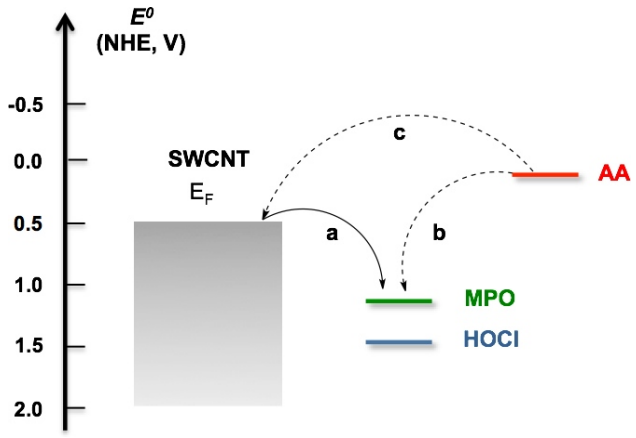

Figure 20. With greater redox potentials, HOCl (E^0 = 1.28 V) and the reactive intermediates of MPO (E^0 = 1.16 V) will oxidize (a) SWCNTs (E^0 = 0.5 V) and (b) ascorbic acid (AA, E^0 = 0.066 V). (c) In the absence of these oxidative species, SWCNTs can react with AA as observed by the Raman data. Reprinted with permission from [152]. Copyright 2013 Royal Society of Chemistry).

2.2.3.6 Potential mechanism – do AA and GSH reduce o-SWCNTs?

During the formation of o-SWCNTs *via* harsh chemical oxidants, hydroxyl, carbonyl, and carboxyl groups are generally imparted on the edges and sidewalls of nanotubes.[186] Moreover, it has been demonstrated that AA[187] and GSH[188] can significantly reduce most oxygen functional groups of graphene oxide resulting in a more pristine structure. Interestingly, we observed that the D/G ratio decreased for o-SWCNTs treated with antioxidants (from 0.53 for o-SWCNTs to 0.30 and 0.31 for o-SWCNTs incubated with either AA or GSH, respectively); a similar decline in the D/G ratio was observed for CNTs that were thermally annealed under vacuum, which results in the removal of functional groups.[189] For a system consisting of reactive intermediates, HOCl, and o-SWCNTs, we would expect the antioxidants to reduce the former two species before the SWCNTs as a consequence of their higher redox potential (Figure 20b). For each addition, the antioxidant was present in higher concentration than H_2O_2; therefore, the excess antioxidant would be able to react with the o-SWCNTs (Figure 20c). Because SWCNTs with

more pristine structures undergo less efficient MPO-catalyzed biodegradation,[134] there exists the possibility that the antioxidants were making the CNTs more pristine thereby mitigating biodegradation. To test this hypothesis, o-SWCNTs that were treated with AA or GSH for four days at 37 °C were subsequently incubated at 37 °C with MPO and H_2O_2 for four days in the presence and absence of Cl^-. Employing the microplate reader, it was determined that the S_{22} absorption transition intensity decreased by 70% and 65% for AA and 64% and 49% for GSH at day 4 relative to day 0 in the presence and absence of Cl^-, respectively (Figure 39). Therefore, while it appears that some functional groups on o-SWCNTs are reduced by antioxidants (*i.e.*, decline in the D/G ratio), neither AA nor GSH reduced the carboxyl groups, which are necessary for enzyme-catalyzed degradation of nanotubes.[3] Thus, other mechanisms may be responsible for the mitigation of o-SWCNT biodegradation.

2.2.3.7 Potential mechanism – effects of antioxidants on the peroxidase cycle and HOCl

Kagan *et al.* demonstrated that in the absence of transition metal catalysts, H_2O_2 fails to oxidize AA.[190] Moreover, our electron paramagnetic resonance (EPR) spectroscopy data for a system consisting of o-SWCNTs, MPO, H_2O_2, and AA demonstrated the formation of the ascorbate radical, which implies that AA is being oxidized by reactive intermediates (Figure 35). This notion is also substantiated by the redox potential of the AA (E^0 = 0.066 V);[191] therefore, AA has the potential to reduce Compounds I and II of MPO given that the mean redox potentials of peroxidase cycle is 1.16 V (Figure 20b).[3] Consequently, AA can mitigate the biodegradation of o-SWCNTs by out-competing the nanomaterial as a substrate for MPO. GSH, on the other hand, is a relatively poor substrate for Compounds I and II of MPO;[192] in addition, its one-electron oxidation product, the glutathione thiyl radical, is a strong oxidant (E^0 = 0.920 V).[193] However,

GSH was also effective in preventing o-SWCNT oxidation by MPO both in the presence and absence of Cl^- thereby suggesting that glutathione thiyl radical likely reacted with excess GSH in solution to form GSSG and had not significantly contributed to the degradation of o-SWCNTs. Also, H_2O_2, can directly oxidize GSH;[194] hence decreases the quantity of H_2O_2 available to interact with MPO and generate reactive intermediates..

The protection afforded by the antioxidants during the production of HOCl is two-fold. First, as described above, the antioxidants can reduce Compound I (AA) or H_2O_2 (GSH) thereby reducing Compound I that is available to react with Cl^-. Second, HOCl oxidizes both AA and GSH at very rapid rates, which in turn affords protection for the o-SWCNTs (Figure 20b). The mechanism of AA oxidation by HOCl may entail either an electrophilic chlorination or a two-electron-transfer reaction whereby DHA is produced.[195] Meanwhile, GSH oxidation by HOCl results in the formation of a sulfenyl chloride (GSCl), which reacts with either GSH to produce glutathione disulfide (GSSG) or with two equivalents of HOCl thereby yielding glutathione sulfonyl chloride (GSO_2Cl).[196] GSO_2Cl is likely hydrolyzed to glutathione sulfonic acid (GSO_2OH).[196] Our ESI-MS data confirmed that both GSO_2OH and GSSG were formed.

2.2.4 Conclusions

The cumulative results from TEM and Raman and UV-vis absorption spectroscopies demonstrated that both hypochlorite and reactive intermediates oxidized o-SWCNTs thereby resulting in the degradation of this nanomaterial. Additionally, the data also established that the water-soluble antioxidants, L-ascorbic acid and L-glutathione, could suppress MPO-driven biodegradation of CNTs. Significantly, antioxidant supplementation may attenuate oxidative

stress-associated tissue damage incurred by CNT exposure; for example, vitamin E deficiency enhances the pulmonary inflammatory response and oxidative stress induced by SWCNTs in C57BL/6 mice.[197] The initial phase of the inflammatory response includes massive recruitment and activation of neutrophils (PMNs), whose MPO is involved in biodegradation of CNTs. Therefore, the choice of protective antioxidants for regulating CNT-induced oxidative stress should be selective and include testing for neutrality towards CNT biodegradation.

2.2.5 Experimental

2.2.5.1 Materials

Oxidized arc discharge single-walled carbon nanotubes (o-SWCNTs) were acquired from Carbon Solutions, Inc. (P3, Riverside, CA, USA). Lyophilized purified native human myeloperoxidase (MPO) was purchased from Athens Research and Technology, Inc. (Athens, GA, USA). L-ascorbic acid (AA), L-glutathione (reduced, GSH), L-glutathione (oxidized, GSSG), hydrogen peroxide (30%, H_2O_2), 0.1 M phosphate buffer, sodium chloride (NaCl), and diethylenetriaminepentaacetic acid (DTPA) were obtained from Sigma Aldrich (St. Louis, MO, USA). Amplex Red was procured from Molecular Probes (Life Technologies, Grand Island, NY, USA). TefSep PTFE membrane filters (GE Infrastructure Water & Process Technologies) that were 25 mm diameter and contained a pore size of 0.22 µM were acquired from Spectrum Chemicals and Laboratory Products (New Brunswick, NJ). Finally, sodium hydroxide (NaOH), hydrochloric acid (HCl), polystyrene 96 well plates and Amicon Ultra 4 (10K MWCO, Millipore) were obtained from Fisher Scientific (Pittsburgh, PA, USA).

2.2.5.2 Methods

DTPA was added to the 0.1 M phosphate buffer at a final concentration of 300 µM. Next, a dispersion containing 1.0 mg/mL of P3 o-SWCNTs was prepared by sonicating 1.0 mL of 0.1 M/300 µM phosphate/DTPA buffer with 1.0 mg of P3 o-SWCNTs for 1h. Stock solutions were prepared for AA (250 mM), GSH (250 mM), H_2O_2 (18.75 mM), and NaCl (5 M) utilizing the nanopure water as the solvent. Since the buffer in which the MPO was lyophilized contains NaCl, different MPO preparations were employed for $\pm Cl^-$ conditions. For $+Cl^-$ samples, the as received lyophilized MPO (*i.e.*, AR MPO) was reconstituted with 350 µL of nanopure water for a final concentration of 2.0 µM. On the other hand, for $-Cl^-$ conditions, the lyophilized MPO was reconstituted with 350 µL of nanopure water, and the buffer was exchanged to 0.1 M phosphate buffer utilizing an Amicon Ultra 4 to a final volume of 350 µL (forming BE MPO). The activity of BE MPO was compared to AR MPO utilizing Amplex red (refer to MPO Activity Study, Table 6 and Figure 37), and the quantity of BE MPO utilized in the experiment was proportionally adjusted to obtain equivalent rates. Table 7 replicates the initial experimental conditions, which were performed in triplicate using 96 well plates. Employing an Epoch microplate spectrophotometer (BioTek, Winooski, VT), an initial (Day 0) absorbance was measured at 999 nm. Every hour, 18.75 mM H_2O_2 and 250 mM of both AA and GSH were apportioned at concentrations of 75 µM, 1 mM, and 1 mM, respectively, for a total of 7 additions on day 0 and 8 additions on days 1, 2 and 3. In addition, 4 µL of AR MPO and 4.8 µL of BE MPO were added to the samples (according to Table 7, MPO columns) on days 1, 2 and 3. Between additions, the samples were incubated at 37 °C in an incubator (Thermo Scientific).

On day 4 (96 h), the Epoch microplate spectrophotometer was again utilized to measure the absorbance at 999 nm, and the samples from day 4 were characterized utilizing transmission

electron microscopy (TEM), Raman spectroscopy, and visible-near infrared (vis-NIR) absorbance spectroscopy.

2.2.5.3 Transmission Electron Microscopy

Samples were diluted 1:100 with nanopure water. 5 µL of the suspended sample was placed on a lacey carbon grid (Pacific-Grid Tech) and permitted to dry in ambient conditions for overnight prior to TEM imaging (FEI Morgagni, 80 keV).

2.2.5.4 Raman Spectroscopy

Samples were prepared by drop-casting approximately 100 µL of sample on a quartz microscope slide and drying. All spectra were collected on a Renishaw *inVia* Raman microscope using an excitation wavelength of 633 nm. Samples were scanned from 100 – 3100 cm^{-1} to visualize the RBM, D, G, and 2D bands. Spectra were collected with a 15 second exposure time and averaged across 5 scans per location; a total of 5 locations were selected per sample.

2.2.5.5 vis-NIR Absorbance Spectroscopy

Samples (150 µL) were analyzed using a Lambda 900 spectrophotometer (Perkin Elmer) and 200 µL quartz cuvettes (Path length: 1 cm, World Precision Instruments, Inc.). The samples were scanned from 500 – 1250 nm. All samples were utilized without any further treatment or purification. Peak integration was conducted relative to the baseline employing Origin.

2.2.5.6 Electron Paramagnetic Resonance Spectroscopy

Ascorbate radicals were detected using a JEOL-RE1X EPR spectrometer (Tokyo, Japan) in 50 mM phosphate buffer, containing 100 µM DTPA at 25 °C. Samples (100 µL) contained 3 µL SWCNT (stock concentration 5 mg/ml), 1.5 µL MPO (stock concentration 2 µM), 100 µM H_2O_2, 140 mM NaCl, and 1.0 mM AA. Measurements were performed in gas-permeable Teflon tubing (0.8-mm internal diameter, 0.013-mm thickness) from Alpha Wire Corp. (Elizabeth, NJ). The tubing containing the sample was folded twice and placed into a 3.0-mm EPR quartz tube. The EPR conditions for detecting ascorbate radicals were: 335.0 G center field, 50 G sweep width, 0.79 G field modulation, 20 mW microwave power, 0.1 s time constant, 1000 receiver gain, 2 min time scan. Spectra were collected using EPRwase software (Scientific Software Services, Bloomington, IL).

2.2.5.7 Electrospray Ionization – Mass Spectrometry (ESI-MS)

Three samples, which consisted of reduced GSH (1 mg/mL), oxidized GSH (GSSG, 1 mg/mL), and o-SWCNT + MPO + H_2O_2 + Cl^- + GSH (100 µM, final) were analyzed by positive mode electrospray ionization – mass spectrometry (ESI-MS). Each sample was filtered through a 0.22-µm-syringe filter (Whatman, Sanford, ME, USA), and 1 µL of sample was directly injected into a LCMS-2020 unit (Shimadzu Scientific, Columbia, MD, USA). Data was acquired for 10 minutes.

2.2.5.8 Monitoring MPO Activity with Amplex Red

Amplex Red was employed to test MPO activity for both the as received and buffer exchanged MPO samples. A 10 mM stock solution of Amplex Red was prepared by dissolving the reagent

in DMSO. Table 6 provides the experimental details for the assay. After gentle mixing, a fluorescence-based kinetic experiment was implemented on the four samples whereby a Fluoromax 3 (Horiba Scientific, Edison, NJ, USA) was employed to acquire measurements every 5 s for a total of 120 s with the excitation wavelength at 575 nm and emission wavelength equal to 585 nm. The relative activities are compared in Figure 37.

2.3 INSIGHT INTO THE MECHANISM OF CARBON NANOTUBE DEGRADATION

2.3.1 Role of Reduction Potentials in Peroxidase-Catalyzed Oxidation/Degradation

Recently, the reduction potential of SWCNTs with different chiralities and diameters were modeled[198] and experimentally measured[199] *via* electrochemistry coupled with spectroscopy. In Figure 21, the electrochemical potentials of SWCNTs with different diameters are plotted against the reduction potentials of HRP (E^0, +0.884 V), MPO (E^0, +1.16 V), and the hypohalous acids, HOCl (E^0, +1.28 V) and HOBr (E^0, +1.13 V), which are the formed by the oxidation of Cl^- and Br^- by MPO and EPO, respectively, *via* the halogenation cycle.[3, 200] The electrochemical potentials of SWCNTs have been shown to increase as the tube diameter decreases (Figure 21**,** V1s line). Therefore, in this model, electrons are transferred from the top of the valence band (*i.e.,* for SWCNTs) to the oxidizing species. For the HRP/H_2O_2, the redox potential is ~0.88 V, which is higher than the V1s bands of the large diameter SWCNTs (pink region), but similar to the small diameter SWCNTs (green region). As a result of this difference in the redox potential,

large diameter SWCNTs are more favorably oxidized relative to smaller diameter SWCNTs, which is in agreement with the shortened degradation time that we observed for large SWCNTs.[130, 132] For either the MPO/H_2O_2/NaCl or EPO/H_2O_2/NaBr system, HOCl or HOBr is produced and demonstrated a redox potential of 1.28 V or 1.13, respectively.[4] As evidenced by the degradation of acid treated HiPco SWCNTs *via* the MPO/H_2O_2/NaCl system, these oxidants, which exhibit a greater oxidizing capacity than HRP, have the capacity to oxidize even small diameter SWCNTs, which have significant potential differences.[144] It has been demonstrated that hypochlorite results in the introduction of acid "defects" sites on the surface of CNTs.[176] Therefore, for MPO-catalyzed biodegradation, it is possible that the initial oxidation of CNTs is predominantly due to the effects of hypochlorite (as a result of its very high oxidizing potential); the accumulation of oxidative "defects" may pave the way for subsequent more effective oxidation *via* both mechanisms (*i.e.*, hypochlorite and peroxidase reactive intermediates with lower oxidizing potentials). Likewise, since HOBr is also a strong oxidant (E^0, +1.13 V), presumable the biodegradation pathway proceeds in a similar fashion.

While this model works well for pristine SWCNTs, this carbon-based nanomaterial is often p-doped by acid treatment,[201] which further increases their redox potential and theoretically lowers their reactivity compared to the pristine SWCNTs by drawing their valence band closer to the oxidation potential of reactive species. This may not be the case, however, as pristine SWCNTs were shown not to be degradable by enzymatic oxidation.[130, 132] Therefore, certain functionalities are required to undergo the peroxidase cycle. Carboxyl and hydroxyl (phenol) groups have labile hydrogen atoms that assist the peroxidase cycle, in which Compound I oxidizes a substrate by two sequential, one-electron oxidation steps to form water. In pristine

SWCNTs that have neither functional groups nor labile hydrogen atoms, the biodegradation of pristine SWCNTs cannot be initiated.

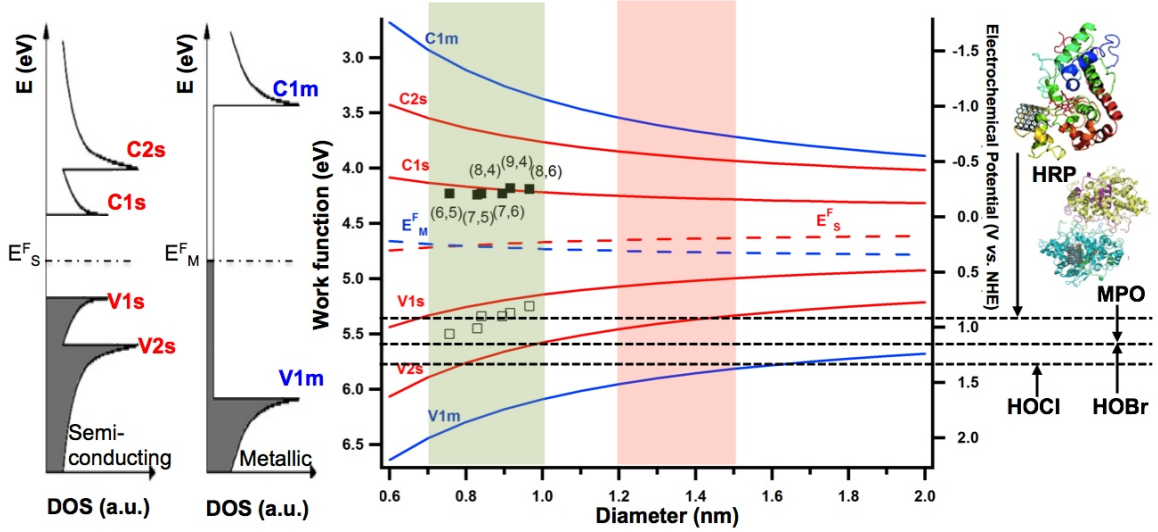

Figure 21. Electrochemical potentials of SWCNTs with different diameters plotted against the standard reduction potentials of HRP, MPO, HOBr, and HOCl (black dashed line). The dependence of electrochemical potentials of SWCNTs on their diameter were modeled in Ref. [202] with experimental data adapted from Ref. [199] (squares). The green region indicates the diameter range for HiPco SWCNTs, and the pink region specifies the larger diameter SWCNTs fabricated by electric arc discharge. Adapted with permission from [144]. Copyright 2013 American Chemical Society).

2.3.2 The Effect of Dispersity on Peroxidase-Catalyzed Oxidation/Degradation

One plausible explanation for the observation that covalently functionalized SWCNTs undergoes peroxidase driven degradation is related to the overall dispersity of CNTs in an aqueous media. Because pristine CNTs are intrinsically hydrophobic, there exists a strong tendency for nanotubes to aggregate into bundles, ropes, and networks as a result of van der Waals forces. To counteract these effects, CNTs have been modified by numerous covalent and noncovalent

modifications (Section 1.2.4) to render this nanomaterial more dispersible in an aqueous environment.[168] To this end, CNTs have been functionalized employing several methodologies, including: (1) the creation of defect-sites *via* strong oxidant chemistry, (2) covalent chemistry performed on sidewall, (3) attachment of pyrene derivatives *via* π-π interactions, and (4) noncovalent wrapping utilizing surfactants/amphiphiles, polymers, and biopolymers.[33] These techniques often yield a high-quality dispersion, which is composed mainly of individualized nanotubes with the remainder consisting of small bundles; Coleman and coworkers demonstrated that the quality of these dispersions scale with the ζ-potential of the dispersion.[203] As the ζ-potential increases, the electrostatic repulsion of the functional groups imparted by the dispersing agent/*via* covalent modification is sufficient to overcome the attractive van der Waals interactions of the CNTs.[204] While insight relating the direct role between bundling and degradation has not yet been reported in the literature, all studies that reported degradation were conducted on covalently functionalized CNTs that demonstrate minimal bundling. Since it has been demonstrated that hypochlorite results in the introduction of acid "defects" sites on the surface of CNTs,[176] we hypothesize that the hypochlorite and reactive intermediates produced by the halide and peroxidase cycles, respectively, will degrade pristine nanotubes that are individualized. To this end, studies are underway to assess if pristine SWCNTs that are well dispersed *via* noncovalent functionalization (*e.g.* polymers, surfactants, and phospholipids) and subjected to MPO-catalyzed degradation will degrade.

2.3.3 The Role of Functional Groups in Peroxidase-Catalyzed Oxidation/Degradation

Kane and coworkers correlated CNT oxidation to the disruption of the graphitic lattice incurred by functionalization.[205] Strong oxidizing acids employed to functionalize SWCNTs typically yield epoxide, peroxide, hydroxyl, carbonyl, and carboxylate functional groups.[205] During carboxylation, three bonds belonging to the participating carbon atoms are broken, rendering this functionality attached to the graphitic backbone by only one bond (Figure 22). Thus, carboxylated CNTs appeared most susceptible to enzymatic oxidation, because only one bond needed to be cleaved.

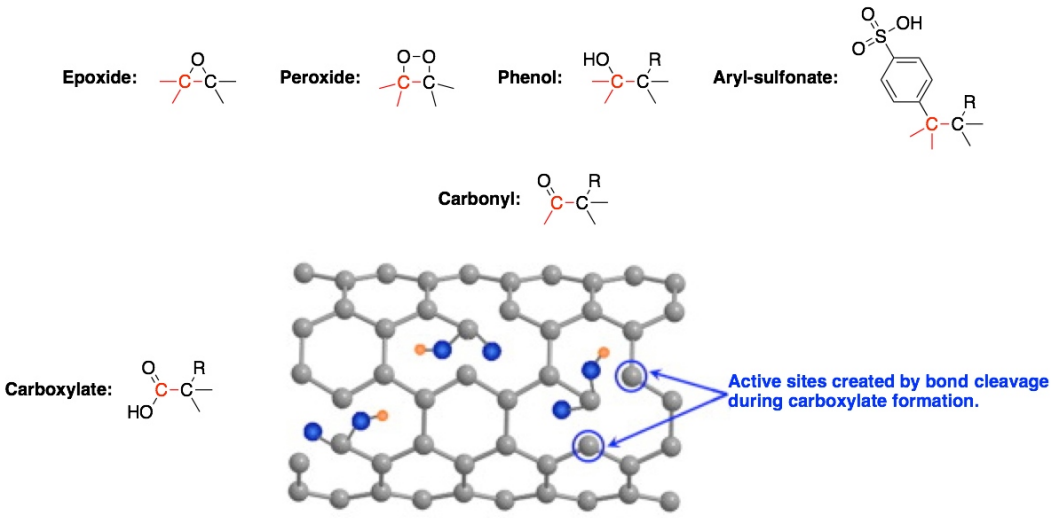

Figure 22. Schematic depicting the relationship between functionalization and CNT oxidation. While all functional groups disrupt the π-conjugation of the CNT, carboxylation uniquely damages the CNT backbone by creating two active sites, which provides points for further oxidative degradation. (Reproduced with permission from [3]. Copyright 2012 American Chemical Society).

2.3.4 Enzyme-Substrate Interactions in Peroxidase-catalyzed Oxidation/Degradation

We hypothesized that the carboxylates are important for an additional reason: their negative charge in aqueous media facilitates the proper orientation/proximity of the peroxidase enzyme's heme active site to the SWCNT substrate. Our collaborators employed molecular modeling studies to characterize the role of functional groups in enzyme-substrate interactions. A calculation of the docking conformations for carboxylated SWCNTs on HRP predicted that the carboxylated ends, which are negatively charged in an aqueous suspension, would orient themselves toward a positively charged arginine residue, Arg178, near HRP's heme site (Figure 14b).[130] In contrast, pristine SWCNTs, which failed undergo degradation, were predicted to orient themselves with the distal end of the enzyme, away from the active heme site.

For MPO, amino acid residues, Glu242, Asp94 and Met243, are covalently bound to the ferriprotoporphyrin IX heme group,[140] and molecular simulations suggested the existence of two potential interaction sites for CNT binding depending on their functionality.[134] For acid treated SWCNTs, the positively charged arginine residues (*i.e.*, Arg 294, 307, and 507), which reside near the proximal end of the heme group, strongly interacted with the negatively charged carboxylated nanotubes; this area also contained the catalytically active tyrosine residues, Tyr293 and 313 (Figure 14c).[134] Alternatively, pristine SWCNTs appeared to favor a second binding site, which exists at the distal end of the heme group away from the tyrosine residues.[134]

Two binding sites were identified for EPO both of which are stabilized by the electrostatic interactions between the positively charged arginine residues (*i.e.*, Arg205, Arg207, and Arg209 for binding site 1 and Arg94 and Arg99 for binding site 2) and the negatively charged oxygen-containing functionalities on oxidized SWCNTs site (Figure 14d).[137] Of these

two sites, binding site 1 was identified to be located on the same side as the catalytic site, appeared to be closer to the entrance of the catalytic site *versus* binding site 2, and overlapped with one of the bromide ion binding sites. Consequently, these cumulative results indicate that binding site 1 of EPO was the preferred location for biodegradation of oxidized SWCNTs.[137]

2.4 CONCLUSIONS

In this chapter, it was demonstrated that HRP, MPO, and EPO degraded CNTs in the test tube, which marks an important milestone in understanding the long-run chemical transformation and fate of this nanomaterial and has implications for both human health and the environment. Moreover, our current understanding of the factors that influence peroxidase driven degradation of CNTs was described. Details regarding *in vitro* and *in vivo* biodegradation studies and their possible role in future nanomedical applications employing CNTs as the delivery vehicle will be discussed in Section 4.2.

3.0 PEROXIDASE CATALYZED OXIDATION OF GRAPHENE DERIVATIVES

3.1 CHAPTER PREFACE

In this third chapter, the effect of peroxidase-catalyzed oxidation on two-dimensional (2D) carbon nanostructures is explored utilizing graphene oxide (GO, Section 1.3.3) and its reduced form, reduced graphene oxide (rGO, Section 1.3.3). The studies conducted on these carbon nanomaterials employed HRP.[133] The material contained within Section 3.2 was published as an original research paper in the journal, *ACS Nano*, and the figures have been reproduced with permission from [133].

List of Authors: G. P. Kotchey, B. L. Allen, H. Vedala, N. Yanamala, A. A. Kapralov, Y. Y. Tyurina, J. Klein-Seetharaman, V. E. Kagan, and A. Star.

Author Contributions: GPK, BLA, VEK, and AS conceived and designed the experiments, analyzed the data, and wrote the manuscript. GPK fabricated the GO, RGO, and hRGO, performed the experiment, and utilized absorption, Raman, and FTIR spectroscopies and mass spectrometry. BLA performed TEM and AFM. AAK ran sodium dodecyl sulfate polyacrylamide gel electrophoresis (SDS-PAGE). YYT performed EPR. N.Y. and J.K.S. performed the molecular modeling studies. HV conducted FET measurements.

3.2 HORSERADISH PEROXIDASE (HRP) AND GRAPHENE DERIVATIVES – THE ENZYMATIC OXIDATION OF GRAPHENE OXIDE

3.2.1 Introduction

Graphene has captured the attention of the scientific community due to its novel electronic properties[206, 207] coupled with its mechanical strength,[207, 208] both of which may make graphene integral in future generations of electronics, batteries, sensors, and composites.[55, 206, 207, 209, 210] One of the current methods of synthesizing graphene entails exfoliating graphite through oxidation to yield graphite oxide (GO), and this material is sonicated to produce graphene oxide.[79, 211] Graphene oxide is subsequently reduced either chemically[63, 79, 82, 211] or thermally[65, 66, 211] to produce reduced graphene oxide (RGO).

While the graphene precursor, GO, has been studied for about 170 years,[212] graphene oxide has only recently been recognized as an attractive material.[12-14] For example, graphene oxide has been proposed for drug delivery and cellular imaging applications.[213] Further, graphene oxide paper formed from interlocking sheets of graphene oxide demonstrated superior strength and stiffness compared to many other papers.[214] Finally, graphene oxide has been suggested as a simple alternative to poly(3,4-ethylenedioxythiophene)-poly(styrenesulfonate) (PEDOT:PSS), a hole transporting layer and electron blocking layer in organic photovoltaics (OPVs).[215] Given the recent rise in applications for graphene oxide and RGO, it is important to study the chemical properties of these carbon nanomaterials and to develop methods for their remediation to minimize their environmental impact.

Graphene and graphene derivatives such as graphene oxide have been modified for applications through treatment with strong oxidizing and reducing agents,[80] oxidative etching at temperatures greater than 400ºC,[216] etching using lithography,[217] and sonochemical approaches.[218] Here, we report an entirely new phenomenon; a mild enzymatic reaction that resulted in the oxidation and the formation of holey graphene oxide nanostructures, as demonstrated using numerous analytical techniques. Computational studies that complemented these results suggested that the molecular mechanisms for oxidation were related to the orientation, dynamics, and strength of binding of the enzyme to different graphene sheets. In addition to reporting on the stability of graphene oxide and RGO towards oxidation by peroxidases, we also demonstrated that enzymatic treatment of graphene resulted in alterations of their electronic properties. In particular, we found that holey reduced graphene oxide (hRGO), the reduced form of holey graphene oxide, demonstrated p-type semiconducting behavior, which could make this material desirable for applications involving field-effect transistors (FETs).

3.2.2 Results and Discussion

3.2.2.1 Enzymatic Reaction Conditions and Spectroscopic Analysis

Similar to our previous work where single-walled carbon nanotubes (SWCNTs) were degraded *via* enzymatic catalysis,[129, 130, 134] both graphene oxide and RGO samples were incubated with horseradish peroxidase (HRP) at pH 7.0, room temperature, and low concentrations (~40 μM final concentration) of hydrogen peroxide (H_2O_2) that were added daily (Figure 23a). These dispersions, which consisted of either graphene oxide or RGO with HRP, were classified as colloids based on the Tyndall scattering effect (Figure 23b).[80] In addition, Raman spectroscopy

was used to analyze graphene oxide and RGO on days 0, 4, and 20 of incubation with HRP/H_2O_2 (Figure 23c-d), and the ratio of the D band, which measured the presence of disorder in sp^2-hybridized carbon systems, to G band that evaluated stretching of C-C bonds in graphitic materials were compared.[89] For graphene oxide between days 0 and 4, the D:G ratio increased from 1.1 to 1.6, and by day 20, both the D and G bands disappeared. For RGO, the D:G ratio between day 0 and 4 decreased from 1.2 to 1.1, and increased to 1.3 by day 20. There were two plausible explanations for the increase in the D:G ratio from 1.1 to 1.6 between days 0 to 4 of graphene oxide incubation. First, because Raman spectroscopy was performed on different flakes, the variance in the D:G ratio may have been the result of different degrees of graphene oxide oxidation due to the modified Hummers' method. The second source may have been an increase in defect sites as a result of HRP catalyzed oxidation of the graphitic lattice. The D and G bands disappeared by day 20 as a result of the complete enzymatic oxidation of the graphitic lattice; Raman spectroscopy provided evidence that graphene oxide underwent oxidation. Like the Raman data in Figure 23d, it has been noted that the D:G ratio increases after graphene oxide is reduced to RGO using hydrazine.[63] The fluctuations observed in the D:G ratio for RGO between days 0, 4, and 20 were attributed to variations in samples since different flakes were examined.

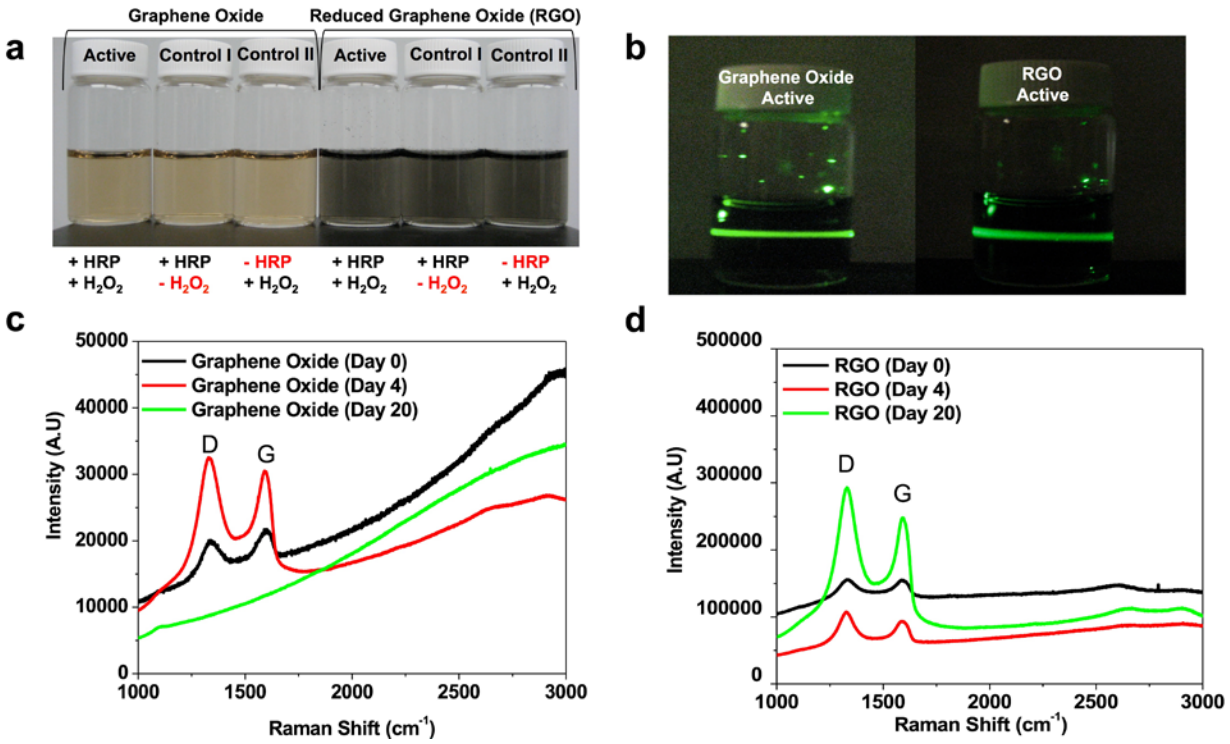

Figure 23. (a) Sample vials for the graphene oxide and reduced graphene oxide (RGO) enzymatic oxidation experiment. (b) The Tyndall scattering effect confirmed that the dispersions consisting of either graphene oxide or RGO with HRP (at day 0 of the oxidation process) were colloids. Raman spectra depicting (c) graphene oxide and (d) RGO after days 0 (black), 4 (red), and 20 (green) of incubation with horseradish peroxidase (HRP)/H_2O_2. The D and G bands are marked on the spectrum. (Reproduced with permission from [133]. Copyright 2011 American Chemical Society).

3.2.2.2 Microscopy

Transmission electron microscopy (TEM) was utilized to monitor the progression of HRP catalyzed oxidation of graphene oxide over a 20 day period with daily additions of 40 µM H_2O_2 (final concentration, Figure 24a). Initially at day 0, flat sheets with dimensions ranging from 0.5 to 1.5 µm were observed. After 5 days, graphene oxide sheets began to wrinkle; visible holes were formed in the graphitic lattice of the basal plane by day 8. The size of the holes increased

with time; at day 8 the average hole size was 2.1 ± 0.6 nm *versus* 26.7 ± 12.8 nm at day 10 of the oxidation process (Figure 25). By day 12 as the hole size continued to expand, small flakes of graphene oxide were observed, and the majority of graphene oxide was completely oxidized by day 20 of the experiment (Figure 24a). In contrast, no oxidation was observed by TEM for the graphene oxide controls, (–H_2O_2, Figure 40a) and (–HRP, Figure 40b). From the TEM micrographs obtained over the 20-day period of the study, it was concluded that graphene oxide underwent significant oxidation, which resulted in the formation of holes on its basal plane.

The TEM micrographs of graphene oxide at day 8 and 10 of the oxidation process were scrutinized to obtain information regarding the oxidation mechanism. In particular, two parameters were analyzed: the neck width (D) and the hole diameter (d) (Figure 25 insert). Interestingly, as the diameters of the holes increased on average 12 times (2.1 ± 0.6 nm to 26.7 ± 12.8 nm) from days 8 to 10, the neck width remained roughly unchanged (9.4 ± 7.8 nm *versus* 8.9 ± 6.9 nm for days 8 and 10, respectively). Therefore, as time progressed, HRP/H_2O_2 further oxidized the basal plane leading to the formation of additional holes; these holes merged together resulting in the formation of larger holes.

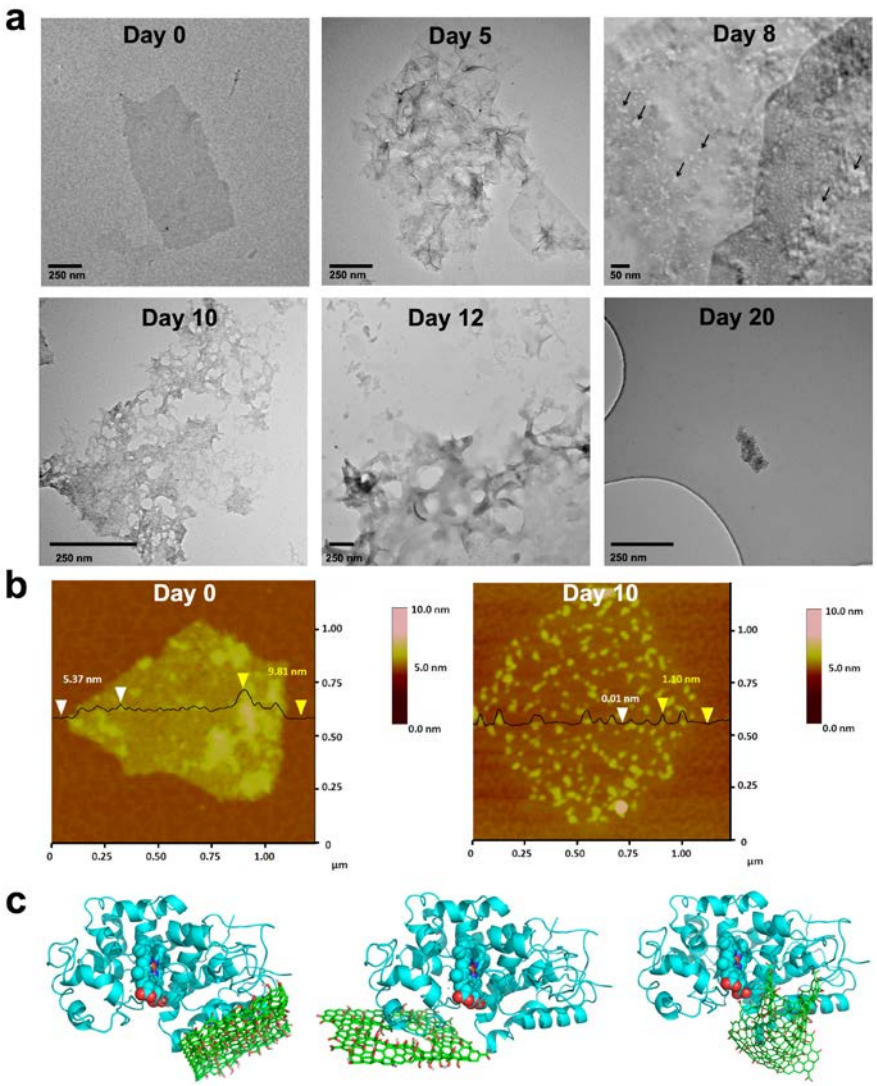

Figure 24. (a) Transmission electron microscopy (TEM) micrographs of graphene oxide after 0, 5, 8, 10, 12, and 20 days of incubation with horseradish peroxidase (HRP) and 40 µM hydrogen peroxide (H_2O_2). Arrows indicate hole formation in the basal plane at day 8. (b) Atomic force microscopy (AFM) images with section analysis of graphene oxide with HRP at day 0 (left) and holey graphene oxide (at day 10, right). Graphene oxide with HRP has a sheet height of 5.37 nm and 9.81 nm. Holey graphene oxide has a sheet height of 1.10 nm, and the holes were authentic at a height of 0.01 nm. (c) Binding poses of HRP on (from left to right) graphene oxide, holey graphene oxide, and a small sheet of graphene oxide calculated using molecular docking studies (AutoDock Vina). (Reproduced with permission from [133]. Copyright 2011 American Chemical Society).

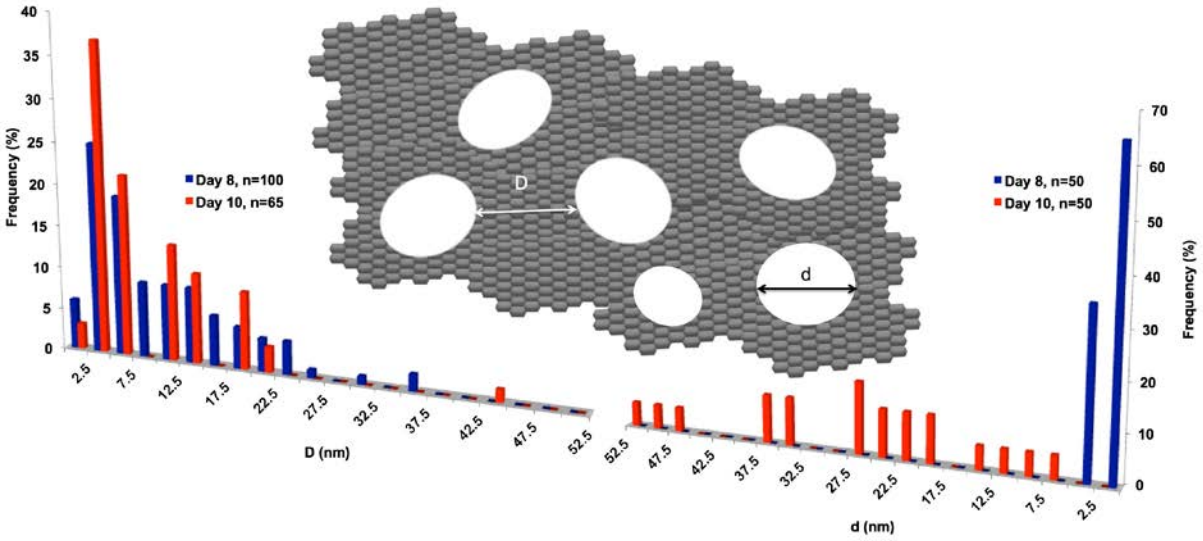

Figure 25. Histograms of neck width (D) and hole diameter (d) on days 8 and 10 of the oxidation process as measured from TEM micrographs. The cartoon insert illustrates the definitions of neck width and hole diameter. (Reproduced with permission from [133]. Copyright 2011 American Chemical Society).

As judged by TEM, RGO incubated under identical reaction conditions as graphene oxide, failed to undergo oxidation over the same twenty-day period (Figure 26a, S1c-d). A colorimetric assay performed with Amplex Red, a reagent commonly employed to measure trace H_2O_2 concentrations in biological systems,[219] had a peak for resorufin (the product of HRP catalyzed oxidation of Amplex Red) in the visible region around 570 nm for a sample containing RGO at both day 1 and day 20 of the oxidation process (Figure 41). This assay revealed that at least a portion of HRP retained enzymatic activity in the presence of RGO; the retention of HRP activity in the presence of RGO was also confirmed by electron paramagnetic resonance spectroscopy (EPR, Figure 42). Therefore, since there was no visible evidence of enzymatic oxidation for RGO over the twenty-day period of analysis, it appeared that HRP interacted with RGO and graphene oxide differently (*vide infra*).

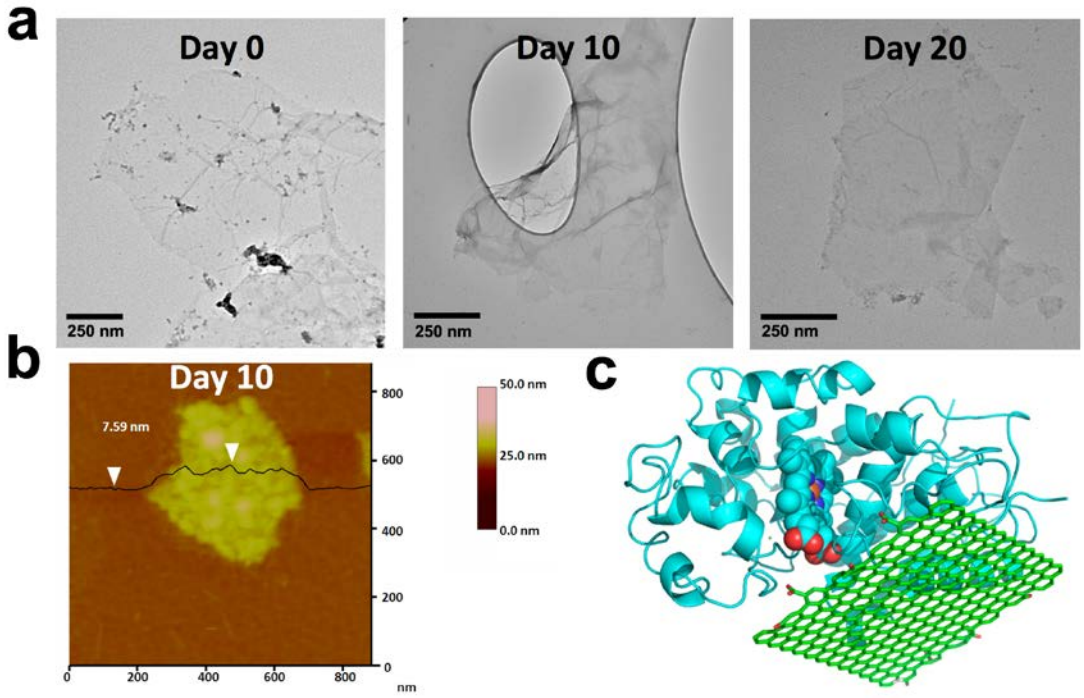

Figure 26. (a) Transmission electron microscopy (TEM) micrographs of reduced graphene oxide (RGO) after 0, 10, and 20 days of incubation with horseradish peroxidase (HRP) and 40 μM hydrogen peroxide (H_2O_2). (b) Atomic force microscopy (AFM) images with section analysis of RGO with HRP at day 10. RGO with HRP has a sheet height of 7.59 nm. (c) Binding poses of HRP on RGO calculated using molecular docking studies (AutoDock Vina). (Reproduced with permission from [133]. Copyright 2011 American Chemical Society).

Graphene oxide, holey graphene oxide, and RGO were further examined by atomic force microscopy (AFM, Figure 24b, Figure 26b, and S4). AFM section analysis indicated that graphene oxide had a height of 0.61 nm (Figure 43a); therefore, the exfoliation of graphite oxide by sonication successfully produced a single layer of graphene oxide. Since graphene sheets have a height of 0.34 nm, it was not possible for two sheets to be present (*i.e.*, 0.61 nm < 0.68 nm). The presence of covalently attached oxygen functional groups (tertiary alcohols and

epoxides) that decorate the basal plane of graphene oxide might be responsible for the added thickness of the graphene oxide flake. In addition, AFM confirmed that HRP binds to graphene oxide (Figure 24b). HRP's height was determined by AFM section analysis to be approximately 5 nm (Figure 43b);[130] therefore, the height of 5.37 nm obtained by section analysis in Figure 24b (graphene oxide – Day 0) indicated that a single layer enzyme was bound to an individual sheet of graphene oxide. Applying the same reasoning, one could conclude that two layers of enzyme existed on graphene oxide to produce a region where the height was 9.81 nm. The height of the holey graphene oxide sheet was 1.10 nm (a graphene oxide bilayer) with a hole height of 0.01 nm (Figure 24b, graphene oxide – Day 10). Finally, AFM section analysis indicated that RGO had a height 1.73 nm, which demonstrated that RGO consisted of an aggregation of flakes (Figure 43c). Since the oxygen functional groups on the basal plane were reduced, van der Waals forces dominated between the flakes of RGO resulting in the formation of aggregates. Similar to graphene oxide, AFM confirmed that HRP was bound to RGO during the incubation process; unlike graphene oxide, however, no evidence of oxidation was observed by AFM at day 10 (Figure 26b, RGO – Day 10). With a total height of 7.59 nm, one layer of enzyme was bound to a RGO aggregate that contained between four to seven sheets.

3.2.2.3 HRP interaction with Graphene Oxide/RGO

The ability of HRP to bind with sheets of graphene oxide/RGO was confirmed by sodium dodecyl sulfate polyacrylamide gel electrophoresis (SDS-PAGE), followed by silver staining, shown in Figure 5a. Due to its size, both graphene oxide and the highly hydrophobic RGO failed to migrate well during gel electrophoresis; therefore, the majority of the material was retained in the stacking region of the gel. The protein band at 44 kDa corresponded to the literature value

for HRP.[220] The quantity of protein that remained post-incubation with RGO was approximately three times less then the quantity of HRP present in other samples, which indicated that HRP was bound more tightly to RGO than graphene oxide. Additionally, the results of gel electrophoresis indicated that minimal auto-oxidation took place during both the tested incubation period and for 40 μM levels of H_2O_2. In the absence of exogenous oxidizable substrates, monomeric hemoproteins form dimers, trimers, and other oligomers during the activation of their peroxidase. This stems from the recombination of protein-derived (likely, tyrosyl) radicals generated as reaction intermediates[221-223] and results in the formation of covalent cross-links that are non-dissociable in SDS. Thus if HRP oligomers were formed in the reaction, they should have been detectable in the SDS gel. The lack of HRP oligomers indicated that H_2O_2-dependent cross-linking of the enzyme did not take place, and the oxidizing potential of the enzyme was directed towards graphene oxide/RGO oxidation.

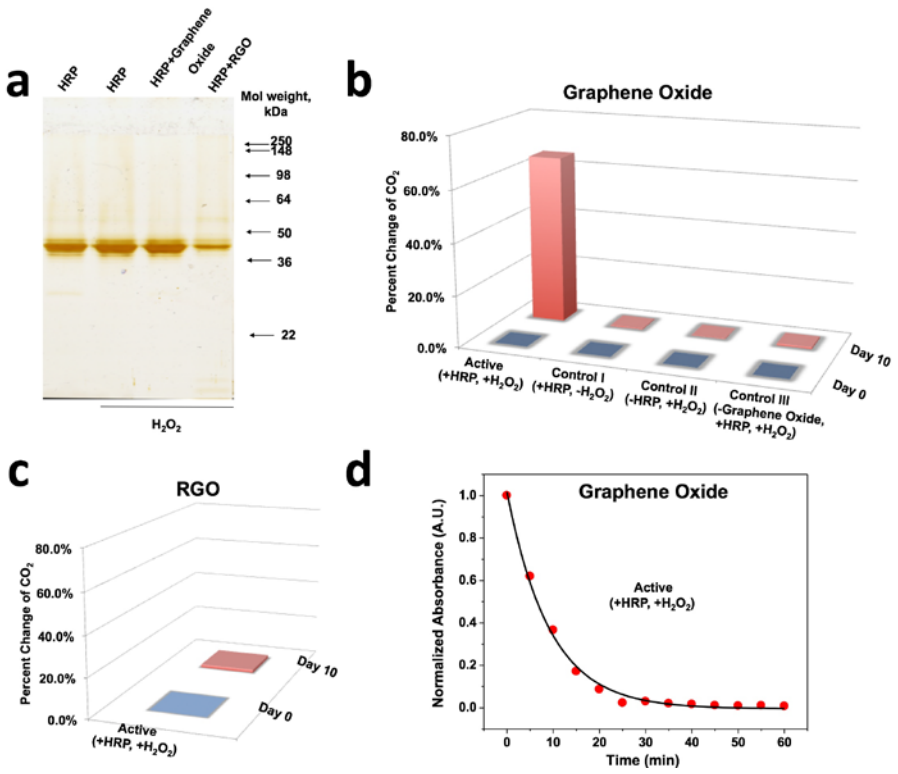

Figure 27. (a) Sodium dodecyl sulfate polyacrylamide gel electrophoresis (SDS-PAGE) with silver staining. The gel contained a control for horseradish peroxidase (HRP, around 44 kDa) without hydrogen peroxide (H_2O_2), HRP incubated for three hours in the presence of H_2O_2 (final concentration of 40 µM H_2O_2 added every 1h), and HRP incubated with graphene oxide or reduced graphene oxide (RGO) for three hours in the presence of H_2O_2 (final concentration of 40 µM H_2O_2 added every 1h). Relative increase in headspace CO_2 concentration as measured by GC-MS for day 0 and 10 for (b) G graphene oxide-active, control I (–H_2O_2), control II (–HRP), control III (–graphene oxide), and (c) RGO-active. It was determined that the CO_2 concentrations in the headspace of the sample vials increased by 65% for graphene oxide-active, <1% for graphene oxide-control I, graphene oxide-control II, and graphene oxide-control III, and 2% for RGO-active. (d) Examination of the enzymatic kinetics for the graphene oxide-active sample employing an Amplex Red assay, where the absorbance of resorufin, which was directly proportional to H_2O_2 concentration, was measured at 5-minute time intervals for 1 hour. The assay indicated that nearly all of the H_2O_2 was consumed over the first 30-minutes of analysis as graphene oxide was oxidized. (Reproduced with permission from [133]. Copyright 2011 American Chemical Society).

3.2.2.4 Molecular Modeling Studies

Employing AutoDock Vina software,[224] molecular docking studies were performed to identify the manner by which HRP was bound to graphene oxide and RGO. Docking of RGO to HRP indicated that there existed only one binding site on HRP where RGO can bind (Figure 26c, Table 9). The closest distance to the heme active site from RGO was 11.5 Å. The results for graphene oxide, on the other hand, indicated two different binding sites for graphene oxide on HRP. The first binding site was similar to the RGO binding site with participation of the additional residues Ala86, Glu88, Ser89, Pro92, and Lue299. The heme active site was predicted to be 12.8 Å away from the graphene oxide surface (Table 9). In comparison to the first binding site, the heme active site in the case of second binding site was predicted to be 8.7 Å away from the surface of graphene oxide (Figure 24c, Table 9). The overall predicted binding energy for the two binding sites on graphene oxide was –24.8 kcal mol^{-1} and –22.4 kcal mol^{-1}, respectively, and –26.7 kcal mol^{-1} for RGO, indicating that HRP may bind more tightly to RGO than to graphene oxide. This was consistent with the gel electrophoresis data, which indicated that two-thirds of the HRP was bound to RGO and retained in the well. When a hole was introduced into the graphene oxide sheet, we predicted only one binding site that consisted of HRP residues similar to that of the second binding site described for graphene oxide above (Figure 24c). This result suggested that graphene oxide could bind to HRP differently as compared to RGO making it susceptible for oxidation. These findings are in line with our previous observation of HRP binding to oxidized *versus* non-oxidized SWCNTs, where we also observed a preference of the enzyme's active site to be in closer proximity to the binding interface in oxidized material than in non-oxidized material. Finally, it was observed experimentally that holes formed preferentially on the basal plane, which indicated that the enzyme was more favorably bound to and oxidized

the planer portion of graphene oxide instead of the edge. As these holes on the basal plane increased in number, the necks collapsed, which resulted in an increase in the diameters of the holes on average 12 times from days 8 to 10; the neck width, however, remained roughly unchanged for days 8 and 10. This observation was consisted with the docking results that only identified favorable binding poses on the plane. Thus, it appeared that the edge failed to provide sufficient surface area for stabilization of the graphene-HRP interaction through hydrophobic contacts.

In summary, the molecular modeling studies suggest that the presence of epoxy- and hydroxyl groups in the basal plane and the flexibility of the oxidized graphene sheet may be responsible for the preferential enzymatic degradation of graphene oxide and holey graphene oxide *versus* RGO by HRP.

3.2.2.5 Molecular mechanisms of oxidation

No visible evidence of oxidation as determined by TEM was observed for RGO over the twenty-day period of analysis. Both the Amplex Red assay and the EPR data confirmed that the enzyme, HRP, remained active in the presence of RGO; therefore, another mechanism was responsible for the lack of visible oxidation. Based on our prior work with carboxylated SWCNT degradation[129, 130, 134] and the results obtained from the computational study, a potential mechanism of graphene oxide/RGO oxidation was elucidated. Since the binding energy was greater for RGO than graphene oxide, it was possible that the oxygen groups on graphene oxide allowed the enzyme to be more dynamic, which brought the heme site in close proximity of graphene oxide. Conversely, as a result of tighter binding between RGO and HRP, the dynamic motion of the enzyme was retarded. Therefore, the heme active site of HRP was not in close

proximity of the graphene lattice, which was necessary for oxidation to occur. Initially, HRP was inactive, where the heme peroxidase was in the ferric oxidation state. In the presence of hydrogen peroxide (H_2O_2), the heme active site underwent a protein-assisted conversion to a ferryl oxo iron (Fe^{4+}=O) porphyrin π cation radical known as Compound I.[143] Compound I was reduced back to the ferric state in two sequential, one-electron transfer steps. In the first step, the transient intermediate, Compound II, was produced; during this process, the porphyrin π cation radical was reduced while graphene oxide was oxidized. Graphene oxide underwent further oxidation when the ferryl oxo iron (Fe^{4+}=O) was subsequently reduced to the ferric state. During this process, the σ carbon-carbon bond of the tertiary hydroxyl and epoxide groups that were formed during the initial oxidization of graphite by $KMnO_4$ and H_2SO_4 were cleaved. This was consistent with the literature, where it was demonstrated that peroxidases have the ability to catalyze both epoxidation and cleavage of carbon-carbon bonds in the presence of H_2O_2.[225, 226]

3.2.2.6 Oxidation product analysis

While identification of the intermediate products of graphene oxide oxidation is ongoing, product analysis in the sample headspace utilizing gas chromatography – mass spectrometry (GC-MS) indicated that CO_2 was the final product of complete enzymatic catalyzed oxidation. Sample headspace of sealed vials in which HRP was incubated with either graphene oxide (Figure 27b) or RGO (Figure 27c) was extracted, and the concentration of CO_2 was determined. By day 10, the concentration of CO_2 increased by 65% for graphene oxide (Figure 27b) and 2% for RGO (Figure 27c) over ambient; whereas the controls for graphene oxide (–HRP, –H_2O_2, and –graphene oxide) indicated only a 2-4% increase in relative CO_2 levels at day 10 (Figure 27b). With over thirty times the amount of CO_2 produced for graphene oxide oxidation

compared to the RGO control, the Raman and TEM results, which indicated that graphene oxide underwent HRP catalyzed oxidation, appeared to be substantiated.

3.2.2.7 Enzymatic Kinetics

Amplex Red was utilized to monitor the concentration of the substrate, H_2O_2, as a function of time to yield enzyme kinetics. HRP incubated with graphene oxide and H_2O_2 demonstrated that 97% of the substrate, H_2O_2, was consumed within 30 minutes (Figure 27d). It should be emphasized here that in all above experiments H_2O_2 was added on a daily basis to facilitate thorough characterization of the oxidation products. Taking into account the enzymatic kinetic data, we conducted additional experiments, where H_2O_2 was added every 30 minutes. For the resulting data, holes were observed in the basal plane of graphene oxide after 4.5 hours (Figure 40e). These results proved difficult to reproduce, however, due to the quick rate of enzymatic oxidation once holes were formed, rendering most of the graphene oxide "over-oxidized" (Figure 40f). Attempts to shorten the total oxidation time by 15 minutes (*i.e.,* for a total oxidation time of 4.25 hours) yielded pristine graphene oxide sheets; therefore, there existed a narrow window, where hole formation occurred. Consequently, with respect to reproducibly generating holey graphene oxide, the multi-day approach appeared advantageous, and holey graphene oxide has been produced several times utilizing this technique.

3.2.2.8 Electronic properties of holey reduced graphene oxide (hRGO)

Creating holes in graphene is important to fine-tune its electronic properties. As a result of its zero bandgap, graphene is a semimetal.[227, 228] This property limits graphene's utility in some electronic applications such as room temperature field-effect transistors (FETs), which require

semiconducting materials. To overcome this limitation, theoretical work has predicted that quantum confinement and edge effects would produce semiconducting properties at room temperature in graphene sheets that have widths less than 10 nm; an active area of graphene research involves the fabrication of these quasi-one-dimensional structures referred to as graphene nanoribbons (GNRs).[229-231] Block copolymer lithography,[232, 233] laser induced photochemical reactions,[234] Joule heating,[235] oxidative etching at temperatures greater than 400ºC,[216] and two-dimensional polymer synthesis[236] have been employed to create nanometer sized holes on individual sheets of graphene. As a sheet of perforated graphene can be conceptualized as interconnected nanoribbons, the creation of holes in the basal plane of graphene opens its bandgap to yield a semiconducting nanomaterial.

To test if the side product of enzymatic oxidation has unique electronic properties, holey graphene oxide that was formed after 8 days of oxidation was reduced with hydrazine to yield hRGO flakes (Figure 40g), and this material demonstrated electrical conductivity. Both liquid-gated and back-gated FET measurements were implemented on RGO and hRGO (Figure 28a and Figure 44). For both of the measurement techniques, similar electronic transport characteristics were observed with the liquid gate measurement demonstrating more effective tuning of charge carriers.[237] RGO exhibited a V-shaped transfer characteristic (Figure 28a) similar to a single layer of graphene, which can be attributed to the zero band gap of graphene.[238-240] In comparison, hRGO exhibited a decrease in conductance with a p-type behavior and a positive shift in the Dirac points (Figure 28a). The comparison of transconductance ($\Delta I/\Delta V_g$) values for the n and p regions (Figure 28b) obtained from 12 different RGO and hRGO FET devices (6 devices each) confirmed the repeatability of the enhanced p-type semiconducting behavior of hRGO compared to RGO.

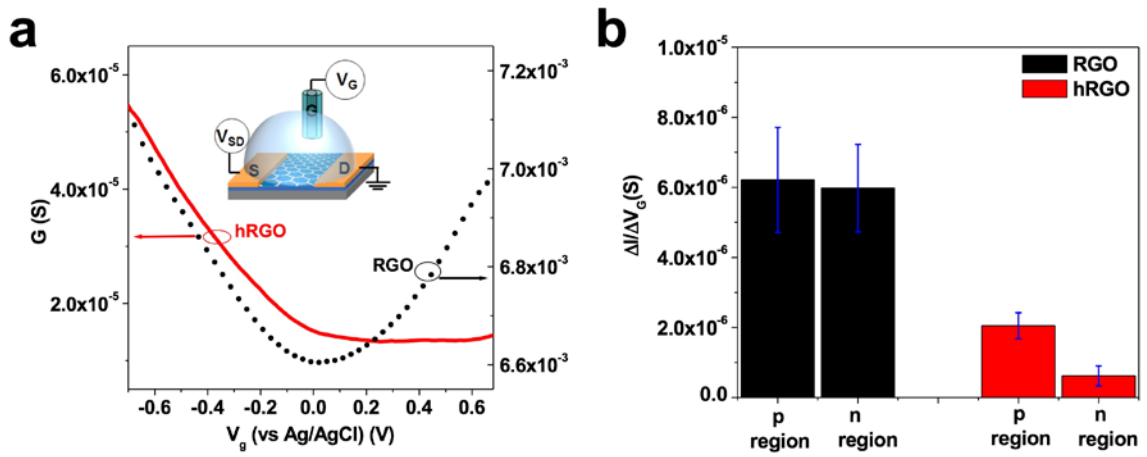

Figure 28. (a) Conductivity *versus* potential (liquid gate) plot for reduced graphene oxide (RGO, black circles) and holey reduced graphene oxide (hRGO, solid red line). The measurements were recorded in 10 mM KCl/10 mM PBS (pH 7) at a constant drain-source voltage of 10 mV. Inset represents a schematic of the experimental setup. (b) Comparison of transconductance ($\Delta I/\Delta V_g$) values of n and p region of 12 different RGO and hRGO FET devices (6 devices each). (Reproduced with permission from [133]. Copyright 2011 American Chemical Society).

The observed p-type behavior in hRGO samples can be attributed to the presence of holes in the basal plane of the graphene nanomaterial, which resulted in the opening of the band gap as a consequence of lateral quantum confinement[229-231] and the presence of additional oxygen-containing functional moieties (*i.e.*, carboxylic acids, lactols, quinines, hydroquinones, *etc.*) around the holes that were introduced during the enzymatic oxidation process. These data were in accordance with recent reports on nanoperforated graphene.[232, 233]

3.2.3 Conclusion

In this work, we demonstrated that HRP catalyzed the oxidation of graphene oxide that resulted in the formation of holes in the basal plane of this nanomaterial; over the same period of time, HRP failed to catalyze the oxidation of RGO. These observations were consistent with the computational findings, which indicated that the heme active site of HRP was in closer proximity, and the enzyme itself was more dynamic when bound to GO compared to RGO. This made graphene oxide more susceptible to carbon-carbon bond cleavage. With proposals for graphene oxide to be implemented in applications with an environmental impact,[241] the described enzymatic oxidation may be an attractive method for the bioremediation of graphene oxide. In addition to the environmental perspective, we discovered that enzymatic oxidation of graphene oxide produced holey graphene nanostructures, which upon reduction, demonstrated p-type semiconducting behavior. This material may have potential applications in electronics and sensor devices.

3.2.4 Methods

3.2.4.1 Materials

Graphite flakes, lyophilized HRP type VI, PBS, hydrazine hydrate (50 wt%), and 30% H_2O_2 were purchased from Sigma Aldrich. Amplex Red was purchased from Molecular Probes, Invitrogen, and the SilverSNAP stain kit was acquired from Thermo Scientific.

3.2.4.2 Preparation of Graphene Oxide and RGO

Graphite oxide was prepared utilizing a modified Hummers' method on graphite flakes that underwent a preoxidation step.[242] Graphene oxide (~0.125 wt%) was formed from graphite oxide that was diluted 1:4 with double distilled water and exfoliated for 30 minutes by ultrasonication followed by 30 minutes of centrifugation at 3400 r.p.m to remove unexfoliated graphite oxide. Atomic force microscopy (AFM), Fourier transform infrared spectroscopy (FT-IR), ultraviolet-visible spectroscopy (UV-vis), and transmission electron microscopy (TEM) were employed to characterize the exfoliated graphene oxide. Graphene oxide had a sheet height of 0.61 nm, which was determined by section analysis and confirmed that a single layer of graphene oxide was present (Figure 43a). Additionally, as evident by the FT-IR spectrum in Figure 45a, major peaks appeared around 3400 cm^{-1}, 1700 cm^{-1}, and 1000 cm^{-1}, which were attributed to O-H, C=O, and C-O stretching vibrations, respectively. Moreover, Figure 24a depicted a single sheet of graphene oxide as captured by TEM.

Graphene oxide was reduced to form RGO employing hydrazine hydrate, and RGO was dispersed in water with ammonium hydroxide at a pH around 10 following a published procedure.[80] A mixture containing 5.0 mL of 0.125 wt% graphene oxide, 4.8 mL of double distilled water, 200 µL of hydrazine hydrate (50 wt%), and 35 µL of NH_4OH (28 wt%) was stirred for 5 minutes and heated at 95 °C for 1 hour. The suspension containing RGO was subsequently dialyzed against distilled water to remove hydrazine and NH_4OH. RGO had a sheet height of 1.73 nm, which was determined by section analysis and confirmed that between three to five layers of RGO was present (Figure 43c). The FT-IR spectrum for RGO (Figure 45a) depicted a reduction in the O-H stretch around 3400 cm^{-1}, and carbonyl groups appeared

around 1700 cm^{-1}. Figure 26a and Figure 40c-d depicted the TEM micrograph of RGO, and the UV-vis spectrum of RGO displayed a shoulder around 327 nm (Figure 45b).

3.2.4.3 Incubation with HRP and H_2O_2

Three vials were prepared by adding 2.0 mL of the 0.125 w/v graphene oxide dispersed in double distilled water. Lyophilized HRP type VI was solubilized in 1× phosphate buffered saline (PBS) (11.9 mM phosphates, 137 mM NaCl, and 2.7 mM KCl) at 0.390 mg mL^{-1} and added to two of the vials containing graphene oxide at a volume of 4.0 mL. This created two vials with a total volume of 6.0 mL (active and control I, $–H_2O_2$) and one with a total volume of 2.0 mL (control II, –HRP). Next, 3.5 mL, 4.0 mL, and 7.5 mL of 1×PBS were added to active, control I, and control II, respectively, for a total volume of 9.5 mL, 10.0 mL and 9.5 mL. All vials were then sealed with a septum and wrapped with parafilm to create an airtight seal. The identical procedure was followed to prepare three vials for RGO. An additional control III vial (–graphene oxide) was created by adding 4.0 mL of HRP and 5.5 mL of 1×PBS. A sample of 0.5 mL of 800 µM H_2O_2 was added by needle through the septum to the active, control II, and control III vials; this started the oxidation reaction. Daily additions of 4 µL of 0.1 M H_2O_2 were added to the active, control II, and control III vials; this was continued on a daily basis for twenty days.

3.2.4.4 Preparation of Holey Reduced Graphene Oxide (hRGO)

A sample of holey graphene oxide subjected to 8 days of oxidation was reduced to form hRGO employing hydrazine hydrate in an aqueous suspension containing ammonium hydroxide at a pH around 10 following a published procedure (Figure 40g).[80] A mixture containing 5.0 mL of

0.125 wt% holey graphene oxide, 4.8 mL of double distilled water, 200 µL of hydrazine hydrate (50 wt%), and 35 µL of NH_4OH (28 wt%) was stirred for 5 minutes and heated at 95 °C for 1 hour. The suspension containing hRGO was subsequently dialyzed against distilled water with 0.5% NH_4OH to remove hydrazine. The FT-IR spectrum for RGO (Figure 45a) depicted a reduction in the O-H stretch around 3400 cm^{-1}, and carbonyl groups appeared around 1700 cm^{-1}. Moreover, the UV-vis spectrum demonstrated a well-defined peak around 327 nm (Figure 45b).

3.2.4.5 Raman Spectroscopy

Samples were prepared by drop-casting approximately 20 µL of graphene oxide or RGO at days 0, 4, or 20 on a quartz microscope slide and drying. All spectra were collected on a Renishaw *inVia* Raman microscope using an excitation wavelength of 633 nm. Samples were scanned from 1000 – 3000 cm^{-1} to visualize the D and G bands of the samples. Spectra were collected with a 15 second exposure time and averaged across 5 scans per location; a total of 10 locations were selected per sample.

3.2.4.6 Transmission Electron Microscopy

Samples in PBS suspension were first centrifuged at 3400 r.p.m. for 30 minutes and decanted of supernatant in order to effectively remove salt contributions from the buffer. Re-suspension into approximately 1 mL of double distilled H_2O was performed by sonication for one minute. One drop of the suspended sample was placed on a lacey carbon grid (Pacific-Grid Tech) and allowed to dry in ambient conditions for 2 hours prior to TEM imaging (FEI Morgagni, 80 keV or JEOL 2100F, 200 keV).

3.2.4.7 Atomic Force Microscopy (AFM)

A Multimode scanning probe microscope (Veeco) was utilized in tapping mode for height, phase, and sectional analysis. Sample preparation was performed on freshly cleaved mica that was treated with approximately 20 µL of 0.1% (w/w) poly–L–Lysine (aq) through spin-coating at 1,400 r.p.m. Approximately 10 µL of sample (aq) was spin-coated at 1,400 r.p.m. and allowed to dry in ambient for 45 minutes prior to imaging. Using a "supersharp" Si probe (tip radius <5nm, AppNano), tapping mode was performed at a drive frequency of 182.316 Hz, an amplitude set point of 0.2465 V, and a drive amplitude of 216 mV. Images were initially scanned in a 13.1 µm area prior to magnification of relevant areas. Post-imaging processing included section analysis for quantifying cross-sectional heights of samples.

3.2.4.8 Monitoring HRP Activity with Amplex Red.

Amplex Red (Molecular Probes, Invitrogen) was employed to test HRP activity. A 10 mM stock solution of Amplex Red was prepared by dissolving the reagent in DMSO. To a 250 µL aliquot of sample being tested for enzymatic activity, 234 µL of 1×PBS, 15 µL of 800 µM H_2O_2 and 1 µL of 10 mM Amplex Red were added. After gentle mixing, the UV-Vis spectrum of the sample was taken with 1×PBS used as the background.

3.2.4.9 UV-vis-NIR Spectroscopy

Aqueous samples (150 µL) were analyzed using a Lambda 900 spectrophotometer (Perkin Elmer) and 0.20 mL quartz cuvettes (Path length: 1 cm, World Precision Instruments, Inc.). The samples for the Amplex Red study were scanned from 300 to 800 nm. All samples were used without any further treatment or purification.

3.2.4.10 Electron Paramagnetic Resonance Spectroscopy.

To each sample containing HRP (0.35 µM) and etoposide (200 µM), H_2O_2 (80 µM) was added, and either a full ESR spectra (Figure 42a) or the time course of the EPR signal (Figure 42b-e) was recorded. The duration of the recordings were 10 min for sample A, and 1 min for the time course of the EPR signals (samples b-e). Sample d (Figure 42d) contained graphene oxide (5×10^{-5} mg/ml), and sample e (Figure 42e) contained RGO (5×10^{-5} mg/ml).

For the study, a JEOL-RE1X spectrometer at 25 °C outfitted with a gas-permeable Teflon tubing (0.8 mm i.d., 0.013 mm thickness) obtained from Alpha Wire Corp. (Elizabeth, NJ) was utilized. The tube (approximately 8 cm in length) was filled with 70 µL of the mixed sample, folded into quarters, and placed in an opened 3.0 mm i.d. EPR quartz tube. The etoposide phenoxyl radical spectra were recorded under following conditions: 3350 G, center field; 50 G, sweep width; 0.5 G, field modulation; 10 mW, microwave power; 0.03s, time constant; 2 min, timescane (sample a). The time course of etoposide radical EPR signals was obtained by repeated scanning of the field (1.0 G, sweep width; 3350 G, center field; 8 min, timescane) that corresponded to part of the EPR signal (samples b-e).

3.2.4.11 Polyacrylamide Gel Electrophoresis (PAGE)

Four samples were analyzed using gel electrophoresis, which included: a control for horseradish peroxidase (HRP) (around 44 kDa) without hydrogen peroxide (H_2O_2), HRP incubated for three hours in the presence of H_2O_2 (final concentration of 40 µM H_2O_2 added every 1h), and HRP incubated with graphene oxide or reduced graphene oxide (RGO) for three hours in the presence of H_2O_2 (final concentration of 40 µM H_2O_2 added every 1h). Samples were separated by sodium dodecyl sulfate (SDS) PAGE in Tris-glycine buffer. The running gel contained 10%

acrylamide, 0.375 mM tris-HCl buffer (pH 8.8), 0.1% SDS; the stacking gel contained 4% acrylamide, 0.125 mM tris-HCl buffer (pH 6.8), 0.1% SDS. Gels were polymerized by the addition of 0.1% ammonium persulfate and 0.1% TEMED. Running buffer included 250 mM tris, 250 mM glycine, 0.1% SDS. Samples were diluted in the loading buffer containing 0.125 mM tris-HCl (pH 6.8), 1% SDS and boiled for 5 min. Electrophoresis was run at a constant voltage of 130 v. Gels were stained by a SilverSNAP kit according to the manufacturer's manual.

3.2.4.12 Enzymatic Kinetic Studies

Amplex Red was employed to measure the concentration of the substrate, H_2O_2, as a function of time for a constant concentration of HRP (0.390 mg mL^{-1}) incubated with graphene oxide (graphene oxide-active). At 5 min time intervals (for 1 h), a 249 μL aliquot of sample and 1 μL of 10 mM Amplex Red was gently mixed, and the UV-Vis spectrum of the sample was taken with 1×PBS utilized as the background. Figure 5d contained the resulting concentration vs. time plots for graphene oxide-active; the data was fitted with an exponential decay plot.

3.2.4.13 Fourier Transform – Infrared Spectroscopy

Graphene oxide, RGO, and hRGO were isolated using TefSep Teflon laminated filters (0.22 μm hole size). Each sample was mixed with KBr and ground into a fine powder using a mortar and pestle. A KBr pellet was formed from the powder using a press, and the transmittance spectrum of the pellet was taken employing an Avatar 360 FT-IR.

3.2.4.14 Gas Chromatography – Mass Spectrometry (GC-MS)

Approximately 2 µL of sample headspace (total headspace volume: 5 mL) was injected into a Shimadzu QP5050A GC-MS unit with an XTI-F capillary column by sampling through the septum of one of the five vials (graphene oxide-active, graphene oxide-control I, graphene oxide-control II, graphene oxide-control III, and RGO-active) on day 0 and 10 of the oxidation study. A basic temperature program was performed, starting at 100 °C held for one minute, followed by temperature ramping at a rate of 10 °C/min until a maximum temperature of 325 °C was achieved and held for an additional 10 minutes.

3.2.4.15 Fabrication and Measurement of Solution- and Back-Gated RGO and hRGO Field-effect Transistors.

Field-effect transistors (FETs) were fabricated using standard photolithography process on Si/SiO_2 (oxide thickness = 200 nm). The Ti/Au metal contacts (Ti/Au = 30/100 nm) were deposited by electron beam evaporation. Individual graphene flakes were dielectrophretically deposited onto interdigitated electrodes at a frequency of 300 kHz and an a.c field of 1.6 MV/m,[243] and devices were annealed in vacuum at 180°C for 2 hours. The Si chips with graphene flakes were wire-bonded and packaged in a 40-pin ceramic dual-inline package. For backgate measurements, the Si substrate served as gate electrode. The electrical performance of the device was measured using two source measuring units (Keithley 2400). The gate potential was swept from -85 V to 85 V with a constant source drain voltage (V_{ds}) of 50 mV.

For electrolyte-gated measurements, a liquid gate potential was applied to Ag/AgCl (3M NaCl) reference electrode. Epoxy resin was used to prevent direct contact between metal electrode and electrolyte, leaving active graphene area exposed to electrolyte solution. A small

polymer chamber was placed on the chip and sealed with epoxy to hold a small volume (a few ml) of the electrolyte. Solution gate measurements were performed in 10 mM KCl/10 mM PBS (pH 7), and the gate voltage was swept from -0.75 V to 0.75 V with the V_{ds} kept constant at 10 mV.

3.2.4.16 Molecular Modeling

HRP was docked to different chemical structures of RGO and graphene oxide. 3D structures of RGO and graphene oxide sheets with dimensions of 3 nm were generated using SketchEI molecular editing tool provided by the VegaZZ software package.[244] Where indicated, edges of RGO were modified to contain both carboxyl- and carbonyl groups. In the case of graphene oxide, the basal plane always contained epoxide and hydroxyl groups, and the edges had a combination of carbonyl, carboxyl, lactol, and phenolic groups in accordance with previous work.[77, 245] Using AutoDock Vina software,[246] docking of HRP's X-ray crystal structure (PDB ID: 1H5A, chain A) to both RGO and graphene oxide sheets was performed as described previously.[130] A grid box with dimensions of 120 Å in the x, y, and z directions was used with the center of the box placed at the center of the protein molecule. The resulting 9 graphene ligand bound poses were further analyzed to find the most preferred binding pose in each case. The preferred binding pose was defined as the pose that has the minimum energy with the maximum number of poses clustered in that site.

3.3 CONCLUSIONS

Through the original research presented in this chapter, the effect of peroxidase enzymes on two dimensional carbon materials was elucidated. To this end, it was demonstrated that HRP catalyzed the oxidation of graphene oxide, which resulted in the formation of holes in the basal plane of this nanomaterial. Meanwhile, over the same period of time, HRP failed to drive the oxidation of reduced graphene oxide. The higher abundance of oxygen functionalities graphene oxide *versus* reduced graphene oxide may have been necessary to: (1) maintain well dispersed, individualized sheets; (2) properly orient the heme active site of HRP in close proximity to graphene oxide to thereby enable the further oxidation of this nanomaterial; and/or (3) provide an sp^3 defect site that is susceptible to enzymatic oxidation. Furthermore, the reduced holey graphene nanostructures, which can be conceptualized as interconnected graphene nanoribbons, demonstrated p-type semiconducting behavior. Therefore, this material has been employed as a transducer in sensor devices, which will be discussed further in Section 4.3.

4.0 OUTLOOK, APPLICATIONS, AND FUTURE DIRECTIONS

4.1 CHAPTER PREFACE

In this chapter, an outlook of the current field including *in vitro* and *in vivo* biodegradation experiments, which have benefits in terms of human health and environmental safety, and future directions that could has implications for nanomedical and sensor devices, will be explored. In particular, the current state of CNT biodegradation is addressed by summarizing recent *in vitro* and *in vivo* studies and potential future directions for the field in Section 4.2. Section 4.2 is largely reproduced with permission from [4]. Copyright 2013 Elsevier B.V. Meanwhile, the Star group's recent efforts to utilize holey reduced graphene oxide (hRGO) as a transducer in field-effect transistor (FET) devices for sensing applications is summarized in Section 4.3; portions of this section was reproduced with permission from [247]. Copyright 2011 American Chemical Society).

4.2 CNT DEGRADATION – *IN VITRO* AND *IN VIVO* STUDIES AND THEIR IMPLICATIONS FOR NANOMEDICINE

4.2.1 The *in vitro* Degradation of CNTs by Neutrophils

Kagan, coworkers, and collaborators demonstrated that activated neutrophils successfully biodegraded oxidized SWCNTs that were noncovalently functionalized with Immunoglobulin G (IgG).[134] To this end, the neutrophils were first activated employing the chemoattractant, *N*-formyl-methionyl-leucyl-phenylalanine (fMLP), and cytochalasin B, which promotes the degranulation of neutrophils including the release of hMPO. Neutrophil activation is characterized by the translocation of hMPO into phagosomes. The membrane-bound enzyme, NADPH oxidase, is also located within these vesicles and generates superoxide radicals, which further dismutate into H_2O_2 thereby facilitating the production of reactive intermediates and HOCl via the peroxidase and halogenation cycles of hMPO (Figure 14a). Meanwhile, the short, oxidized SWCNTs were functionalized with IgG to effectuate their efficient internalization into neutrophils. Raman microscopy confirmed that IgG-nanotubes were completely degraded by neutrophils during a period of 12 hours; on the other hand, only 30% of the non-IgG-treated nanotubes were degraded. Interestingly, the *in vitro* degradation of CNTs was found to be more profound in neutrophils than in macrophages, which contain much lower level of hMPO *versus* neutrophils. Therefore, the mechanism of CNT biodegradation by neutrophils stemmed from hMPO associated oxidative stress triggered by activated cells.

4.2.2 The *in vitro* Degradation of CNTs by Eosinophils

In a recent study, Fadeel, Kagan, and collaborators, demonstrated that stimulated primary murine eosinophils facilitated the biodegradation of oxidized SWCNTs.[137] During inflammation (*e.g.* conditions induced by CNT exposure), EPO, a peroxidase enzyme that is exocytosed by eosinophils, possess the ability to generate oxidative species (*i.e.,* reactive intermediates and HOBr, Section 1.6.4.2). Therefore, to simulate inflammatory conditions, the CNT degradation experiments were conducted in a cellular culture system comprising of highly purified murine eosinophils that were obtained from mouse bone marrow progenitors.[137] Degranulation and exocytosis of murine EPO (mEPO) were triggered by cytochalasin B and a platelet-activating factor (PAF). After incubating oxidized SWCNTs for 48 h with activated murine eosinophils, TEM images revealed that the bulk of SWCNT bundles were degraded leaving residual CNTs and carbonaceous materials, and the biodegradation of SWCNTs was also confirmed by a decrease in both the S_2 band and G-band for the NIR spectra and Raman spectra, respectively. Interestingly, in contrast to neutrophils, opsonization with immunoglobulins was not a prerequisite for biodegradation since the enzyme, EPO, is exocytosed upon cellular activation.

4.2.3 The *in vivo* Biodegradation of CNTs

Shvedova, Kagan, and collaborators investigated the *in vivo* degradation of oxidized SWCNTs instilled into the lung *via* pharyngeal aspiration of either wild-type (w/t) or myeloperoxidase knockout (MPO k/o) mice (*i.e.,* mice with MPO deficiency).[136] For both types of mice, a pulmonary inflammatory response and the accumulation of neutrophils was observed as early as

1 day after exposure. While the phagocytized SWCNTs remained persistent in the neutrophils of MPO k/o mice and induced a stronger fibrogenic response, SWCNTs underwent significant diminution in the lungs of w/t mice *versus* MPO k/o mice as evidenced through quantitative imaging (Figure 29a-b). Twenty-eight days after exposure, TEM and Raman analysis also confirmed that the oxidized SWCNTs underwent biodegradation as demonstrated by the shortening of the CNTs and an increase in the ratio of the D to G bands for the respective techniques; this effect, however, was more apparent in the w/t mice, which indicated the crucial role of MPO in oxidatively biodegrading SWCNTs *in vivo*. Since degradation was also observed in MPO k/o mice at a much lower rate (Figure 29c), other hemeperoxidases (*e.g.* EPO) may also contribute to the *in vivo* biodegradation process. In agreement with our previous *in vitro* study,[134] the *in vivo* results strengthened the importance of MPO containing neutrophils in the biodegradation of CNTs.

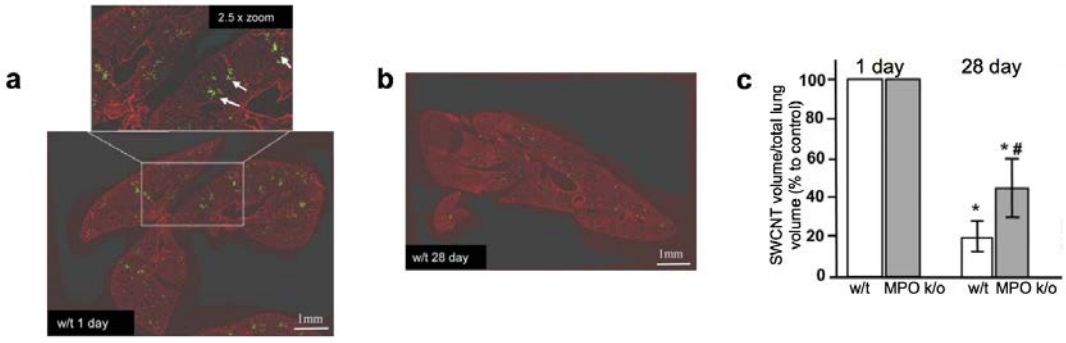

Figure 29. Quantitative imaging of the lung tissue sections from w/t mice treated with SWCNTs illustrated with green pseudo-color after (a) 1 day and (b) 28 days. The inset in (a) represents a higher magnification of a field with the presence of SWCNT (green punctuate spots pointed by white arrows). (c) Details the ratio of the volume of SWCNTs to the total lung volume for w/t and MPO k/o mice at 1 day and 28 days after injection, respectively. (Adapted with permission from [4]. Copyright 2013 Elsevier B.V.).

Nunes *et al*. recently investigated the fate of MWCNTs in mouse neuronal tissue.[248] Amine-functionalized MWCNTs were stereotactically injected into the motor cortex of a mouse brain, where microglia functioned as the primary professional phagocytes for the brain's immune system. TEM imaging was performed on parenchyma samples near the injection site 2 days post-injection. While widespread microglia internalization of MWCNTs was considered to be the predominant mechanism of early tissue response, the micrographs revealed that this nanomaterial was also internalized into different types of brain cells including neurons (Figure 30a). Aggregates of MWCNTs were localized in the possible phagolysosomal vesicles through active endocytosis or phagocytosis, and individualized MWCNTs were mainly internalized in the cytoplasm through a direct membrane translocation pathway. Besides the intact nanotubes, many internalized MWCNTs were observed to undergo severe structural deformation yielding amorphous debris (Figure 30b), which indicated the widespread initiation of the degradation process in microglia on day 2 after injection. This structural deformation was confirmed by Raman spectra that were taken of the injected brain tissue on days 2 and 14 after injection (Figure 30c-e), which demonstrated an overall reduction in the intensity of the D and G peaks coupled with an increase in background noise thereby indicating diminishing CNT content. A decrease in the D to G band ratio was observed, however, which might indicate the incomplete degradation of MWCNTs in microglia as was observed in another degradation experiment conducted on MWCNTs.[132] While the authors attributed the possible *in vivo* degradation of MWCNTs to the highly efficient phagocytosis capacity of microglia cells that possess both an oxidative lysosomal environment with low pH and an abundance of hydrolytic enzymes, the actual mechanism of degradation remained hypothetical.

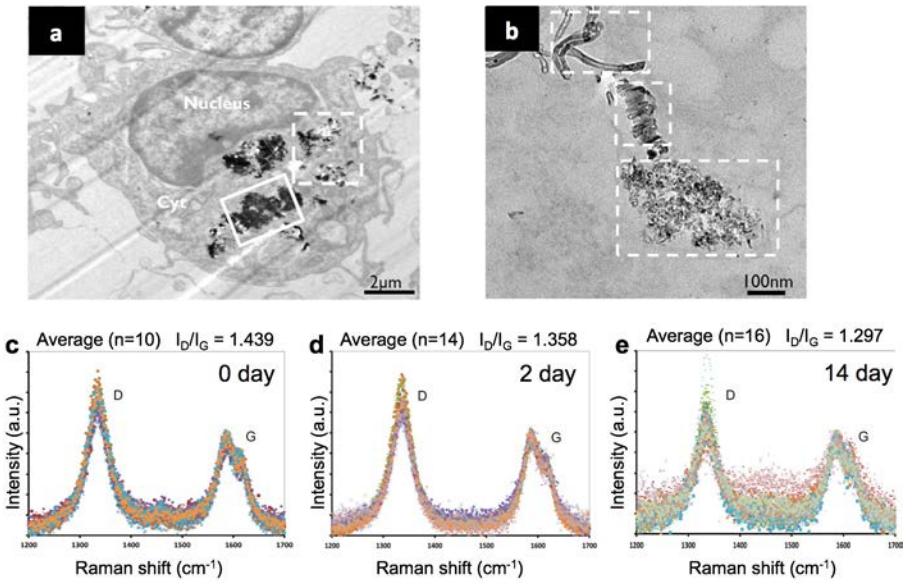

Figure 30. (a) Low resolution TEM image of microglia with amine-functionalized MWCNTs localized intracellularly, both intact individualized MWCNTs (dash box) and structurally deformed MWCNT debris (solid) is exhibited. (b) TEM image with higher resolution showing co-existing intact MWCNTs (top), carbon sheets unraveled form MWCNTs (middle) and deformed MWCNT debris. (c, d, e) Raman spectra taken from the starting MWCNTs before injection and brain sections 2 days and 14 days after MWCNT injection. The corresponding D to G band ratios (I_D/I_G) are recorded. (Reproduced with permission from [4]. Copyright 2013 Elsevier B.V.).

4.2.4 Outlook and Future Directions for Peroxidase-driven Biodegradation of CNTs – Implications for Nanomedicine

A variety of nanoparticles (NPs) that are composed of metals, metal oxides, quantum dots (QDs), polymers, and carbon (*e.g.* carbon nanotubes and graphene) are receiving increasing interest over the recent years due to their potential *in vivo* therapeutic or imaging applications.[249-251] As a result of their high surface area and unique optical and electronic properties, CNTs have the

potential of becoming a highly efficient delivery vehicle for drugs and biomolecules.[251] Because as-prepared CNTs are hydrophobic, to enhance their dispersibility in aqueous environments and thereby implement this carbon-based nanomaterial for biomedical applications,[168] CNTs must be modified by either covalent (Section 1.2.4.2) or noncovalent means (Section 1.2.4.1); this action will not only enhance biodispersibility but also biocompatibility of CNTs. Once rendered biodispersible and biocompatible, the high surface area of the CNTs presents an attractive platform for therapeutic delivery, where peptides, nucleic acids, proteins, and drugs could be (1) stored in the large inner-tubular volume; (2) π-π stacked to the walls; and/or (3) covalently conjugated to defect sites on the walls/edges of this carbon-based nanomaterial.[252] Moreover, CNTs are proficient at entering the nuclei of cells,[253] which may render this nanomaterial integral for gene therapy applications. Interestingly, the near-infrared (NIR) biological transparency window, which occurs in the range of 800 to 1400 nm, falls within the region where SWCNTs strongly absorb and emit light (*i.e.,* 800 to 1600 nm).[251] As a result, SWCNTs have been employed for photothermal therapy, photoacoustic imaging, and Raman detection/imaging.[251]

Ideally, CNT delivery vehicles that transport theranostic payloads should be disposed of after arriving at their target destination sites. To this end, while many chemical methodologies have been developed to "oxidatively cut" and degrade CNT, the aggressive nature of these oxidants precludes their possible employment in physiologically relevant environments (*i.e.*, tissues and body biofluids). Consequently, this prompted an active search for possible enzymatic mechanisms and pathways whereby mild and controlled oxidation reactions would effectively biodegrade CNTs. The discovery of peroxidase-driven biodegradation processes is an important milestone on the path to regulated and targeted spatiotemporal degradation of CNT. Through

either noncovalent functionalization or covalent attachment through stimuli-cleavable groups, specialized signaling molecules of lipid and/or protein nature will facilitate the internalization of CNTs. Also, one can envision the attachment of chemical/biological species that will activate the professional phagocytes. Acute and resolution phases of the body's inflammatory response are characterized by the predominant accumulation of myeloperoxidase (MPO)-rich PMNs and macrophages, respectively. One can envision that MPO-driven oxidative reaction will represent the dominant pathways for the CNTs biodegradation during the acute phase. In contrast, macrophages, which are relatively poor in MPO, may utilize a different oxidizing system such as peroxynitrite generators to be involved in the CNT biodegradation process. In this regard, NADPH-oxidase and NO synthases (*e.g.* iNOS) may be particularly important as sources of superoxide radicals and $NO^{\bullet}$, respectively. By producing these reactive oxygen and nitrogen species (*i.e.,* ROS and RNS), macrophages are involved in the production of peroxynitrite, whose high oxidizing potential is sufficient to trigger CNT oxidative degradation. Therefore, by tailoring functionalization, one can envision a possible tool for regulating the biodegradation of CNTs coated with important payloads. Alternatively, nano-containers with encapsulated freight can be utilized in ways where oxidative biodegradation of the vehicle will facilitate the release of the inner contents as they reach the desired targets. While different types of nano-containers have been designed and fabricated,[254-256] approaches towards the utilization of peroxidase-catalyzed oxidative biodegradation on these types of delivery nano-devices in target organs/cells have not yet been developed and represent an exciting future area of research.

4.3 PRODUCTS OF GRAPHENE OXIDE OXIDATION – A NOVEL MATERIAL FOR SENSOR APPLICATIONS

Because all of its atoms are located on the surface coupled with its unique structural and electronic properties (*i.e.*, high charge mobility),[206, 257, 258] graphene may be an ideal material for electronic,[257, 259] energy conversion,[260] and chemical sensor[261, 262] applications. Graphene represents a zero bandgap semimetal, and field-effect transistor (FET) devices based on this carbon-based nanomaterial demonstrate small on/off ratios, which limit their electronic applications.[228] Interestingly, defects on the surface of graphene can significantly influence their electronic properties by acting as charge scattering sites; therefore, by introducing extrinsic defects on the basal plane of graphene, it is possible to tailor graphene's electronic transport properties.[263] Similarly, alternative approaches permit the fabrication of narrow graphene nanoribbons (GNRs, <20 nm wide),[264, 265] wherein quantum confinement and edge effects lead to the opening of the band gap and thus render GNRs useful for FET devices.

We hypothesized that holey reduced graphene oxide (hRGO), which was synthesized *via* enzymatic oxidation to generate holes within the basal plane of graphene oxide and subsequently reduced with hydrazine, would represent a synergistic material that contained both defects (*i.e.*, oxygen moieties primarily along the edges) and interconnected nanoribbons that would tailor the electronic properties of graphene.[247] In comparison to RGO, hRGO exhibited a decrease in conductance with a p-type behavior and a positive shift in the Dirac points (Figure 28a).[133] Upon decoration with Pt nanoparticles, which were imparted through electrochemical deposition, and incorporation into FET devices (Figure 31a), hRGO exhibited both a large and selective increase in device conductance response towards increasing concentrations of hydrogen gas at room

temperature. For example, the unoptimized detection limit was 60 ppm, and the devices demonstrated no significant response towards CO (0.25%, Figure 31b), CH_4 (4%, Figure 31b), and relative humidity (11–78%). Interestingly, no Pt poisoning was observed for these devices after CO exposure (Figure 31b). Significantly, devices consisting of RGO decorated with Pt nanoparticles (*i.e.*, Pt-RGO) did not exhibit any significant response to H_2 at room temperature in the tested range (40 to 40,000 ppm). Therefore, since both Pt-RGO and Pt-hRGO had similar coverage of Pt nanoparticles on their basal planes, we attributed the presence of holes on the basal plane for Pt-hRGO, which created more edges containing oxygen functionalities, to be the source of the significantly enhanced response of Pt-hRGO to hydrogen. The high selectivity of Pt-hRGO devices toward hydrogen gas represents a characteristic that can be further exploited for the development of ultrasensitive gas sensors or high efficiency catalyst membranes.

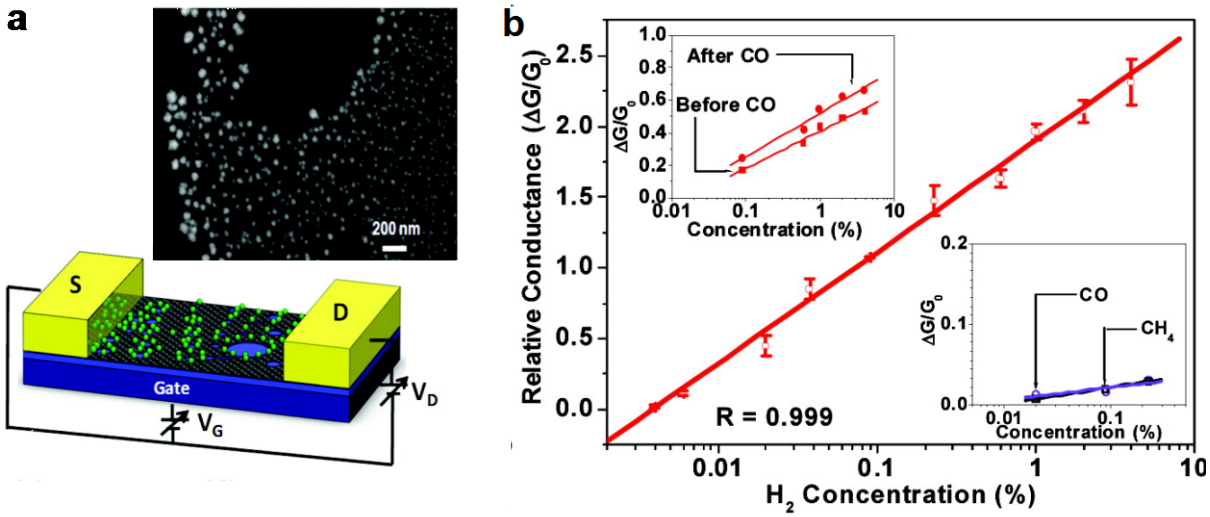

Figure 31. (a) Illustration of the hRGO device decorated with Pt metal nanoparticles. Inset depicts a scanning electron micrograph of Pt-hRGO. (b) Calibration curve of Pt-hRGO for the response to H_2 gas, left inset shows the device response to H_2 before and after exposure to CO (0.25% in N_2) and right inset shows the response to CO (0.05–0.25% in N_2) and CH_4 (0.4–4% in N_2). (Reproduced with permission from [247]. Copyright 2011 American Chemical Society).

5.0 PUBLICATIONS AND POSTER PRESENTATIONS

5.1 PUBLICATIONS

5.1.1 Book Chapters

(2) Kotchey, G. P.; Star, A.: Advances in supramolecular chemistry of carbon nanotubes. In *Supramol. Chem.*; Gale, P. A., Steed, J. W. , Eds.; John Wiley & Sons, Ltd: West Sussex, 2012; Vol. 8; pp 3767-3790.

(1) Kotchey, G. P.; Star, A.: Carbon nanotubes and fullerenes in chemical sensors. In *Chemical sensors*; Korotcenkov, G., Schwank, J., Eds.; Momentum Press, LLC: New York, 2010; Vol. 2; pp 87-140.

5.1.2 Review Articles

(2) Kotchey, G. P.; Zhao, Y.; Kagan, V. E.; Star, A. Peroxidase-mediated biodegradation of carbon nanotubes *in vitro* and *in vivo*. *Adv. Drug Deliver. Rev.* **2013**, DOI: 10.1016/j.addr.2013.07.007.

(1) Kotchey, G. P.; Hasan, S. A.; Kapralov, A. A.; Ha, S. H.; Kim, K.; Shvedova, A. A.; Kagan, V. E.; Star, A., A Natural Vanishing Act: The Enzyme-Catalyzed Degradation of Carbon Nanomaterials. *Acc. Chem. Res.* **2012,** *45*, 1770-1781.

5.1.3 Journal Articles

(12) Chiu, C. F.; Barth, B. A.; Kotchey, G. P.; Zhao, Y.; Gogick, K. A.; Saidi, W. A.; Petoud, S.; Star, A., Enzyme-Catalyzed Oxidation Facilitates the Return of Fluorescence for Single-Walled Carbon Nanotubes. *J. Am. Chem. Soc.* **2013**, DOI: 10.1021/ja400699y.

(11) Kotchey, G. P.; Gaugler, J. A.; Kapralov, A. A.; Kagan, V. E.; Star, A., Effect of Antioxidants on Enzyme-Catalysed Biodegradation of Carbon Nanotubes. *J. Mater. Chem. B* **2013,** *1*, 302-309.

(10) Andón, F. T.; Kapralov, A. A.; Yanamala, N.; Feng, W.; Baygan, A.; Chambers, B. J.; Hultenby, K.; Ye, F.; Toprak, M. S.; Brandner, B. D.; Fornara, A.; Klein-Seetharaman, J.; Kotchey, G. P.; Star, A.; Shvedova, A. A.; Fadeel, B.; Kagan, V. E., Biodegradation of Single-Walled Carbon Nanotubes by Eosinophil Peroxidase. *Small* **2013**, DOI: 10.1002/smll.201202508.

(9) Tkach, A. V.; Yanamala, N.; Stanley, S.; Shurin, M. R.; Shurin, G. V.; Kisin, E. R.; Murray, A. R.; Pareso, S.; Khaliullin, T.; Kotchey, G. P.; Castranova, V.; Mathur, S.; Fadeel, B.; Star, A.; Kagan, V. E.; Shvedova, A. A., Graphene Oxide, but Not Fullerenes, Targets Immunoproteasomes and Suppresses Antigen Presentation by Dendritic Cells. *Small* **2013,** *9*, 1686-1690.

(8) Shvedova, A. A.; Kapralov, A. A.; Feng, W. H.; Kisin, E. R.; Murray, A. R.; Mercer, R. R.; St. Croix, C. M.; Lang, M. A.; Watkins, S. C.; Konduru, N. V.; Allen, B. L.; Conroy, J.; Kotchey, G. P.; Mohamed, B. M.; Meade, A. D.; Volkov, Y.; Star, A.; Fadeel, B.; Kagan, V. E., Impaired Clearance and Enhanced Pulmonary Inflammatory/Fibrotic Response to Carbon Nanotubes in Myeloperoxidase-Deficient Mice. *PLoS One* **2012,** *7*, e30923.

(7) Kapralov, A. A.; Feng, W. H.; Amoscato, A. A.; Yanamala, N.; Balasubramanian, K.; Winnica, D. E.; Kisin, E. R.; Kotchey, G. P.; Gou, P.; Sparvero, L. J.; Ray, P.; Mallampalli, R. K.; Klein-Seetharaman, J.; Fadeel, B.; Star, A.; Shvedova, A. A.; Kagan, V. E., Adsorption of Surfactant Lipids by Single-Walled Carbon Nanotubes in Mouse Lung Upon Pharyngeal Aspiration. *ACS Nano* **2012,** *6*, 4147-4156.

(6) Ding, M.; Sorescu, D. C.; Kotchey, G. P.; Star, A., Welding of Gold Nanoparticles on Graphitic Templates for Chemical Sensing. *J. Am. Chem. Soc.* **2012,** *134*, 3472-3479.

(5) Chen, Y.; Vedala, H.; Kotchey, G. P.; Audfray, A.; Cecioni, S.; Imberty, A.; Vidal, S. b.; Star, A., Electronic Detection of Lectins Using Carbohydrate-Functionalized Nanostructures: Graphene *Versus* Carbon Nanotubes. *ACS Nano* **2012,** *6*, 760-770.

(4) Vedala, H.; Sorescu, D. C.; Kotchey, G. P.; Star, A., Chemical Sensitivity of Graphene Edges Decorated with Metal Nanoparticles. *Nano Lett.* **2011,** *11*, 2342-2347.

(3) Tang, Y.; Kotchey, G. P.; Vedala, H.; Star, A., Electrochemical Detection with Platinum Decorated Carbon Nanomaterials. *Electroanalysis* **2011,** *23*, 870-877.

(2) Kotchey, G. P.; Allen, B. L.; Vedala, H.; Yanamala, N.; Kapralov, A. A.; Tyurina, Y. Y.; Klein-Seetharaman, J.; Kagan, V. E.; Star, A., The Enzymatic Oxidation of Graphene Oxide. *ACS Nano* **2011,** *5*, 2098-2108.

(1) Allen, B. L.; Kotchey, G. P.; Chen, Y.; Yanamala, N. V. K.; Klein-Seetharaman, J.; Kagan, V. E.; Star, A., Mechanistic Investigations of Horseradish Peroxidase-Catalyzed Degradation of Single-Walled Carbon Nanotubes. *J. Am. Chem. Soc.* **2009,** *131*, 17194-17205.

5.2 POSTER PRESENTATIONS

(3) 245th ACS National Meeting and Exposition (New Orleans, LA - 2013). Effect of Antioxidants on Enzyme-catalyzed Biodegradation of Carbon Nanotubes.

(2) 2011 EPA STAR Graduate Fellowship Conference (Washington, D.C. - 2011). The Enzymatic Degradation of Carbon Nanomaterials.

(1) 242nd ACS National Meeting and Exposition (Denver, CO - 2011). Enzymatic Oxidation of Carbon Nanomaterials.

APPENDIX A

EFFECT OF ANTIOXIDANTS ON ENZYME-CATALYZED BIODEGRADATION OF CARBON NANOTUBES – ELECTRONIC SUPPLEMENTARY INFORMATION

This Appendix contains the Electronic Supplementary Information (ESI) for Section 2.2. The content includes: tables detailing the experimental setup (*i.e.*, Table 4, Table 6, Table 7, and Table 8) and supporting Raman spectra (Figure 32), vis-NIR absorption data (Figure 33), S_{22} absorption data for control experiments (Figure 34), EPR studies (Figure 35), ESI-MS spectra (Figure 36), MPO activity assays (Figure 37), absorption *vs.* antioxidant concentration plots (Figure 38), and absorption data for degradation experiments conducted with antioxidant-treated o-SWCNTs (Figure 39).

Table 4. Initial Experimental Conditions

Sample	o-SWCNTs (1 mg/mL)	H_2O_2 (18.75 mM)	AR-MPO (2.0 µM)	BE-MPO	NaCl (5 M)	AA (250 mM)	GSH (250 mM)	PB/DTPA (0.1 M/ 300 µM)
o-SWCNT	7 µL	0	0	0	0	0	0	243 µL
o-SWCNT + MPO	7 µL	0	0	4.8 µL	0	0	0	238.2 µL
o-SWCNT + H_2O_2	7 µL	1 µL	0	0	0	0	0	242 µL
o-SWCNT + MPO + H_2O_2 − Cl^-	7 µL	1 µL	0	4.8 µL	0	0	0	237.2 µL
o-SWCNT + MPO + H_2O_2 + Cl^-	7 µL	1 µL	4 µL	0	7 µL	0	0	231 µL
o-SWCNT + AA	7 µL	0	0	0	0	1 µL	0	242 µL
o-SWCNT + MPO + AA	7 µL	0	0	4.8 µL	0	1 µL	0	237.2 µL
o-SWCNT + MPO + H_2O_2 − Cl^- + AA	7 µL	1 µL	0	4.8 µL	0	1 µL	0	236.2 µL
o-SWCNT + MPO + H_2O_2 + Cl^- + AA	7 µL	1 µL	4 µL	0	7 µL	1 µL	0	230 µL

o-SWCNT + GSH	7 µL	0	0	0	0	0	1 µL	242 µL
o-SWCNT + MPO + GSH	7 µL	0	0	4.8 µL	0	0	1 µL	237.2 µL
o-SWCNT + MPO + $H_2O_2 - Cl^-$ + GSH	7 µL	1 µL	0	4.8 µL	0	0	1 µL	236.2 µL
o-SWCNT + MPO + $H_2O_2 + Cl^-$ + GSH	7 µL	1 µL	4 µL	0	7 µL	0	1 µL	230 µL

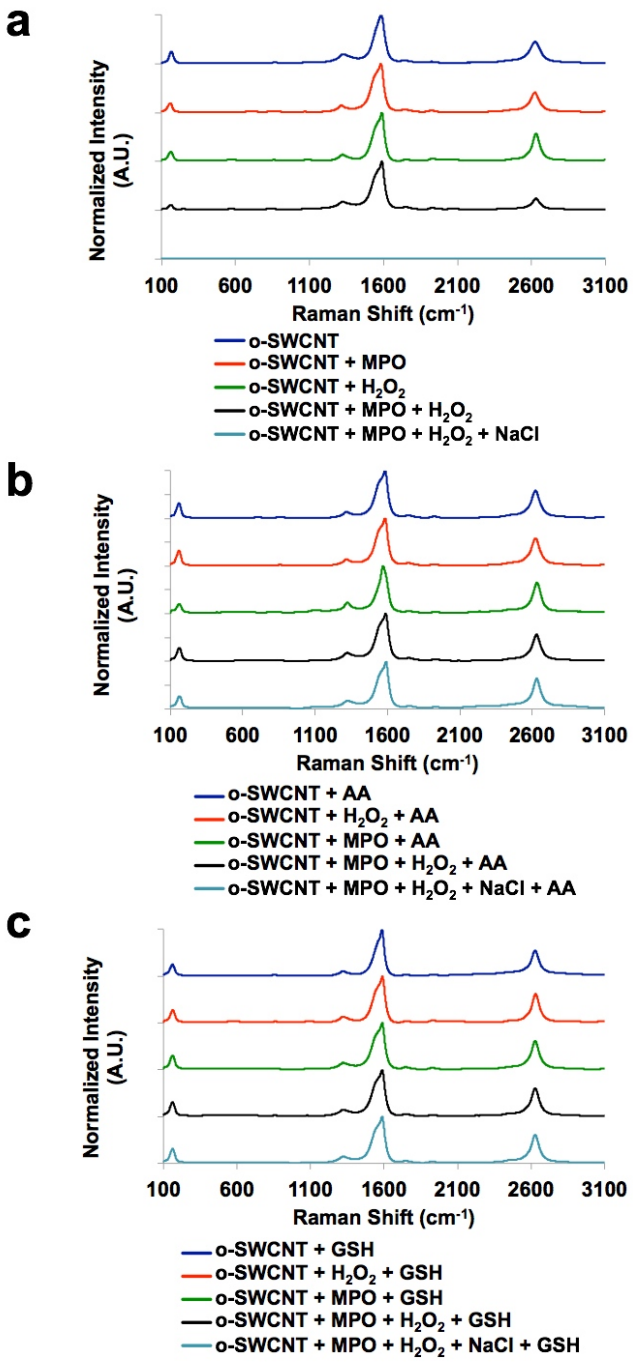
a
Normalized Intensity (A.U.)
100
600
1100
1600
2100
2600
3100
Raman Shift (cm-1)
o-SWCNT
o-SWCNT + MPO
o-SWCNT + H2O2
o-SWCNT + MPO + H2O2
o-SWCNT + MPO + H2O2 + NaCl
b
Normalized Intensity (A.U.)
100
600
1100
1600
2100
2600
3100
Raman Shift (cm-1)
o-SWCNT + AA
o-SWCNT + H2O2 + AA
o-SWCNT + MPO + AA
o-SWCNT + MPO + H2O2 + AA
o-SWCNT + MPO + H2O2 + NaCl + AA
c
Normalized Intensity (A.U.)
100
600
1100
1600
2100
2600
3100
Raman Shift (cm-1)
o-SWCNT + GSH
o-SWCNT + H2O2 + GSH
o-SWCNT + MPO + GSH
o-SWCNT + MPO + H2O2 + GSH
o-SWCNT + MPO + H2O2 + NaCl + GSH

Figure 32. Raman spectroscopy performed on (a) o-SWCNTs samples, (b) o-SWCNTs samples treated with AA, and o-SWCNTs samples treated with GSH. Reprinted with permission from [152]. Copyright 2013 Royal Society of Chemistry).

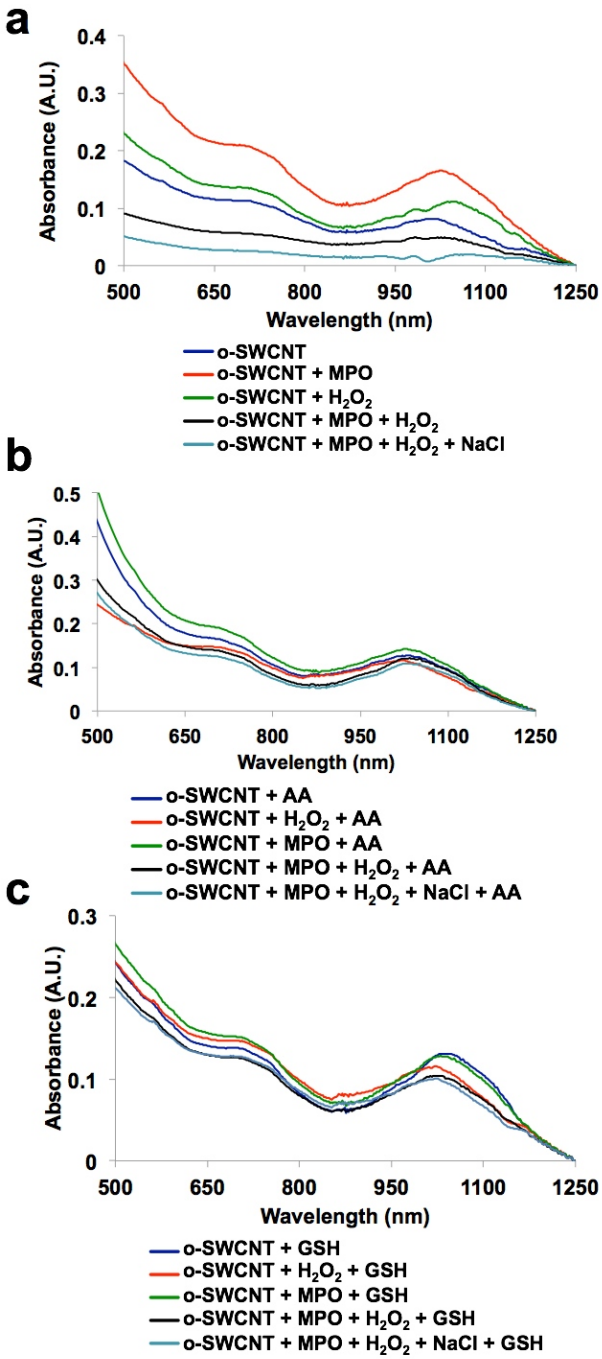

Figure 33. vis−NIR absorption spectra for (a) o-SWCNTs samples, (b) o-SWCNTs samples treated with AA, and o-SWCNTs samples treated with GSH. Reprinted with permission from [152]. Copyright 2013 Royal Society of Chemistry).

Table 5. Area of S_{22} Peaks

Sample	Area of S_{22} Peak
o-SWCNT	8.135
o-SWCNT + MPO + H_2O_2	2.980
o-SWCNT + MPO + H_2O_2 + NaCl	1.962
o-SWCNT + MPO + H_2O_2 + GSH	7.425
o-SWCNT + MPO + H_2O_2 + NaCl + GSH	7.981
o-SWCNT + MPO + H_2O_2 + AA	9.698
o-SWCNT + MPO + H_2O_2 + NaCl + AA	10.627

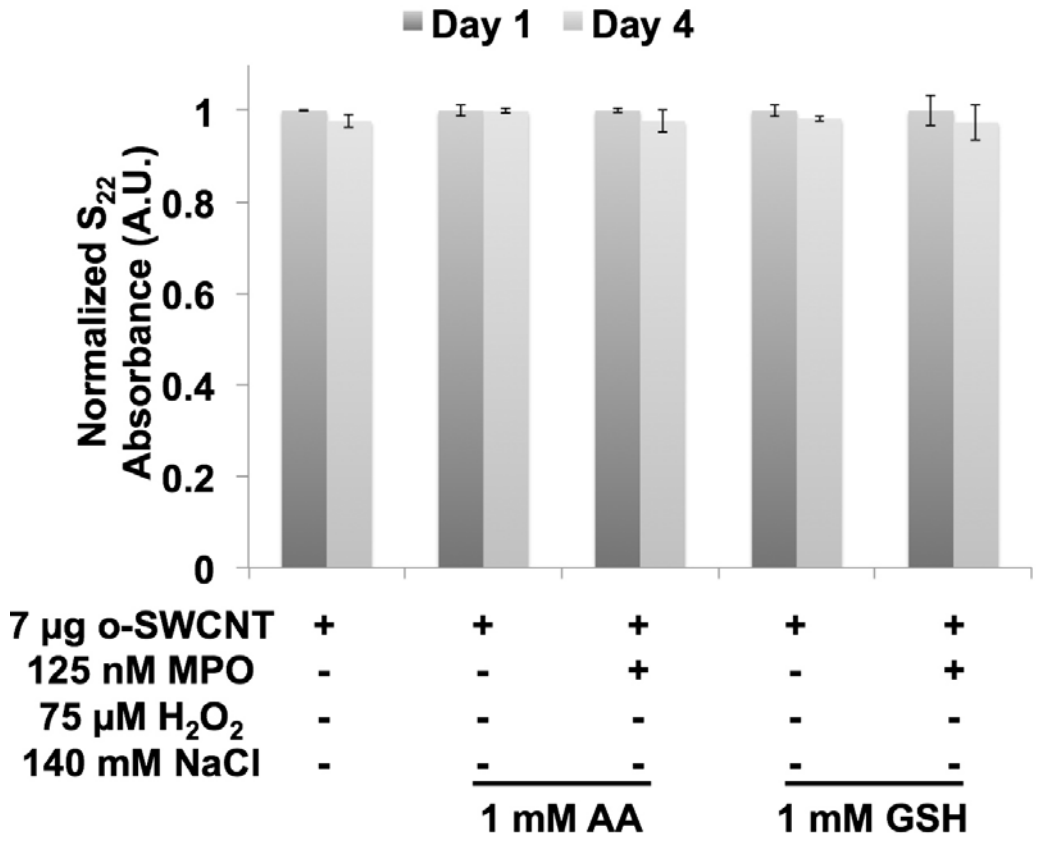

Figure 34. S_{22} absorbance intensity of o-SWCNTs at day 0 and day 4 for the given control experiments. The error bar represents standard error of the mean with a sample size of three. Reprinted with permission from [152]. Copyright 2013 Royal Society of Chemistry).

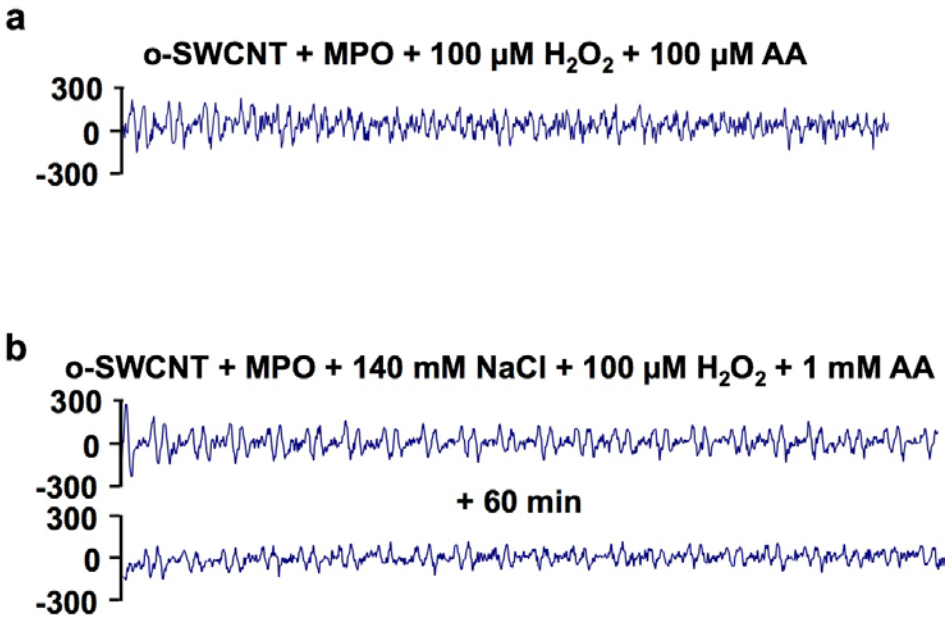

Figure 35. Results of an electron paramagnetic resonance (EPR) study, which demonstrates the presence of the ascorbate radical (a) under conditions consisting of o-SWCNTs, MPO, and H_2O_2 and (b) after a 60-minute incubation with a system consisting of o-SWCNTs, MPO, NaCl, and H_2O_2. Reprinted with permission from [152]. Copyright 2013 Royal Society of Chemistry).

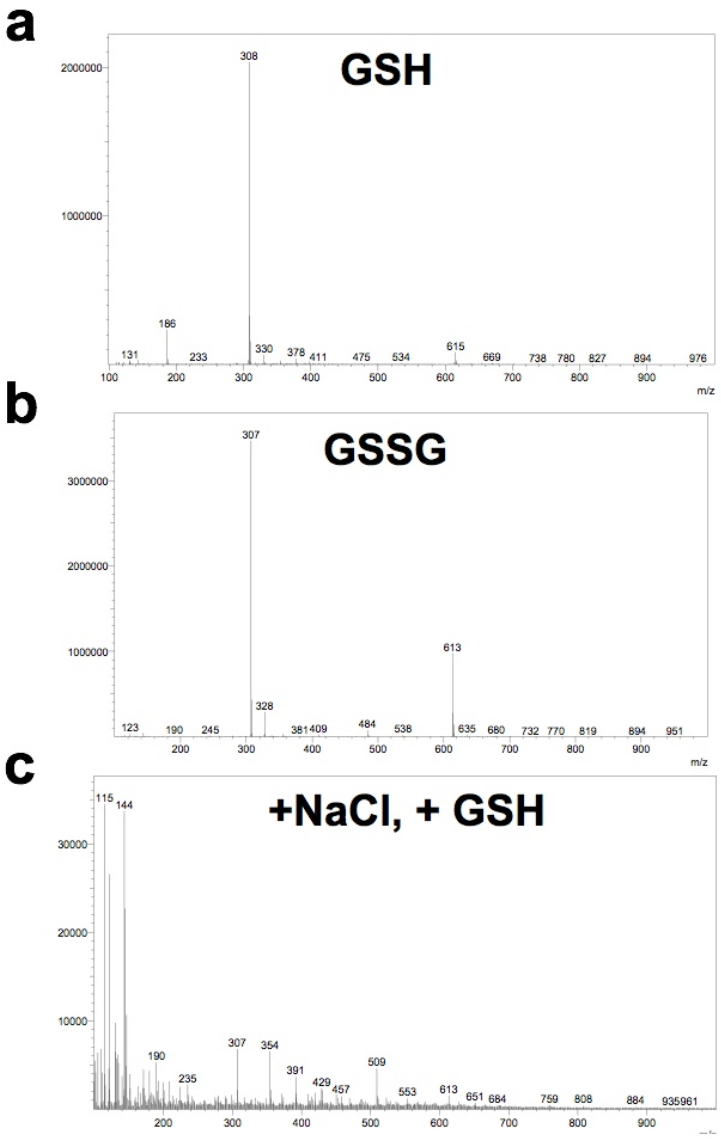

Figure 36. Electrospray ionization mass spectrometry (ESI-MS) data (positive mode) for (a) GSH, (b) oxidized GSH (GSSG), (c) o-SWCNTs samples treated with both GSH and NaCl. Reprinted with permission from [152]. Copyright 2013 Royal Society of Chemistry).

Table 6. Experimental Conditions for MPO Activity Assay Employing Amplex Red

Sample	Amplex Red (10 mM)	H_2O_2 (10 mM)	AR-MPO*	BE-MPO*	AA (250 mM)	GSH (250 mM)	PB/DTPA (0.1 M/ 300 µM)
AR MPO + H_2O_2 − Cl^-	3 µL	3 µL	4 µL	0	0	0	590 µL
BE MPO + H_2O_2 − Cl^-	3 µL	3 µL	0	4.8 µL	0	0	589.2 µL
***Diluted 1/200 with PB/DTPA**							

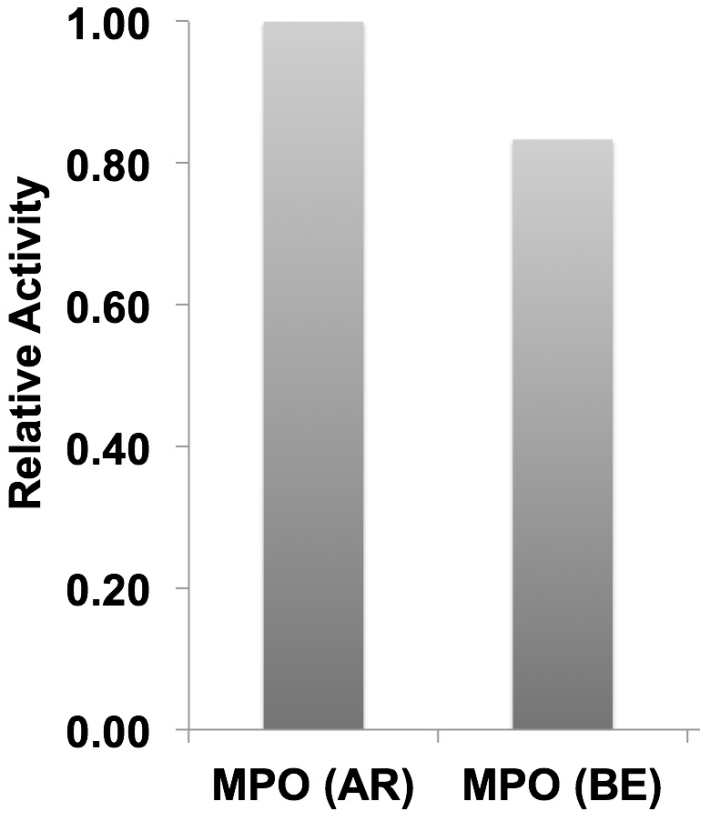

Figure 37. Comparison of the relative activity of as received (AR) MPO and buffer exchanged (BE) MPO derived from a fluorescence-based kinetic experiment employing Amplex red. Reprinted with permission from [152]. Copyright 2013 Royal Society of Chemistry).

A.1 EFFECT OF CHANGING THE ANTIOXIDANT CONCENTRATION ON O-SWCNT DEGRADATION

The effect of changing the antioxidant concentration on o-SWCNT degradation was analyzed. The variable AA final concentrations were 50 µM, 100 µM, 250 µM, 500 µM, and 1 mM; the GSH concentrations were 10 nM, 50 nM, 100 nM, 250 nM, 500 nM, 1 µM, 10 µM, 50 µM, 100 µM mM, 250 µM, 500 µM, and 1 mM. The experiments were performed in triplicate using 96 well plates. Table 7 details the initial experimental conditions for the 1 mM data point. Again, the Epoch microplate spectrophotometer was employed to obtain initial (Day 0) absorbance reading at 999 nm. Every hour, 75 µM H_2O_2 (final) and the respective AA (50 µM, 100 µM, 250 µM, 500 µM, and 1 mM) and GSH (10 nM, 50 nM, 100 nM, 250 nM, 500 nM, 1 µM, 10 µM, 50 µM, 100 µM mM, 250 µM, 500 µM, and 1 mM) concentrations (final) were dispensed for a total of 7 additions on day 0 and 8 additions on days 1, 2 and 3. On days 1, 2 and 3, 4 µL of AR MPO and 4.8 µL of BE MPO were added to the samples (according to Table 7, MPO columns). Between additions and overnight, the samples were incubated at 37 °C in an incubator. Finally, on day 4 (96 h), the Epoch microplate spectrophotometer was again used to measure the absorbance at 999 nm. The data is presented in Figure 38 as the relative change compared to when zero antioxidant is utilized.

Table 7. Initial Conditions for Experiments with Different Antioxidant Concentration – 1 mM Data Point

Sample	o-SWCNTs (1 mg/mL)	H_2O_2 (18.75 mM)	AR MPO (2.0 µM)	BE MPO	NaCl (5 M)	AA (250 mM)	GSH (250 mM)	PB/DTPA (0.1 M/ 300 µM)
o-SWCNT + MPO + H_2O_2 − Cl^- + AA	7 µL	1 µL	0	4.8 µL	0	1 µL	0	236.2 µL
o-SWCNT + MPO + H_2O_2 + Cl^- + AA	7 µL	1 µL	4 µL	0	7 µL	1 µL	0	230 µL
o-SWCNT + MPO + H_2O_2 − Cl^- + GSH	7 µL	1 µL	0	4.8 µL	0	0	1 µL	236.2 µL
o-SWCNT + MPO + H_2O_2 + Cl^- + GSH	7 µL	1 µL	4 µL	0	7 µL	0	1 µL	230 µL

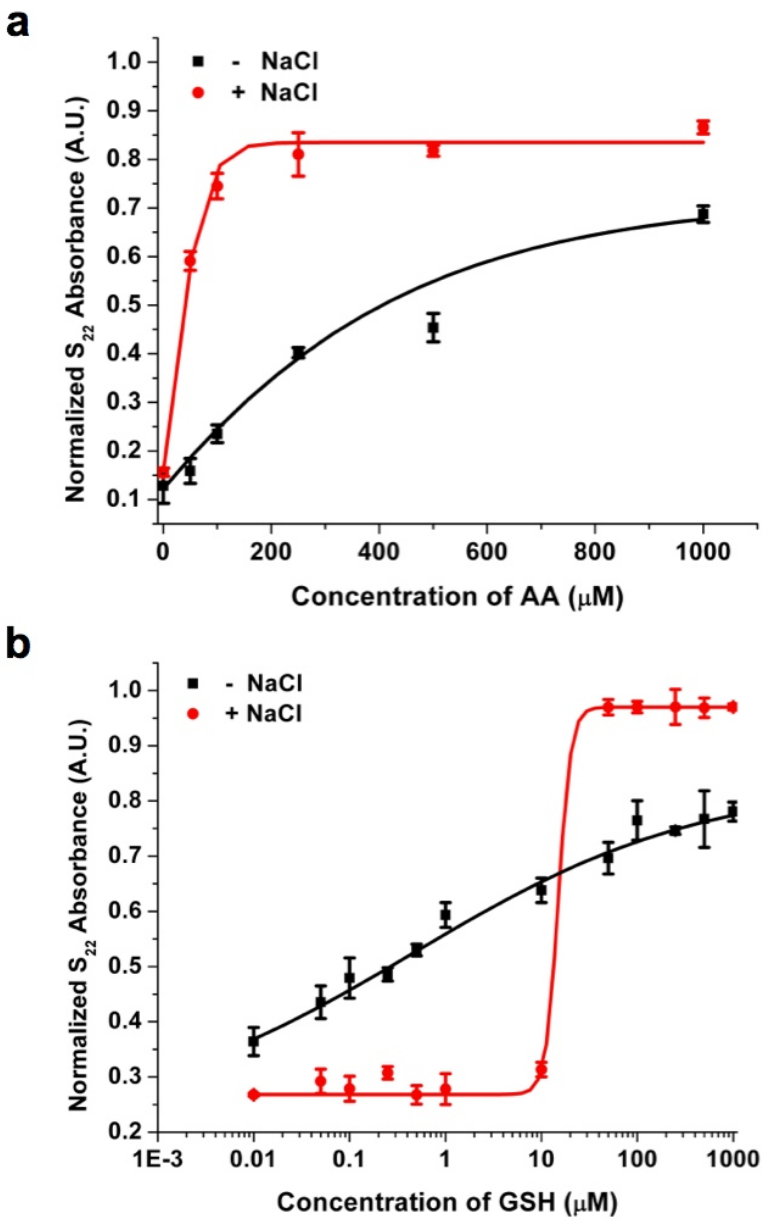

Figure 38. The effect of changing (a) AA and (b) GSH concentrations on the relative change in S_{22} absorbance for the MPO system with (red) and without (black) NaCl. Reprinted with permission from [152]. Copyright 2013 Royal Society of Chemistry).

A.2 DEGRADATION EXPERIMENTS WITH ANTIOXIDANT TREATED O-SWCNTS

To ascertain if the reduction of functional groups belonging to o-SWCNTs by antioxidants hindered enzyme-catalyzed degradation, the nanotubes were first treated with the antioxidants and subsequently subjected to enzymatic treatment under $\pm Cl^-$ conditions. To this end, 1 mg of P3 o-SWCNTs was added to 10 mL of nanopure water in a glass vial and sonicated for 5 minutes. To this vial, a final concentration of 3.6 mM AA was added for a total of 8 additions per day for 4 days (32 additions total). Between additions, the vial was covered with aluminum foil and incubated at 37 °C with shaking. Note that the concentration of AA utilized was derived from the antioxidant experiments (*i.e.*, 1 mM) and proportionally adjusted for the higher concentration of nanotubes (0.1 mg/mL). A second vial was created for GSH following an identical procedure described above. After 96 hours of incubation, the nanotubes were filtered employing TefSep PTFE membrane filters; the nanotubes were washed with 100 mL each of nanopure water, 0.01 M NaOH, 0.01 M HCl, and nanopure water. Finally, the dried antioxidant-treated o-SWCNT samples were weighed and sonicated into 0.1 mM phosphate buffer at a final concentration of 1 mg/mL. Table 8 details the initial experimental conditions, which were performed in triplicate using 96 well plates. Every hour, 75 µM H_2O_2 (final) were dispensed for a total of 7 additions on day 0 and 8 additions on days 1, 2 and 3. On days 1, 2 and 3, 4 µL of AR MPO and 4.8 µL of BE MPO were added to the samples (according to Table 8, MPO columns). Between additions, the samples were incubated at 37 °C in an incubator. Finally, on day 4 (96 h), the Epoch microplate spectrophotometer was again used to measure the absorbance at 999 nm.

Table 8. Initial Conditions for Experiments with Antioxidant-Treated o-SWCNTs

Sample	AA-o-SWCNTs (1 mg/mL)	GSH-o-SWCNTs (1 mg/mL)	H_2O_2 (18.75 mM)	AR MPO (2.0 µM)	BE MPO	NaCl (5 M)	PB/DTPA (0.1 M/ 300 µM)
AA-o-SWCNT + MPO + H_2O_2 − Cl^-	7 µL	0	1 µL	0	4.8 µL	0	237.2 µL
AA-o-SWCNT + MPO + H_2O_2 + Cl^-	7 µL	0	1 µL	4 µL	0	7 µL	231 µL
GSH-o-SWCNT + MPO + H_2O_2 − Cl^-	0	7 µL	1 µL	0	4.8 µL	0	237.2 µL
GSH-o-SWCNT + MPO + H_2O_2 + Cl^-	0	7 µL	1 µL	4 µL	0	7 µL	231 µL

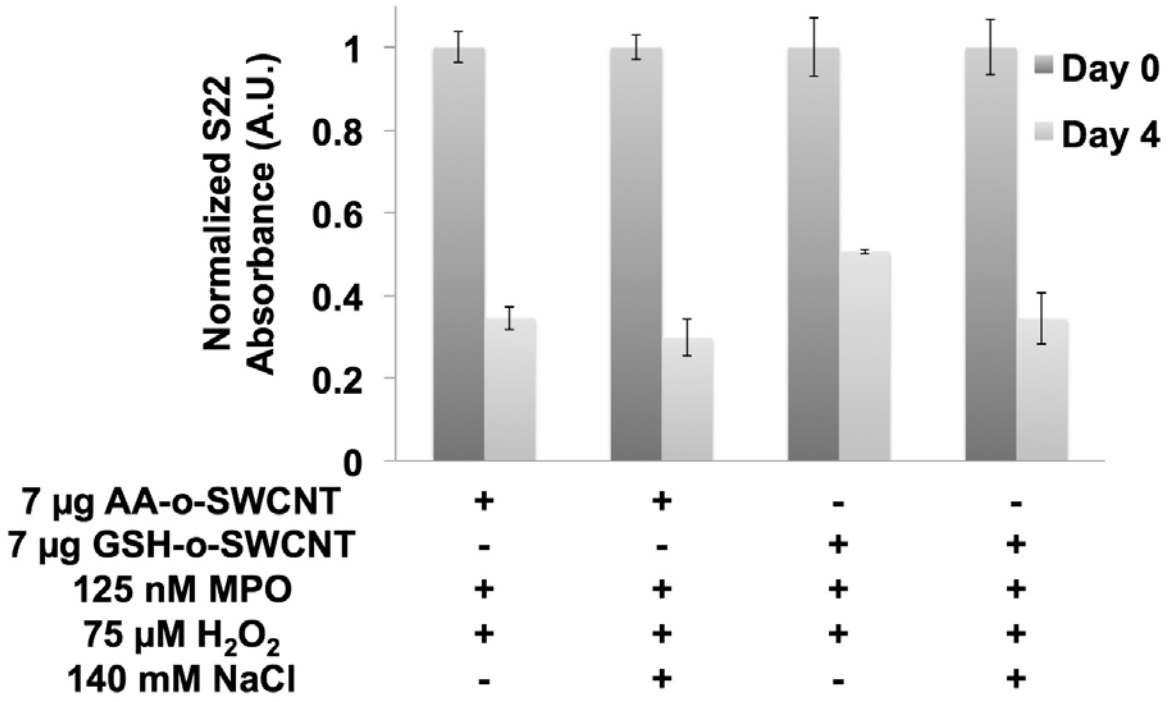

Figure 39. S_{22} absorbance intensity for antioxidant-treated o-SWCNTs under given experimental conditions at day 0 and day 4. The error bar represents standard error of the mean with a sample size of three. Reprinted with permission from [152]. Copyright 2013 Royal Society of Chemistry).

APPENDIX B

THE ENZYMATIC OXIDATION OF GRAPHENE OXIDE – SUPPORTING INFORMATION

This Appendix contains the Supporting Information (SI) for Section 3.2. The content includes: Supplemental TEM micrographs for the graphene oxide and RGO experiments (Figure 40), Amplex Red assay for days 1 and 20 of RGO oxidation (Figure 41), electron paramagnetic resonance (EPR) spectroscopy data (Figure 42), AFM images with section analysis of graphene oxide, HRP, and RGO (Figure 43), details of the predicted interaction sites for RGO, graphene oxide, and holey graphene oxide on HRP (Table 9), back gate FET data for hRGO and RGO (Figure 44), and FT-IR and UV-vis spectra of hRGO, RGO, and graphene oxide (Figure 45).

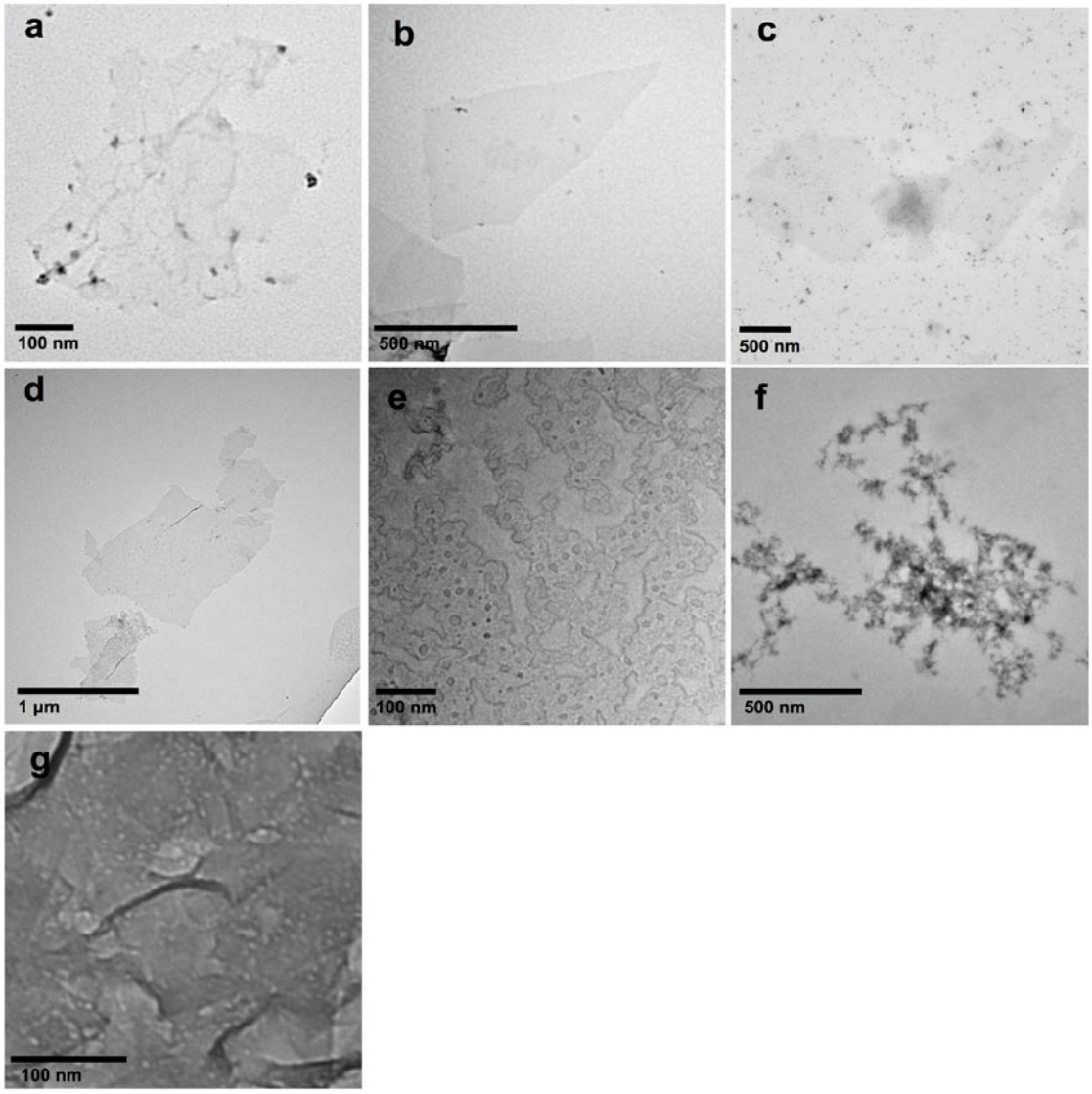

Figure 40. TEM micrographs of (a) graphene oxide-control I (–H_2O_2) and (b) graphene oxide-control II (–HRP) after 10 days of incubation. TEM micrographs of (c) reduced graphene oxide (RGO)-control I (–H_2O_2) and (d) RGO-control II (–HRP) after 10 days of incubation. (e) Holey graphene oxide formed by adding 40 µM H_2O_2 (final concentration) every 30 minutes for 4.5 hours to a dispersion initially containing graphene oxide and HRP. (f) "Over-oxidized" graphene oxide formed by using identical conditions as (e). (g) Holey reduced graphene oxide (hRGO) formed by chemically reducing the holey graphene oxide formed after 8 day of incubation with HRP/H_2O_2 with hydrazine. (Reproduced with permission from [133]. Copyright 2011 American Chemical Society).

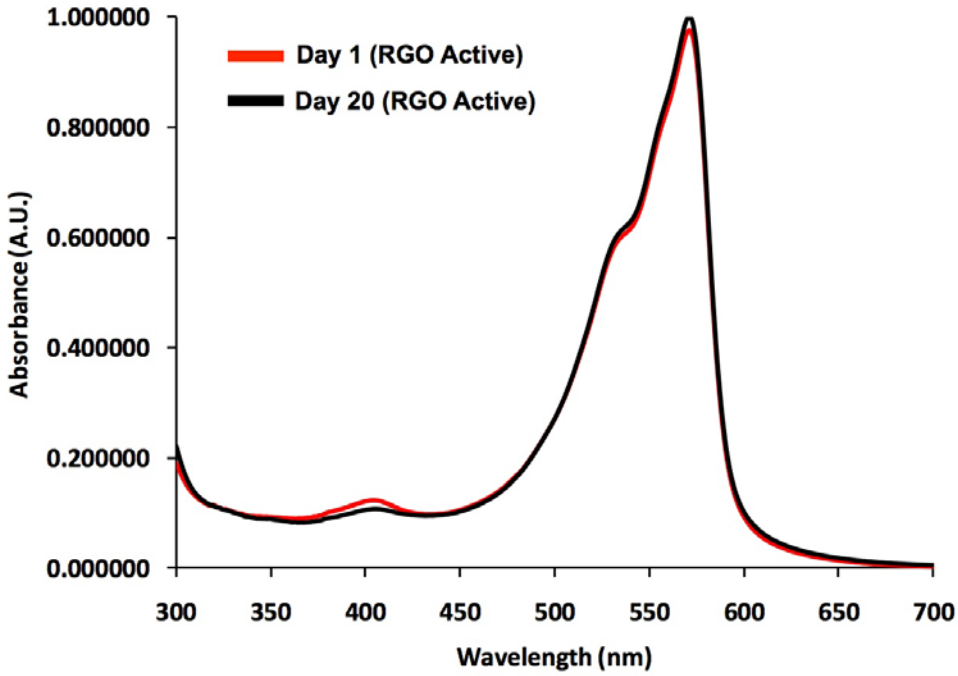

Figure 41. Amplex Red UV-Vis spectroscopic study conducted on days 1 and 20 of the reduced graphene oxide (RGO)/HRP/H_2O_2 sample. (Reproduced with permission from [133]. Copyright 2011 American Chemical Society).

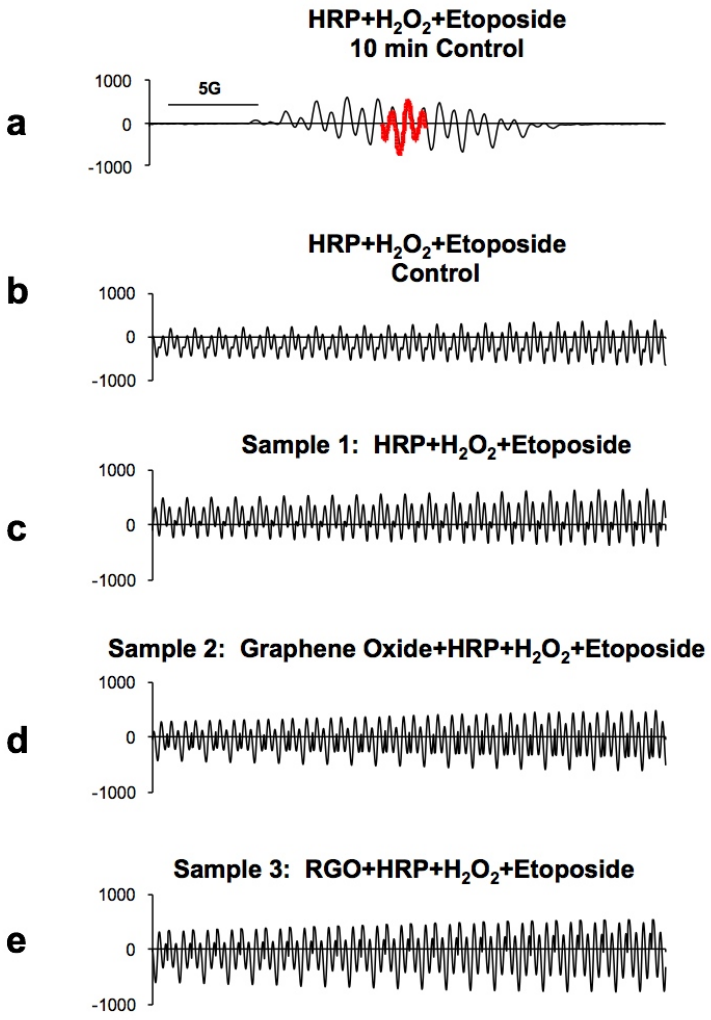

Figure 42. Electron paramagnetic resonance (EPR) spectroscopy data. To each sample containing HRP (0.35 µM) and etoposide (200 µM), H_2O_2 (80 µM) was added, and either a full ESR spectra (a) or the time course of the EPR signal (b-e) were recorded. The duration of the recordings were 10 min for sample (a), and 1 min for the time course of the EPR signals (b-e). Sample (d) contained graphene oxide (5×10^{-5} mg/ml), and sample (e) contained reduced graphene oxide (RGO) (5×10^{-5} mg/ml). (Reproduced with permission from [133]. Copyright 2011 American Chemical Society).

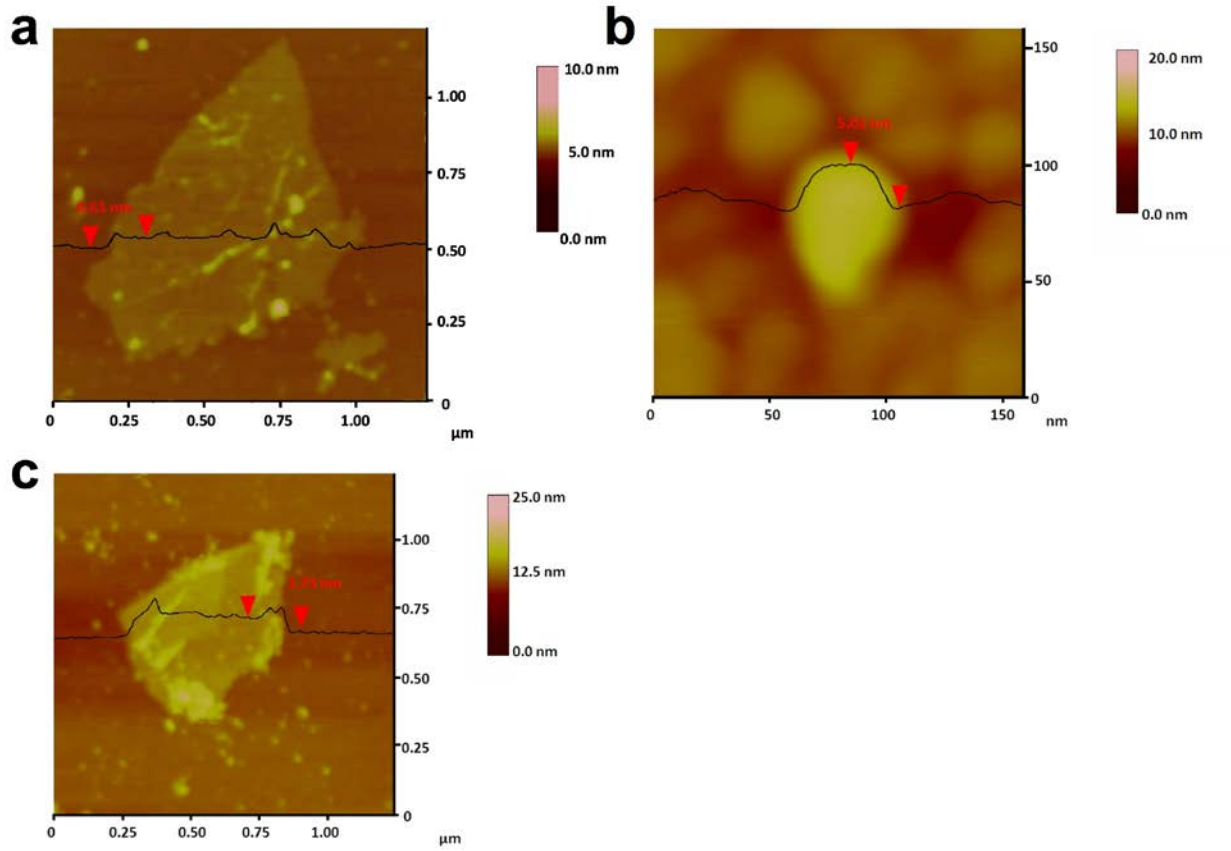

Figure 43. Atomic force microscopy (AFM) images with section analysis of (a) graphene oxide, (b) horseradish peroxidase (HRP), and (c) reduced graphene oxide (RGO). The heights determined by section analysis are 0.61 nm, 5.02 nm, and 1.73 nm, respectively. (Reproduced with permission from [133]. Copyright 2011 American Chemical Society).

Table 9. Details of the Predicted Interaction Sites for Reduced Graphene Oxide, Graphene Oxide and Holey Graphene Oxide on HRP

Structure	Binding Site 1		Binding Site 2	
	Binding Energy	Residues with in 5Å	Binding Energy	Residues with in 5Å
Reduced Graphene Oxide	**-26.7 kcal/mol**	Asn24, Arg27, Ser28, Asp29, Asp56, Asn57, Thr58, Thr59, Arg62, Asp66, Asn72, Pro78, Asp81, Arg82, Ala85, Arg178, Ser216, Ala217, Asn214, Gly213, Asn300, Arg302, Val303, Val304, Ser306	-	-
Graphene Oxide	**-24.8 kcal/mol**	Asn24, Glu25, Arg27, Ser28, Asp56, Asn57, Thr58, Thr59, Phe77, Pro78, Val79, Asp81, Arg82, Ala85, Ala86, Glu88, Ser89, Pro92, Lue299, Asn300, Arg302, Val303, Val304, Ser306	**-22.4 kcal/mol**	Leu26, Arg27, Pro30, Lys174, Thr200, Tyr201, Gln203, Thr204, Leu205, Arg206, Gly207, Leu208, Pro210, Leu218, Asp220, Leu223, Arg224, Thr225, Pro226 Thr227, Ile228, Lys241
Holey Graphene Oxide	-	-	**-22.4 kcal/mol**	Ser28, Asp29, Pro30, Lys174, Thr200, Tyr201, Gln203, Thr204, Leu205, Arg206, Gly207, Leu208, Pro210, Leu211, Asn212, Gly213, Asn214, Ala217, Leu218, Val219, Asp220, Asp222, Leu223, Arg224, Thr225, Pro226, Thr227, Ile228

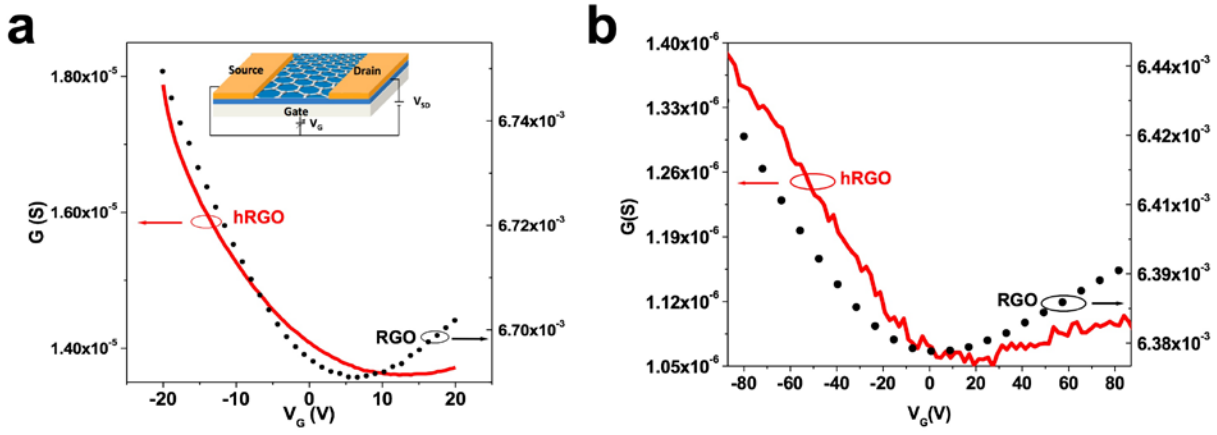

Figure 44. (a) Conductivity *versus* potential (back gate) plot for reduced graphene oxide (RGO, black circles) and holey reduced graphene oxide (hRGO, solid red line). The measurements were recorded at a constant drain-source voltage of 10 mV. Inset represents a schematic of the experimental setup. (b) Transfer characteristics (Gate voltage (V_G) *versus* Conductance (G)) of RGO (black circles) and hRGO (solid red line) measured under ambient conditions and a constant drain-source voltage of 50 mV. (Reproduced with permission from [133]. Copyright 2011 American Chemical Society).

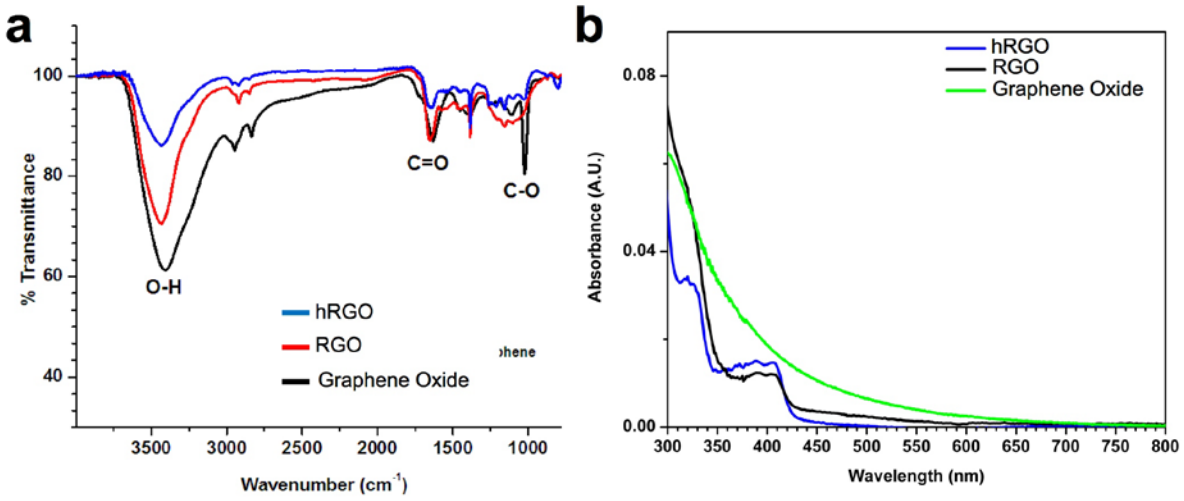

Figure 45. (a) FT-IR spectra of holey reduced graphene oxide (hRGO), reduced graphene oxide (RGO), and graphene oxide. (B) UV-Vis spectra of hRGO, RGO, and graphene oxide. (Reproduced with permission from [133]. Copyright 2011 American Chemical Society).

BIBLIOGRAPHY

1. Kotchey, G. P.; Star, A., Carbon Nanotubes and Fullerenes in Chemical Sensors. In *Chemical Sensors*, Korotcenkov, G.; Schwank, J., Eds. Momentum Press, LLC: New York, 2010; Vol. 2, pp 87-140.

2. Kotchey, G. P.; Star, A., Advances in Supramolecular Chemistry of Carbon Nanotubes. In *Supramol. Chem.*, Gale, P. A.; Steed, J. W., Eds. John Wiley & Sons, Ltd: West Sussex, United Kingdom, 2012; Vol. 8, pp 3767-90.

3. Kotchey, G. P., et al., A Natural Vanishing Act: The Enzyme-Catalyzed Degradation of Carbon Nanomaterials. *Acc. Chem. Res.* **2012,** *45*, 1770-81.

4. Kotchey, G. P., et al., Peroxidase-Mediated Biodegradation of Carbon Nanotubes *in Vitro* and *in Vivo*. *Adv. Drug Deliver. Rev.* **2013**, DOI: 10.1016/j.addr.2013.07.007.

5. Dresselhaus, M. S., et al., *Carbon Nanotubes: Synthesis, Structure, Properties, and Applications*. Springer: Berlin, 2001.

6. Iijima, S., Helical Microtubules of Graphitic Carbon. *Nature* **1991,** *354*, 56-8.

7. Kosakovskaya, Z., Y, et al., Nanofilament Carbon Structure. *JETP Lett.* **1992,** *56*.

8. Gal'pern, E., G, et al., Atomic and Electronic-Structure of the Barrelenes B-Cm with M=36+12n. *JETP Lett.* **1992,** *55*.

9. Iijima, S.; Ichihashi, T., Single-Shell Carbon Nanotubes of 1-Nm Diameter. *Nature* **1993,** *363*, 603-5.

10. Bethune, D. S., et al., Cobalt-Catalyzed Growth of Carbon Nanotubes with Single-Atomic-Layer Walls. *Nature* **1993,** *363,* 605-7.

11. Dresselhaus, M. S., et al., Carbon Fibers Based on Fullerene (C60) and Their Symmetry. *Phys. Rev. B: Condens. Matter Mater. Phys.* **1992,** *45,* 6234-42.

12. Mintmire, J. W., et al., Are Fullerene Tubules Metallic? *Phys. Rev. Lett.* **1992,** *68,* 631-4.

13. Hamada, N., et al., New One-Dimensional Conductors: Graphitic Microtubules. *Phys. Rev. Lett.* **1992,** *68,* 1579-81.

14. Kim, S. N., et al., Carbon Nanotubes for Electronic and Electrochemical Detection of Biomolecules. *Adv. Mater.* **2007,** *19,* 3214-28.

15. Kauffman, D. R.; Star, A., Carbon Nanotube Gas and Vapor Sensors. *Angew. Chem., Int. Ed.* **2008,** *47,* 6550-70.

16. Bethune, D. S., et al., Atoms in Carbon Cages: The Structure and Properties of Endohedral Fullerenes. *Nature* **1993,** *366,* 123-28.

17. Thess, A., et al., Crystalline Ropes of Metallic Carbon Nanotubes. *Science* **1996,** *273,* 483-87.

18. Bronikowski, M. J., et al. In *Gas-Phase Production of Carbon Single-Walled Nanotubes from Carbon Monoxide Via the Hipco Process: A Parametric Study,* The 47th international symposium: Vacuum, thin films, surfaces/interfaces, and processing NAN06, Boston, Massachusetts (USA), AVS: Boston, Massachusetts (USA), 2001; pp 1800-05.

19. Zheng, F., et al., Carbon Nanotube Synthesis Using Mesoporous Silica Templates. *Nano Lett.* **2002,** *2,* 729-32.

20. Subashini, D.; Pandurangan, A., Synthesis of Mesoporous Molecular Sieves as Catalytic Template for the Growth of Single Walled Carbon Nanotubes. *Catal. Commun.* **2007,** *8,* 1665-70.

21. Jasti, R., et al., Synthesis, Characterization, and Theory of [9]-, [12]-, and [18]Cycloparaphenylene: Carbon Nanohoop Structures. *J. Am. Chem. Soc.* **2008,** *130,* 17646-47.

22. Duesberg, G. S., et al., Chromatographic Size Separation of Single-Wall Carbon Nanotubes. *Applied Physics A* **1998,** *67,* 117-19.

23. Zheng, M.; Semke, E. D., Enrichment of Single Chirality Carbon Nanotubes. *J. Am. Chem. Soc.* **2007,** *129,* 6084-85.

24. Bauer, B. J., et al., Measurement of Single-Wall Nanotube Dispersion by Size Exclusion Chromatography†. *The Journal of Physical Chemistry C* **2007,** *111,* 17914-18.

25. Green, A. A.; Hersam, M. C., Ultracentrifugation of Single-Walled Nanotubes. *Materials Today* **2007,** *10,* 59-60.

26. Yanagi, K., et al., Optical and Conductive Characteristics of Metallic Single-Wall Carbon Nanotubes with Three Basic Colors; Cyan, Magenta, and Yellow. *Applied Physics Express* **2008,** *1,* 034003.

27. Sgobba, V.; Guldi, D. M., Carbon Nanotubes-Electronic/Electrochemical Properties and Application for Nanoelectronics and Photonics. *Chem. Soc. Rev.* **2009,** *38,* 165-84.

28. Collins, P. G., et al., Extreme Oxygen Sensitivity of Electronic Properties of Carbon Nanotubes. *Science* **2000,** *287,* 1801-04.

29. Derycke, V., et al., Controlling Doping and Carrier Injection in Carbon Nanotube Transistors. *Appl. Phys. Lett.* **2002,** *80,* 2773-75.

30. Tans, S. J., et al., Room-Temperature Transistor Based on a Single Carbon Nanotube. *Nature* **1998,** *393,* 49-52.

31. Martel, R., et al., Single- and Multi-Wall Carbon Nanotube Field-Effect Transistors. *Appl. Phys. Lett.* **1998,** *73,* 2447-49.

32. Snow, E. S., et al., Random Networks of Carbon Nanotubes as an Electronic Material. *Appl. Phys. Lett.* **2003,** *82,* 2145-47.

33. Tasis, D., et al., Chemistry of Carbon Nanotubes. *Chem. Rev.* **2006,** *106,* 1105-36.

34. Balavoine, F., et al., Helical Crystallization of Proteins on Carbon Nanotubes: A First Step Towards the Development of New Biosensors. *Angew. Chem., Int. Ed.* **1999,** *38,* 1912-15.

35. Bradley, K., et al., Charge Transfer from Adsorbed Proteins. *Nano Lett.* **2004,** *4,* 253-56.

36. Zheng, M., et al., DNA-Assisted Dispersion and Separation of Carbon Nanotubes. *Nat. Mater.* **2003,** *2,* 338-42.

37. Star, A., et al., Starched Carbon Nanotubes. *Angewandte Chemie-International Edition* **2002,** *41,* 2508-12.

38. Star, A., et al., Preparation and Properties of Polymer-Wrapped Single-Walled Carbon Nanotubes. *Angew. Chem., Int. Ed.* **2001,** *40,* 1721-25.

39. O'connell, M. J., et al., Reversible Water-Solubilization of Single-Walled Carbon Nanotubes by Polymer Wrapping. *Chem. Phys. Lett.* **2001,** *342,* 265-71.

40. Star, A., et al., Noncovalent Side-Wall Functionalization of Single-Walled Carbon Nanotubes. *Macromolecules* **2003,** *36,* 553-60.

41. Didenko, V. V., et al., Visualization of Individual Single-Walled Carbon Nanotubes by Fluorescent Polymer Wrapping. *Nano Lett.* **2005,** *5,* 1563-67.

42. Zhang, W., et al., Modular Functionalization of Carbon Nanotubes and Fullerenes. *J. Am. Chem. Soc.* **2009,** *131,* 8446-54.

43. Bahr, J. L.; Tour, J. M., Covalent Chemistry of Single-Wall Carbon Nanotubes. *J. Mater. Chem.* **2002,** *12,* 1952-58.

44. Banerjee, S., et al., Covalent Surface Chemistry of Single-Walled Carbon Nanotubes. *Advanced Materials (Weinheim, Germany)* **2005,** *17*, 17-29.

45. Peng, X.; Wong, S. S., Functional Covalent Chemistry of Carbon Nanotube Surfaces. *Adv. Mater.* **2009,** *21*, 625-42.

46. Bonifazi, D., et al., Supramolecular [60]Fullerene Chemistry on Surfaces. *Chem. Soc. Rev.* **2007,** *36*, 390-414.

47. Diederich, F.; Gomez-Lopez, M., Supramolecular Fullerene Chemistry. *Chem. Soc. Rev.* **1999,** *28*, 263-77.

48. Diederich, F.; Thilgen, C., Covalent Fullerene Chemistry. *Science* **1996,** *271*, 317-23.

49. Thilgen, C., et al., Spacer-Controlled Multiple Functionalization of Fullerenes. *Top. Curr. Chem.* **2005,** *248*, 1-61.

50. Yang, W., et al., Carbon Nanotubes for Biological and Biomedical Applications. *Nanotechnology* **2007,** *18*, 412001.

51. Yu, X., et al., Carbon Nanotube Amplification Strategies for Highly Sensitive Immunodetection of Cancer Biomarkers. *J. Am. Chem. Soc.* **2006,** *128*, 11199-205.

52. Bianco, A., et al., Applications of Carbon Nanotubes in Drug Delivery. *Curr. Opin. Chem. Biol.* **2005,** *9*, 674-79.

53. Kostarelos, K., Rational Design and Engineering of Delivery Systems for Therapeutics: Biomedical Exercises in Colloid and Surface Science. *Adv. Colloid Interface Sci.* **2003,** *106*, 147-68.

54. Wu, W., et al., Targeted Delivery of Amphotericin B to Cells by Using Functionalized Carbon Nanotubes13. *Angew. Chem., Int. Ed.* **2005,** *44*, 6358-62.

55. Allen, M. J., et al., Honeycomb Carbon: A Review of Graphene. *Chem. Rev.* **2010,** *110*, 132-45.

56. Landau, L., Theory of Phase Changes. *Physikalische Zeitschrift der Sowjetunion* **1937,** *11*, 26-47.

57. Kim, K. S., et al., Large-Scale Pattern Growth of Graphene Films for Stretchable Transparent Electrodes. *Nature* **2009,** *457*, 706-10.

58. Sutter, P. W., et al., Epitaxial Graphene on Ruthenium. *Nat. Mater.* **2008,** *7*, 406-11.

59. Reina, A., et al., Large Area, Few-Layer Graphene Films on Arbitrary Substrates by Chemical Vapor Deposition. *Nano Lett.* **2009,** *9*, 30-35.

60. Berger, C., et al., Ultrathin Epitaxial Graphite: Two-Dimensional Electron Gas Properties and a Route toward Graphene-Based Nanoelectronics. *J. Phys. Chem. B* **2004,** *108*, 19912-16.

61. Berger, C., et al., Electronic Confinement and Coherence in Patterned Epitaxial Graphene. *Science* **2006,** *312*, 1191-96.

62. Stankovich, S., et al., Synthesis of Graphene-Based Nanosheets Via Chemical Reduction of Exfoliated Graphite Oxide. *Carbon* **2007,** *45*, 1558-65.

63. Tung, V. C., et al., High-Throughput Solution Processing of Large-Scale Graphene. *Nat. Nanotechnol.* **2009,** *4*, 25-29.

64. Lomeda, J. R., et al., Diazonium Functionalization of Surfactant-Wrapped Chemically Converted Graphene Sheets. *J. Am. Chem. Soc.* **2008,** *130*, 16201-06.

65. Schniepp, H. C., et al., Functionalized Single Graphene Sheets Derived from Splitting Graphite Oxide. *J. Phys. Chem. B* **2006,** *110*, 8535-39.

66. Mcallister, M. J., et al., Single Sheet Functionalized Graphene by Oxidation and Thermal Expansion of Graphite. *Chem. Mater.* **2007,** *19*, 4396-404.

67. Haddon, R. C., Graphene: Noble No More. *Acc. Chem. Res.* **2013,** *46*, 1-3.

68. Novoselov, K. S., et al., Unconventional Quantum Hall Effect and Berry's Phase of 2[Pi] in Bilayer Graphene. *Nat. Phys.* **2006,** *2*, 177-80.

69. Jiang, Z., et al., Quantum Hall Effect in Graphene. *Solid State Commun.* **2007,** *143*, 14-19.

70. Jiang, Z., et al., Quantum Hall States near the Charge-Neutral Dirac Point in Graphene. *Phys. Rev. Lett.* **2007,** *99*, 106802.

71. Zhang, Y., et al., Experimental Observation of the Quantum Hall Effect and Berry's Phase in Graphene. *Nature* **2005,** *438*, 201-04.

72. Novoselov, K. S., et al., Room-Temperature Quantum Hall Effect in Graphene. *Science* **2007,** *315*, 1379.

73. Bolotin, K. I., et al., Ultrahigh Electron Mobility in Suspended Graphene. *Solid State Commun.* **2008,** *146*, 351-55.

245. Casabianca, L. B., et al., Nmr-Based Structural Modeling of Graphite Oxide Using Multidimensional 13c Solid-State Nmr and Ab Initio Chemical Shift Calculations. *J. Am. Chem. Soc.* **2010,** *132*, 5672-76.

246. Trott, O.; Olson, A. J., Software News and Update Autodock Vina: Improving the Speed and Accuracy of Docking with a New Scoring Function, Efficient Optimization, and Multithreading. *J. Comput. Chem.* **2010,** *31*, 455-61.

247. Vedala, H., et al., Chemical Sensitivity of Graphene Edges Decorated with Metal Nanoparticles. *Nano Lett.* **2011,** *11*, 2342-47.

248. Nunes, A., et al., *In Vivo* Degradation of Functionalized Carbon Nanotubes after Stereotactic Administration in the Brain Cortex. *Nanomedicine* **2012,** *7*, 1485-94.

249. Michalet, X., et al., Quantum Dots for Live Cells, in Vivo Imaging, and Diagnostics. *Science* **2005,** *307*, 538-44.

250. De, M., et al., Applications of Nanoparticles in Biology. *Adv. Mater.* **2008,** *20*, 4225-41.

251. Vashist, S. K., et al., Delivery of Drugs and Biomolecules Using Carbon Nanotubes. *Carbon* **2011,** *49,* 4077-97.

252. Kamalha, E., et al., Nanotechnology and Carbon Nanotubes; a Review of Potential in Drug Delivery. *Macromol. Res.* **2012,** *20,* 891-98.

253. Qureshi, S. R., et al., Nanotechnology Based Drug Delivery System. *J. Pharm. Res. Opin.* **2011,** *1,* 161-65.

254. Chun, H., et al., Engineering Low-Aspect Ratio Carbon Nanostructures: Nanocups, Nanorings, and Nanocontainers. *ACS Nano* **2009,** *3,* 1274-78.

255. Oyama, T. G., et al., Fabrication of Nanobeads from Nanocups by Controlling Scission/Crosslinking in Organic Polymer Materials. *Nanotechnology* **2012,** *23,* 495307.

256. Zhao, Y., et al., Corking Carbon Nanotube Cups with Gold Nanoparticles. *ACS Nano* **2012,** *6,* 6912-21.

257. Novoselov, K. S., et al., Electric Field Effect in Atomically Thin Carbon Films. *Science (Washington, DC, U. S.)* **2004,** *306,* 666-69.

258. Castro, N. a. H., et al., The Electronic Properties of Graphene. *Rev. Mod. Phys.* **2009,** *81,* 109-62.

259. Wang, X.; Dai, H., Etching and Narrowing of Graphene from the Edges. *Nat. Chem.* **2010,** *2,* 661-65.

260. Kamat, P. V., Graphene-Based Nanoassemblies for Energy Conversion. *J. Phys. Chem. Lett.* **2011,** *2,* 242-51.

261. Schedin, F., et al., Detection of Individual Gas Molecules Adsorbed on Graphene. *Nat Mater* **2007,** *6,* 652-5.

262. Robinson, J. T., et al., Reduced Graphene Oxide Molecular Sensors. *Nano Lett.* **2008,** *8,* 3137-40.

263. Yang, L., et al., Quasiparticle Energies and Band Gaps in Graphene Nanoribbons. *Phys. Rev. Lett.* **2007,** *99*, 186801.

264. Han, M. Y., et al., Energy Band-Gap Engineering of Graphene Nanoribbons. *Phys. Rev. Lett.* **2007,** *98*, 206805.

265. Yang, X., et al., Two-Dimensional Graphene Nanoribbons. *J. Am. Chem. Soc.* **2008,** *130*, 4216-17.

74. Buchsteiner, A., et al., Water Dynamics in Graphite Oxide Investigated with Neutron Scattering. *J. Phys. Chem. B* **2006,** *110*, 22328-38.

75. He, H., et al., Solid-State Nmr Studies of the Structure of Graphite Oxide. *J. Phys. Chem.* **1996,** *100*, 19954-58.

76. He, H., et al., A New Structural Model for Graphite Oxide. *Chem. Phys. Lett.* **1998,** *287*, 53-56.

77. Lerf, A., et al., Structure of Graphite Oxide Revisited. *J. Phys. Chem. B* **1998,** *102*, 4477-82.

78. Cai, W., et al., Synthesis and Solid-State Nmr Structural Characterization of 13c-Labeled Graphite Oxide. *Science* **2008,** *321*, 1815-17.

79. Park, S.; Ruoff, R. S., Chemical Methods for the Production of Graphenes. *Nat. Nanotechnol.* **2009,** *4*, 217-24.

80. Li, D., et al., Processable Aqueous Dispersions of Graphene Nanosheets. *Nat. Nanotechnol.* **2008,** *3*, 101-05.

81. Bagri, A., et al., Structural Evolution During the Reduction of Chemically Derived Graphene Oxide. *Nat Chem* **2010,** *2*, 581-87.

82. Stankovich, S., et al., Graphene-Based Composite Materials. *Nature* **2006,** *442*, 282-86.

83. Wang, G., et al., Facile Synthesis and Characterization of Graphene Nanosheets. *J. Phys. Chem. C* **2008,** *112,* 8192-95.

84. Williams, G., et al., Tio2-Graphene Nanocomposites. Uv-Assisted Photocatalytic Reduction of Graphene Oxide. *ACS Nano* **2008,** *2,* 1487-91.

85. Weisman, R. B., et al., (N,M)-Assigned Absorption and Emission Spectra of Single-Walled Carbon Nanotubes. *AIP Conf. Proc.* **2003,** *685,* 241-45.

86. Niyogi, S., et al., Chemistry of Single-Walled Carbon Nanotubes. *Acc. Chem. Res.* **2002,** *35,* 1105-13.

87. O'connell, M. J., et al., Band Gap Fluorescence from Individual Single-Walled Carbon Nanotubes. *Science* **2002,** *297,* 593-96.

88. Liu, Z., et al., Carbon Nanotubes in Biology and Medicine: In Vitro and in Vivo Detection, Imaging and Drug Delivery. *Nano Research* **2009,** *2,* 85-120.

89. Dresselhaus, M. S., et al., Perspectives on Carbon Nanotubes and Graphene Raman Spectroscopy. *Nano Lett.* **2010,** *10,* 751-58.

90. Dong, L.-X.; Chen, Q., Properties, Synthesis, and Characterization of Graphene. *Frontiers of Materials Science in China* **2010,** *4,* 45-51.

91. Cao, G., *Nanostructures and Nanomaterials - Synthesis, Properties and Applications*. Imperial College Press: London, 2004; p 433.

92. Bellucci, S., et al., Atomic Force Microscopy Characterization of Carbon Nanotubes. *Journal of Physics: Conference Series* **2007,** *61,* 99.

93. Liu, J., et al., Fullerene Pipes. *Science* **1998,** *280,* 1253-56.

94. Chen, R. J., et al., Noncovalent Functionalization of Carbon Nanotubes for Highly Specific Electronic Biosensors. *Proceedings of the National Academy of Sciences* **2003,** *100,* 4984-89.

95. Kapralov, A. A., et al., Adsorption of Surfactant Lipids by Single-Walled Carbon Nanotubes in Mouse Lung Upon Pharyngeal Aspiration. *ACS Nano* **2012,** *6*, 4147-56.

96. Nemes-Incze, P., et al., Anomalies in Thickness Measurements of Graphene and Few Layer Graphite Crystals by Tapping Mode Atomic Force Microscopy. *Carbon* **2008,** *46*, 1435-42.

97. Zhu, Y., et al., Exfoliation of Graphite Oxide in Propylene Carbonate and Thermal Reduction of the Resulting Graphene Oxide Platelets. *ACS Nano* **2010,** *4*, 1227-33.

98. Wang, K., et al., Biocompatibility of Graphene Oxide. *Nanoscale Research Letters* **2010,** *6*, 1-8.

99. Yang, K., et al., The Effect of Chemical Treatment on the Crystallinity of Multi-Walled Carbon Nanotubes. *J. Phys. Chem. Solids* **2008,** *69*, 222-29.

100. Urban, K. W., Electron Microscopy: The Challenges of Graphene. *Nat Mater* **2011,** *10*, 165-66.

101. Muller, J., et al., Respiratory Toxicity of Multi-Wall Carbon Nanotubes. *Toxicol. Appl. Pharmacol.* **2005,** *207*, 221-31.

102. Lam, C.-W., et al., Pulmonary Toxicity of Single-Wall Carbon Nanotubes in Mice 7 and 90 Days after Intratracheal Instillation. *Toxicol. Sci.* **2004,** *77*, 126-34.

103. Warheit, D. B., et al., Comparative Pulmonary Toxicity Assessment of Single-Wall Carbon Nanotubes in Rats. *Toxicol. Sci.* **2004,** *77*, 117-25.

104. Shvedova, A. A., et al., Unusual Inflammatory and Fibrogenic Pulmonary Responses to Single-Walled Carbon Nanotubes in Mice. *Am. J. Physiol.* **2005,** *289*, L698-L708.

105. Muller, J., et al., Clastogenic and Aneugenic Effects of Multi-Wall Carbon Nanotubes in Epithelial Cells. *Carcinogenesis* **2008,** *29*, 427-33.

106. Bottini, M., et al., Multi-Walled Carbon Nanotubes Induce T Lymphocyte Apoptosis. *Toxicol. Lett.* **2006,** *160,* 121-26.

107. Cui, D., et al., Effect of Single Wall Carbon Nanotubes on Human Hek293 Cells. *Toxicol. Lett.* **2005,** *155,* 73-85.

108. Monteiro-Riviere, N. A., et al., Multi-Walled Carbon Nanotube Interactions with Human Epidermal Keratinocytes. *Toxicol. Lett.* **2005,** *155,* 377-84.

109. Shvedova, A., et al., Exposure to Carbon Nanotube Material: Assessment of Nanotube Cytotoxicity Using Human Keratinocyte Cells. *J. Toxicol. Environ. Health, Part A* **2003,** *66,* 1909-26.

110. Huczko, A., et al., Physiological Testing of Carbon Nanotubes: Are They Asbestos-Like? *Fullerene Science and Technology* **2001,** *9,* 251-54.

111. Huczko, A.; Lange, H., Carbon Nanotubes: Experimental Evidence for a Null Risk of Skin Irritation and Allergy. *Fullerene Science and Technology* **2001,** *9,* 247-50.

112. Mitchell, L. A., et al., Pulmonary and Systemic Immune Response to Inhaled Multiwalled Carbon Nanotubes. *Toxicol. Sci.* **2007,** *100,* 203-14.

113. Davoren, M., et al., In Vitro Toxicity Evaluation of Single Walled Carbon Nanotubes on Human A549 Lung Cells. *Toxicol. in Vitro* **2007,** *21,* 438-48.

114. Pulskamp, K., et al., Carbon Nanotubes Show No Sign of Acute Toxicity but Induce Intracellular Reactive Oxygen Species in Dependence on Contaminants. *Toxicol. Lett.* **2007,** *168,* 58-74.

115. Worle-Knirsch, J. M., et al., Oops They Did It Again! Carbon Nanotubes Hoax Scientists in Viability Assays. *Nano Lett.* **2006,** *6,* 1261-8.

116. Muller, J., et al., Structural Defects Play a Major Role in the Acute Lung Toxicity of Multiwall Carbon Nanotubes: Toxicological Aspects. *Chem. Res. Toxicol.* **2008,** *21,* 1698-705.

117. Dujardin, E., et al., Purification of Single-Shell Nanotubes. *Adv. Mater.* **1998,** *10,* 611-13.

118. Kim, Y. A., et al., Annealing Effect on Disordered Multiwall Carbon Nanotubes. *Chem. Phys. Lett.* **2003,** *380,* 319-24.

119. Kagan, V. E., et al., Direct and Indirect Effects of Single Walled Carbon Nanotubes on Raw 264.7 Macrophages: Role of Iron. *Toxicol. Lett.* **2006,** *165,* 88-100.

120. Sato, Y., et al., Influence of Length on Cytotoxicity of Multi-Walled Carbon Nanotubes against Human Acute Monocytic Leukemia Cell Line Thp-1 in Vitro and Subcutaneous Tissue of Rats in Vivo. *Mol. BioSyst.* **2005,** *1,* 176-82.

121. Poland, C. A., et al., Carbon Nanotubes Introduced into the Abdominal Cavity of Mice Show Asbestos-Like Pathogenicity in a Pilot Study. *Nat. Nanotechnol.* **2008,** *3,* 423-28.

122. Magrez, A., et al., Cellular Toxicity of Carbon-Based Nanomaterials. *Nano Lett.* **2006,** *6,* 1121-25.

123. Fenoglio, I., et al., Structural Defects Play a Major Role in the Acute Lung Toxicity of Multiwall Carbon Nanotubes: Physicochemical Aspects. *Chem. Res. Toxicol.* **2008,** *21,* 1690-97.

124. Bussy, C., et al., Safety Considerations for Graphene: Lessons Learnt from Carbon Nanotubes. *Acc. Chem. Res.* **2012,** *46,* 692-701.

125. Liao, K.-H., et al., Cytotoxicity of Graphene Oxide and Graphene in Human Erythrocytes and Skin Fibroblasts. *ACS Applied Materials & Interfaces* **2011,** *3,* 2607-15.

126. Singh, S. K., et al., Amine-Modified Graphene: Thrombo-Protective Safer Alternative to Graphene Oxide for Biomedical Applications. *ACS Nano* **2012,** *6,* 2731-40.

127. Schinwald, A., et al., Graphene-Based Nanoplatelets: A New Risk to the Respiratory System as a Consequence of Their Unusual Aerodynamic Properties. *ACS Nano* **2011,** *6,* 736-46.

128. Ali-Boucetta, H., et al., Purified Graphene Oxide Dispersions Lack in Vitro Cytotoxicity and in Vivo Pathogenicity. *Adv Healthc Mater* **2013,** *2,* 433-41.

129. Allen, B. L., et al., Biodegradation of Single-Walled Carbon Nanotubes through Enzymatic Catalysis. *Nano Lett.* **2008,** *8,* 3899-903.

130. Allen, B. L., et al., Mechanistic Investigations of Horseradish Peroxidase-Catalyzed Degradation of Single-Walled Carbon Nanotubes. *J Am Chem Soc* **2009,** *131,* 17194-205.

131. Russier, J., et al., Oxidative Biodegradation of Single- and Multi-Walled Carbon Nanotubes. *Nanoscale* **2011,** *3,* 893-96.

132. Zhao, Y., et al., Enzymatic Degradation of Multiwalled Carbon Nanotubes. *J. Phys. Chem. A* **2011,** *115,* 9536-44.

133. Kotchey, G. P., et al., The Enzymatic Oxidation of Graphene Oxide. *ACS Nano* **2011,** *5,* 2098-108.

134. Kagan, V. E., et al., Carbon Nanotubes Degraded by Neutrophil Myeloperoxidase Induce Less Pulmonary Inflammation. *Nat. Nanotechnol.* **2010,** *5,* 354-59.

135. Vlasova, I., et al., Myeloperoxidase-Induced Biodegradation of Single-Walled Carbon Nanotubes Is Mediated by Hypochlorite. *Russ. J. Bioorg. Chem.* **2011,** *37,* 453-63.

136. Shvedova, A. A., et al., Impaired Clearance and Enhanced Pulmonary Inflammatory/Fibrotic Response to Carbon Nanotubes in Myeloperoxidase-Deficient Mice. *PLoS One* **2012,** *7,* e30923.

137. Andon, F. T., et al., Biodegradation of Single-Walled Carbon Nanotubes by Eosinophil Peroxidase. *Small* **2013,** *9,* 2721–29.

138. O'brien, P. J., Peroxidases. *Chem.-Biol. Interact.* **2000,** *129,* 113-39.

139. Veitch, N. C., Horseradish Peroxidase: A Modern View of a Classic Enzyme. *Phytochemistry* **2004,** *65,* 249-59.

140. Azevedo, A. M., et al., Horseradish Peroxidase: A Valuable Tool in Biotechnology. In *Biotechnol. Annu. Rev.*, Elsevier: 2003; Vol. Volume 9, pp 199-247.

141. Duran, N.; Esposito, E., Potential Applications of Oxidative Enzymes and Phenol Oxidase-Like Compounds in Wastewater and Soil Treatment: A Review. *Applied Catalysis, B Environmental* **2000,** *28*, 83-99.

142. Rodríguez-López, J. N., et al., Mechanism of Reaction of Hydrogen Peroxide with Horseradish Peroxidase: Identification of Intermediates in the Catalytic Cycle. *J. Am. Chem. Soc.* **2001,** *123*, 11838-47.

143. Filizola, M.; Loew, G. H., Role of Protein Environment in Horseradish Peroxidase Compound I Formation: Molecular Dynamics Simulations of Horseradish Peroxidase-Hooh Complex. *J. Am. Chem. Soc.* **2000,** *122*, 18-25.

144. Chiu, C.-F., et al., Enzyme-Catalyzed Oxidation Facilitates the Return of Fluorescence for Single-Walled Carbon Nanotubes. *J. Am. Chem. Soc.* **2013**, DOI: 10.1021/ja400699y.

145. Bachilo, S. M., et al., Structure-Assigned Optical Spectra of Single-Walled Carbon Nanotubes. *Science* **2002,** *298*, 2361-6.

146. Davies, M. J., Myeloperoxidase-Derived Oxidation: Mechanisms of Biological Damage and Its Prevention. *J Clin Biochem Nutr* **2010,** *48*, 8-19.

147. Nauseef, W. M., How Human Neutrophils Kill and Degrade Microbes: An Integrated View. *Immunol. Rev.* **2007,** *219*, 88-102.

148. Hansson, M., et al., Biosynthesis, Processing, and Sorting of Human Myeloperoxidase. *Arch. Biochem. Biophys.* **2006,** *445*, 214-24.

149. Arnhold, J., Properties, Functions, and Secretion of Human Myeloperoxidase. *Biochemistry (Mosc)* **2004,** *69*, 4-9.

150. Lardinois, O. M.; Ortiz De Montellano, P. R., Epr Spin-Trapping of a Myeloperoxidase Protein Radical. *Biochem. Biophys. Res. Commun.* **2000,** *270*, 199-202.

151. Davies, M. J., et al., Mammalian Heme Peroxidases: From Molecular Mechanisms to Health Implications. *Antioxid. Redox Signaling* **2008,** *10,* 1199-234.

152. Kotchey, G. P., et al., Effect of Antioxidants on Enzyme-Catalysed Biodegradation of Carbon Nanotubes. *J. Mater. Chem. B* **2013,** *1,* 302-09.

153. Odom, T. W., et al., Structure and Electronic Properties of Carbon Nanotubes. *J. Phys. Chem. B* **2000,** *104,* 2794-809.

154. Dresselhaus, M. S., et al., Unusual Properties and Structure of Carbon Nanotubes. *Annu. Rev. Mater. Res.* **2004,** *34,* 247-78.

155. Ruoff, R. S.; Lorents, D. C., Mechanical and Thermal Properties of Carbon Nanotubes. *Carbon* **1995,** *33,* 925-30.

156. Avouris, P., et al., Carbon Nanotube Electronics. *Proc. IEEE* **2003,** *91,* 1772-84.

157. Feigel, I. M., et al., Biosensors Based on One-Dimensional Nanostructures. *J. Mater. Chem.* **2011,** *21,* 8940-54.

158. Coleman, J. N., et al., Small but Strong: A Review of the Mechanical Properties of Carbon Nanotube-Polymer Composites. *Carbon* **2006,** *44,* 1624-52.

159. Baughman, R. H., et al., Carbon Nanotubes--the Route toward Applications. *Science* **2002,** *297,* 787-92.

160. Tkach, A. V., et al., Direct Effects of Carbon Nanotubes on Dendritic Cells Induce Immune Suppression Upon Pulmonary Exposure. *ACS Nano* **2011,** *5,* 5755-62.

161. Kisin, E. R., et al., Single-Walled Carbon Nanotubes: Geno- and Cytotoxic Effects in Lung Fibroblast V79 Cells. *J. Toxicol. Environ. Health, Part A* **2007,** *70,* 2071-79.

162. Shvedova, A. A., et al., Sequential Exposure to Carbon Nanotubes and Bacteria Enhances Pulmonary Inflammation and Infectivity. *Am. J. Respir. Cell Mol. Biol.* **2008,** *38,* 579-90.

163. Shvedova, A. A., et al., Mechanisms of Carbon Nanotube-Induced Toxicity: Focus on Oxidative Stress. *Toxicol. Appl. Pharmacol.* **2012,** *261*, 121-33.

164. Pérez, S., et al., Analysis, Behavior and Ecotoxicity of Carbon-Based Nanomaterials in the Aquatic Environment. *Trends Anal. Chem.* **2009,** *28*, 820-32.

165. Petersen, E. J., et al., Potential Release Pathways, Environmental Fate, and Ecological Risks of Carbon Nanotubes. *Environ. Sci. Technol.* **2011,** *45*, 9837-56.

166. Lowry, G. V., et al., Transformations of Nanomaterials in the Environment. *Environ. Sci. Technol.* **2012,** *46*, 6893-99.

167. Krug, H. F.; Wick, P., Nanotoxicology: An Interdisciplinary Challenge. *Angew. Chem., Int. Ed.* **2011,** *50*, 1260-78.

168. Bianco, A., et al., Making Carbon Nanotubes Biocompatible and Biodegradable. *Chem. Commun.* **2011,** *47*, 10182-88.

169. Di Mascio, P., et al., Antioxidant Defense Systems: The Role of Carotenoids, Tocopherols, and Thiols. *Am. J. Clin. Nutr.* **1991,** *53*, 194S-200S.

170. Padayatty, S. J., et al., Vitamin C as an Antioxidant: Evaluation of Its Role in Disease Prevention. *J. Am. Coll. Nutr.* **2003,** *22*, 18-35.

171. Traber, M. G.; Stevens, J. F., Vitamins C and E: Beneficial Effects from a Mechanistic Perspective. *Free Radic. Biol. Med.* **2011,** *51*, 1000-13.

172. Perricone, C., et al., Glutathione: A Key Player in Autoimmunity. *Autoimmun. Rev.* **2009,** *8*, 697-701.

173. Pattison, D. I.; Davies, M. J., Reactions of Myeloperoxidase-Derived Oxidants with Biological Substrates:Gaining Chemical Insight into Human Inflammatory Diseases. *Curr. Med. Chem.* **2006,** *13*, 3271-90.

174. Winterbourn, C. C., et al., Modeling the Reactions of Superoxide and Myeloperoxidase in the Neutrophil Phagosome: Implications for Microbial Killing. *J. Biol. Chem.* **2006,** *281*, 39860-9.

175. Lide, D. R., *Potentials*. CRC Press: Boca Raton, 2004; p 20-29.

176. Yang, J.-C., et al., Assessment of Adequate Sodium Hypochlorite Concentration for Pre-Oxidization of Multi-Walled Carbon Nanotubes. *J. Chem. Technol. Biotechnol.* **2010,** *85*, 699-707.

177. Value reported for P3 SWCNTs by Carbon Solutions, Inc.

178. Chen, J., et al., Dissolution of Full-Length Single-Walled Carbon Nanotubes. *J. Phys. Chem. B* **2001,** *105*, 2525-28.

179. Kuzmany, H., et al., Functionalization of Carbon Nanotubes. *Synth. Met.* **2004,** *141*, 113-22.

180. Kukovecz, A., et al., On the Stacking Behavior of Functionalized Single-Wall Carbon Nanotubes. *J. Phys. Chem. B* **2002,** *106*, 6374-80.

181. Martínez, M. T., et al., Sensitivity of Single Wall Carbon Nanotubes to Oxidative Processing: Structural Modification, Intercalation and Functionalisation. *Carbon* **2003,** *41*, 2247-56.

182. Sarkar, S., et al., Optical Properties of Breast Tumor Phantoms Containing Carbon Nanotubes and Nanohorns. *J. Biomed. Opt.* **2011,** *16*, 051304-11.

183. Gao, W.; Song, J., Towards Surface Acid–Base Property of the Carboxylic Multi-Walled Carbon Nanotubes by Zero Current Potentiometry. *Electrochem. Commun.* **2009,** *11*, 1285-88.

184. Zhao, B., et al., Synthesis and Characterization of Water Soluble Single-Walled Carbon Nanotube Graft Copolymers. *J. Am. Chem. Soc.* **2005,** *127*, 8197-203.

185. Klebanoff, S. J., Myeloperoxidase: Friend and Foe. *J. Leukocyte Biol.* **2005,** *77*, 598-625.

186. Zhang, J., et al., Effect of Chemical Oxidation on the Structure of Single-Walled Carbon Nanotubes. *J. Phys. Chem. B* **2003,** *107*, 3712-18.

187. Zhang, J., et al., Reduction of Graphene Oxide Via L-Ascorbic Acid. *Chem. Commun.* **2010,** *46*, 1112-14.

188. Pham, T. A., et al., One-Step Reduction of Graphene Oxide with L-Glutathione. *Colloids Surf., A* **2011,** *384*, 543-48.

189. Dyke, C. A.; Tour, J. M., Solvent-Free Functionalization of Carbon Nanotubes. *J. Am. Chem. Soc.* **2003,** *125*, 1156-57.

190. Kagan, V. E., et al., Direct Evidence for Recycling of Myeloperoxidase-Catalyzed Phenoxyl Radicals of a Vitamin E Homologue, 2,2,5,7,8-Pentamethyl-6-Hydroxy Chromane, by Ascorbate/Dihydrolipoate in Living Hl-60 Cells. *Biochim. Biophys. Acta* **2003,** *1620*, 72-84.

191. Borsook, H.; Keighley, G., Oxidation-Reduction Potential of Ascorbic Acid (Vitamin C). *Proc. Natl. Acad. Sci. U. S. A.* **1933,** *19*, 875–78.

192. Borisenko, G. G., et al., Nitroxides Scavenge Myeloperoxidase-Catalyzed Thiyl Radicals in Model Systems and in Cells. *J. Am. Chem. Soc.* **2004,** *126*, 9221-32.

193. Buettner, G. R., The Pecking Order of Free Radicals and Antioxidants: Lipid Peroxidation, A-Tocopherol, and Ascorbate. *Arch. Biochem. Biophys.* **1993,** *300*, 535-43.

194. Finley, J. W., et al., Oxidation of Glutathione by Hydrogen Peroxide and Other Oxidizing Agents. *J. Agric. Food Chem.* **1981,** *29*, 404-07.

195. Folkes, L. K., et al., Kinetics and Mechanisms of Hypochlorous Acid Reactions. *Arch. Biochem. Biophys.* **1995,** *323*, 120-26.

196. Winterbourn, C. C.; Brennan, S. O., Characterization of the Oxidation Products of the Reaction between Reduced Glutathione and Hypochlorous Acid. *Biochem. J.* **1997,** *326*, 87-92.

197. Shvedova, A. A., et al., Vitamin E Deficiency Enhances Pulmonary Inflammatory Response and Oxidative Stress Induced by Single-Walled Carbon Nanotubes in C57bl/6 Mice. *Toxicol. Appl. Pharmacol.* **2007,** *221*, 339-48.

198. Kim, K. K., et al., Doping Strategy of Carbon Nanotubes with Redox Chemistry. *New J. Chem.* **2010,** *34*, 2183-88.

199. Tanaka, Y., et al., In Situ Photoluminescence Spectroelectrochemistry of Single-Walled Carbon Nanotubes with Nine Different Chiral Indices. *Chem. Lett.* **2009,** *38*, 864-65.

200. O'connell, M. J., et al., Chiral Selectivity in the Charge-Transfer Bleaching of Single-Walled Carbon-Nanotube Spectra. *Nat Mater* **2005,** *4*, 412-18.

201. Barros, E. B., et al., Charge Transfer Effects in Acid Treated Single-Wall Carbon Nanotubes. *Carbon* **2005,** *43*, 2495-500.

202. Gao, J., et al., A Novel Pathway Regulates Memory and Plasticity Via Sirt1 and Mir-134. *Nature* **2010,** *466*, 1105-U120.

203. Sun, Z., et al., Quantitative Evaluation of Surfactant-Stabilized Single-Walled Carbon Nanotubes: Dispersion Quality and Its Correlation with Zeta Potential. *J. Phys. Chem. C* **2008,** *112*, 10692-99.

204. Hu, H., et al., Influence of the Zeta Potential on the Dispersability and Purification of Single-Walled Carbon Nanotubes. *J. Phys. Chem. B* **2005,** *109*, 11520-24.

205. Liu, X., et al., Biodurability of Single-Walled Carbon Nanotubes Depends on Surface Functionalization. *Carbon* **2010,** *48*, 1961-69.

206. Geim, A. K.; Novoselov, K. S., The Rise of Graphene. *Nat. Mater.* **2007,** *6*, 183-91.

207. Zhu, Y., et al., Graphene and Graphene Oxide: Synthesis, Properties, and Applications. *Adv. Mater.* **2010,** *22*, 3906-24.

208. Lee, C., et al., Measurement of the Elastic Properties and Intrinsic Strength of Monolayer Graphene. *Science* **2008,** *321,* 385-88.

209. Geim, A. K., Graphene: Status and Prospects. *Science* **2009,** *324,* 1530-34.

210. Kauffman, D. R.; Star, A., Graphene Versus Carbon Nanotubes for Chemical Sensor and Fuel Cell Applications. *Analyst* **2010,** *135,* 2790-97.

211. Dreyer, D. R., et al., The Chemistry of Graphene Oxide. *Chem. Soc. Rev.* **2010,** *39,* 228-40.

212. Dreyer, D. R., et al., From Conception to Realization: An Historial Account of Graphene and Some Perspectives for Its Future. *Angew. Chem., Int. Ed.* **2010,** *49,* 9336-44.

213. Sun, X., et al., Nano-Graphene Oxide for Cellular Imaging and Drug Delivery. *Nano Research* **2008,** *1,* 203-12.

214. Dikin, D. A., et al., Preparation and Characterization of Graphene Oxide Paper. *Nature* **2007,** *448,* 457-60.

215. Li, S.-S., et al., Solution-Processable Graphene Oxide as an Efficient Hole Transport Layer in Polymer Solar Cells. *ACS Nano* **2010,** *4,* 3169-74.

216. Liu, L., et al., Graphene Oxidation: Thickness-Dependent Etching and Strong Chemical Doping. *Nano Lett.* **2008,** *8,* 1965-70.

217. Tapaszto, L., et al., Tailoring the Atomic Structure of Graphene Nanoribbons by Scanning Tunnelling Microscope Lithography. *Nat. Nanotechnol.* **2008,** *3,* 397-401.

218. Li, X., et al., Chemically Derived, Ultrasmooth Graphene Nanoribbon Semiconductors. *Science* **2008,** *319,* 1229-32.

219. Gorris, H. H.; Walt, D. R., Mechanistic Aspects of Horseradish Peroxidase Elucidated through Single-Molecule Studies. *J. Am. Chem. Soc.* **2009,** *131,* 6277-82.

220. Welinder, K. G., Amino Acid Sequence Studies of Horseradish Peroxidase. *Eur. J. Biochem.* **1979,** *96*, 483-502.

221. Qian, S. Y., et al., Identification of Protein-Derived Tyrosyl Radical in the Reaction of Cytochrome C and Hydrogen Peroxide: Characterization by Esr Spin-Trapping, Hplc and Ms. *Biochem. J.* **2002,** *363*, 281-88.

222. Detweiler, C. D., et al., Identification of the Myoglobin Tyrosyl Radical by Immuno-Spin Trapping and Its Dimerization. *Free Radic. Biol. Med.* **2005,** *38*, 969-76.

223. Ehrenshaft, M.; Mason, R. P., Protein Radical Formation on Thyroid Peroxidase During Turnover as Detected by Immuno-Spin Trapping. *Free Radic. Biol. Med.* **2006,** *41*, 422-30.

224. Trott, O.; Olson, A. J., Autodock Vina: Improving the Speed and Accuracy of Docking with a New Scoring Function, Efficient Optimization and Multithreading. *J. Comput. Chem.* **2010,** *31*, 455-61.

225. Tuynman, A., et al., Enantioselective Epoxidation and Carbon-Carbon Bond Cleavage Catalyzed by Coprinus Cinereus Peroxidase and Myeloperoxidase. *J. Biol. Chem.* **2000,** *275*, 3025-30.

226. Ortiz De Montellano, P. R.; Grab, L. A., Cooxidation of Styrene by Horseradish Peroxidase and Phenols: A Biochemical Model for Protein-Mediated Cooxidation. *Biochemistry* **1987,** *26*, 5310-14.

227. Novoselov, K. S., et al., Two-Dimensional Gas of Massless Dirac Fermions in Graphene. *Nature* **2005,** *438*, 197-200.

228. Meric, I., et al., Current Saturation in Zero-Bandgap, Top-Gated Graphene Field-Effect Transistors. *Nat. Nanotechnol.* **2008,** *3*, 654-59.

229. Nakada, K., et al., Edge State in Graphene Ribbons: Nanometer Size Effect and Edge Shape Dependence. *Phys. Rev. B: Condens. Matter Mater. Phys.* **1996,** *54*, 17954.

230. Son, Y.-W., et al., Energy Gaps in Graphene Nanoribbons. *Phys. Rev. Lett.* **2006,** *97*, 216803.

231. Barone, V., et al., Electronic Structure and Stability of Semiconducting Graphene Nanoribbons. *Nano Lett.* **2006,** *6*, 2748-54.

232. Bai, J., et al., Graphene Nanomesh. *Nat Nano* **2010,** *5*, 190-94.

233. Kim, M., et al., Fabrication and Characterization of Large-Area, Semiconducting Nanoperforated Graphene Materials. *Nano Lett.* **2010,** *10*, 1125-31.

234. Liu, H., et al., Photochemical Reactivity of Graphene. *J. Am. Chem. Soc.* **2009,** *131*, 17099-101.

235. Huang, J. Y., et al., In Situ Imaging of Layer-by-Layer Sublimation of Suspended Graphene. *Nano Research* **2010,** *3*, 43-50.

236. Bieri, M., et al., Porous Graphenes: Two-Dimensional Polymer Synthesis with Atomic Precision. *Chem. Commun.* **2009**, 6919-21.

237. Chen, F., et al., Electrochemical Gate-Controlled Charge Transport in Graphene in Ionic Liquid and Aqueous Solution. *J. Am. Chem. Soc.* **2009,** *131*, 9908-09.

238. Eda, G., et al., Large-Area Ultrathin Films of Reduced Graphene Oxide as a Transparent and Flexible Electronic Material. *Nat. Nanotechnol.* **2008,** *3*, 270-74.

239. Jung, I., et al., Tunable Electrical Conductivity of Individual Graphene Oxide Sheets Reduced at "Low" Temperatures. *Nano Lett.* **2008,** *8*, 4283-87.

240. Joung, D., et al., High Yield Fabrication of Chemically Reduced Graphene Oxide Field Effect Transistors by Dielectrophoresis. *Nanotechnology* **2010,** *21*.

241. Salas, E. C., et al., Reduction of Graphene Oxide Via Bacterial Respiration. *ACS Nano* **2010,** *4*, 4852-56.

242. Kovtyukhova, N. I., et al., Layer-by-Layer Assembly of Ultrathin Composite Films from Micron-Sized Graphite Oxide Sheets and Polycations. *Chem. Mater.* **1999,** *11*, 771-78.

243. Vijayaraghavan, A., et al., Dielectrophoretic Assembly of High-Density Arrays of Individual Graphene Devices for Rapid Screening. *ACS Nano* **2009,** *3*, 1729-34.

244. Pedretti, A., et al., Vega – an Open Platform to Develop Chemo-Bio-Informatics Applications, Using Plug-in Architecture and Script Programming. *J. Comput.-Aided Mol. Des.* **2004,** *18*, 167-73.